The Innovation

Review

Orderly Porous Covalent Organic Frameworks-based Materials: Superior Adsorbents for Pollutants Removal from Aqueous Solutions

Xiaolu Liu,[1,2] Hongwei Pang,[2] Xuewei Liu,[2] Qian Li,[2] Ning Zhang,[2] Liang Mao,[3] Muqing Qiu,[1] Baowei Hu,[1,*] Hui Yang,[2,*] and Xiangke Wang[2,*]
*Correspondence: hbw@usx.edu.cn (B.H.); h.yang@ncepu.edu.cn (H.Y.); xkwang@ncepu.edu.cn (X.W.)
Received: October 21, 2020; Accepted: January 3, 2021; Published Online: January 4, 2021; https://doi.org/10.1016/j.xinn.2021.100076

GRAPHICAL ABSTRACT

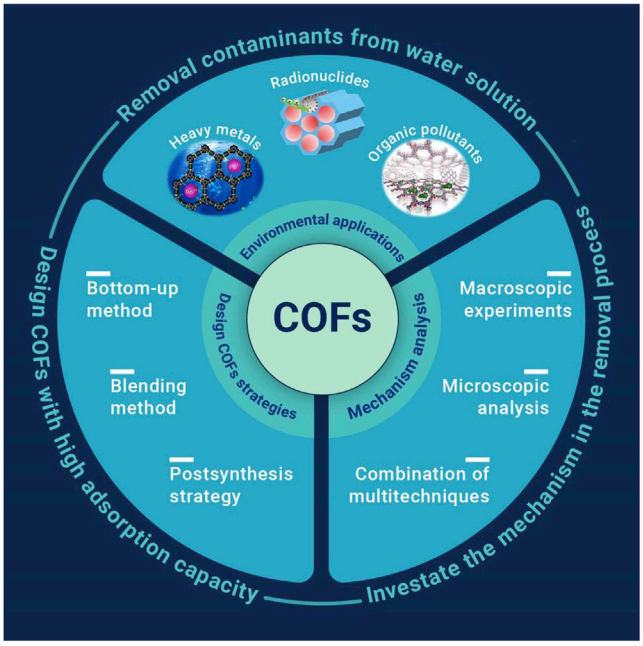

PUBLIC SUMMARY

- Covalent organic frameworks (COFs) are a new type of crystalline porous materials known for chemical stability, high specific surface area, and orderly porous channels.With the rapid growth of industrialization, water pollutants remain a serious issue of public health and environmental protection
- COFs as superior adsorbents for the efficient removal of toxic heavy metal ions, radionuclides, and organic pollutants in water is becoming a hot topic
- Information about the interaction mechanisms between various pollutants and COFs materials are summarized.The perspectives and challenges are proposed to provide some useful inspiration for the application of COFs in environmental pollution management

Review

Orderly Porous Covalent Organic Frameworks-based Materials: Superior Adsorbents for Pollutants Removal from Aqueous Solutions

Xiaolu Liu,[1,2] Hongwei Pang,[2] Xuewei Liu,[2] Qian Li,[2] Ning Zhang,[2] Liang Mao,[3] Muqing Qiu,[1] Baowei Hu,[1,*] Hui Yang,[2,*] and Xiangke Wang[2,*]

[1]School of Life Science, Shaoxing University, Huancheng West Road 508, Shaoxing 312000, P.R. China

[2]College of Environmental Science and Engineering, North China Electric Power University, Beijing 102206, P.R. China

[3]State Key Laboratory of Pollution Control and Resource Reuse, School of the Environment, Nanjing University, Nanjing 210093, P.R. China

*Correspondence: hbw@usx.edu.cn (B.H.); h.yang@ncepu.edu.cn (H.Y.); xkwang@ncepu.edu.cn (X.W.)

Received: October 21, 2020; Accepted: January 3, 2021; Published Online: January 4, 2021; https://doi.org/10.1016/j.xinn.2021.100076

Citation: Liu X., Pang H., Liu X., et al. (2021). Orderly Porous Covalent Organic Frameworks-based Materials: Superior Adsorbents for Pollutants Removal from Aqueous Solutions. The Innovation **2(1)**, 100076.

Covalent organic frameworks (COFs) are a new type of crystalline porous polymers known for chemical stability, excellent structural regularity, robust framework, and inherent porosity, making them promising materials for capturing various types of pollutants from aqueous solutions. This review thoroughly presents the recent progress and advances of COFs and COF-based materials as superior adsorbents for the efficient removal of toxic heavy metal ions, radionuclides, and organic pollutants. Information about the interaction mechanisms between various pollutants and COF-based materials are summarized from the macroscopic and microscopic standpoints, including batch experiments, theoretical calculations, and advanced spectroscopy analysis. The adsorption properties of various COF-based materials are assessed and compared with other widely used adsorbents. Several commonly used strategies to enhance COF-based materials' adsorption performance and the relationship between structural property and sorption ability are also discussed. Finally, a summary and perspective on the opportunities and challenges of COFs and COF-based materials are proposed to provide some inspiring information on designing and fabricating COFs and COF-based materials for environmental pollution management.

KEYWORDS: covalent organic frameworks (COFs); heavy metal ions; radionuclides; organic pollutants; interaction mechanism

INTRODUCTION

Overview of Covalent Organic Framework Materials

The reticular chemistry of linking organic building units by strong covalent bonds to design crystals with extended structures has yielded several new classes of porous materials, and covalent organic frameworks (COFs) have become one of the most widely investigated materials.[1] These porous crystalline materials are entirely composed of light elements (i.e., B, C, N, O, and Si) that are linked by strong covalent bonds, such as B-O, C-N, B-N, B-O-Si, C-C, and C-N.[2] Organic building units used to make up COFs have general features of rigidity in structures and symmetric multiconnectivity, which are prerequisites for forming regular pore frameworks. In particular, the structures and properties of COFs can be predesigned by carefully selecting the building blocks and their conditions for assembly.[2,3] Noteworthy, the reversibility of dynamic covalents, diversity of organic building units, and geometry retention are the key points for the reticular design and synthesis of COFs.[3] Covalently crystalline structure endows COFs with outstanding advantages of low density, large surface area, robust thermal stability, permanent porosity, and facile functional design compared with other porous materials (e.g., molecular sieve,[4,5] metal-organic frameworks (MOFs),[6] zeolite,[7] activated carbons (ACs),[8,9] porous organic polymers,[10] and conjugated microporous polymers.[11] Currently, COFs have attracted multidisciplinary interest because of their excellent properties and widespread applications, such as in adsorption,[12] storage and separation of gases,[13] heterogeneous catalysis,[14,15] energy storage,[16–19] photoelectric sensing,[20,21] and drug delivery.[22–24]

The synthesis of COFs has undergone structural transformation from 2D layers to 3D expanded frameworks, and then to design various functional COF materials (Figure 1A). From the rigid building block dimension standpoint, a combination of rigid building blocks of different geometric shapes determines the COF structures.[3] As shown in Figure 1B, combinations, such as 2D-C_2 + 2D-C_2, 2D-C_2 + 2D-C_3, 2D-C_2 + 2D-C_4, and 2D-C_3 + 2D-C_1 + 2D-C_3 can lead to the construction of 2D COFs with designed topology and pore structure. In contrast, selected combinations of 3D-T_d + 3D-T_d, 3D-T_d + 2D-C_2, or 3D-T_d + 2D-C_3 will afford 3D COFs with different crystalline space groups. Besides the successful topology design strategies (ctn, bor, and dia) of 3D COFs, the new pts, ffc, and more topologies are also applied to build 3D COFs.[33–35,38] In 2D COFs, the extended 2D layers are composed of the periodic organic units via covalent bonds, which stack further to form a layered eclipsed structure via π-π interactions.[36] Generally, monomers with tetrahedral structure (e.g., building blocks containing sp^3 carbon or silane atom) can be used as building units to design the topology structure of 3D COFs. Recently, excellent studies on 3D COFs (SP-3D-COFs and 3D-BMTA-COF) constructed by planar monomers have been reported.[34,35] Beyond doubt, 3D COFs possess higher surface area (in some cases >4,000 $m^2 \cdot g^{-1}$) and larger total pore volume than 2D COFs. From the viewpoint of chemistry, COFs are functionalized via available design strategy to adjust and control their skeleton and physicochemical properties to meet certain application requirements.[36] In a general way, the bottom-up method, post-synthesis strategy, and blending method have been successfully applied for designing various functional COFs, such as COFs on graphene,[39] COFs@Fe_3O_4 with a core-shell structure,[25] COFs on carbon nanotubes (CNTs),[40] metal@COFs,[26] and COFs on CNFs[27] (Figure 1A).

To obtain COFs with higher porosity and structural regularity, rigid p-electron-rich monomers with specific symmetries primarily should be selected as building units to guarantee the complete geometry of the building blocks in COFs.[2,37] The π systems of aromatic families have been proved to be suitable building blocks for COFs not only due to their rigid nature and discrete bonding direction of arenes, but also due to the diverse combinations of aromatic systems, which endow COFs with high flexibility.[3] Reversible covalent bonds formed by dicyclohexylcarbodiimide (DCC) are the key to form COFs. Unlike conventional covalent bonds controlled by kinetic reactions, DCC can drive reversible covalent bond formation, destruction, and modification.[41] Therefore, DCC offers reversible reaction systems with "error-checking" and "proofreading" characteristics, leading to the formation of the most thermodynamically stable structures.[3] The exploration of more diverse frameworks by different connectivity leads to the development of more chemical linkages, such as boron-containing linkage, imine linkage, triazine linkage, hydrazone and azine linkages, β-ketoenamine linkage, and other linkages (Figure S1).[2,42–47]

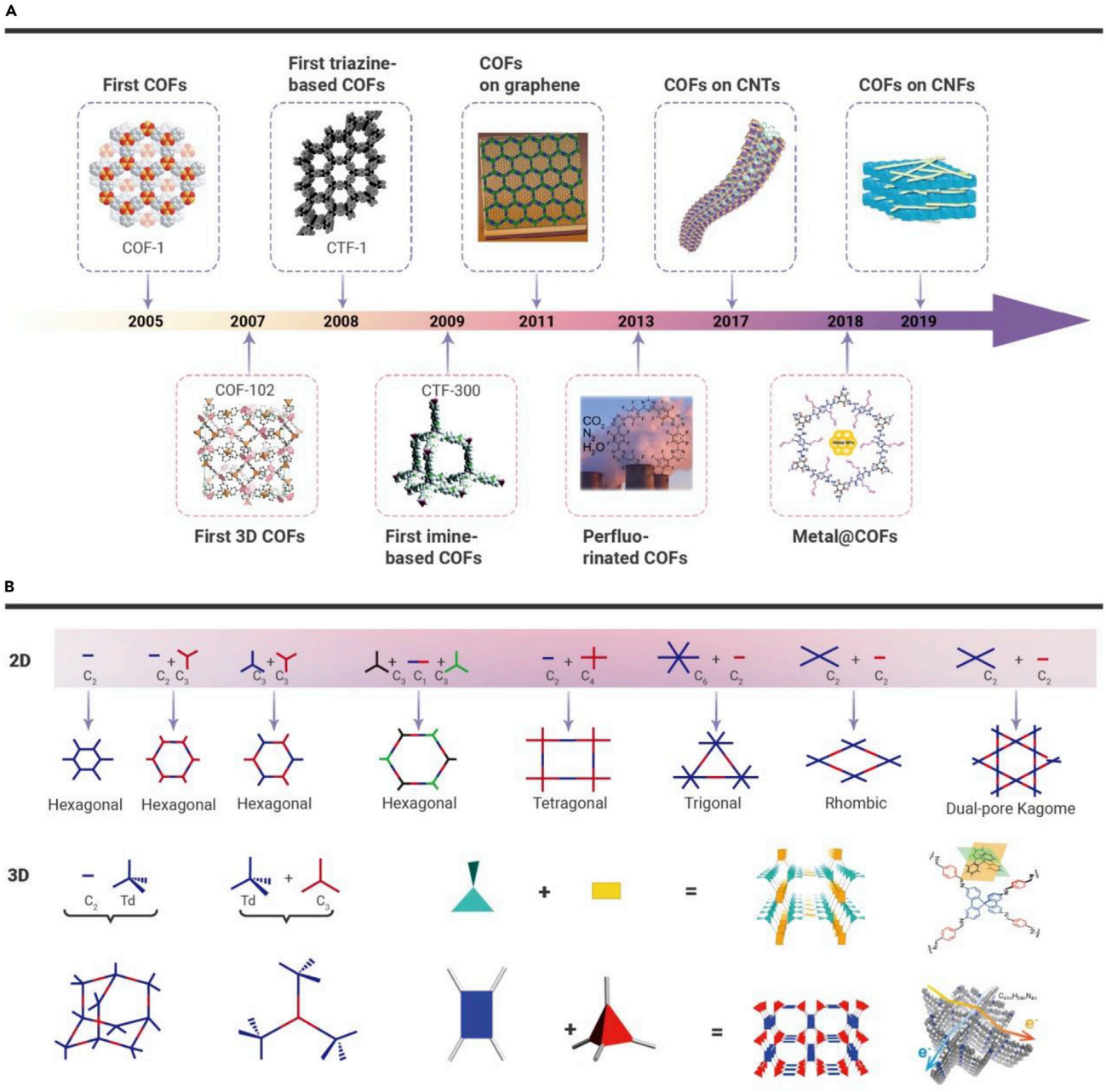

Figure 1. Synthesis of COF-based Materials (A) Developmental milestones of COF-based materials: single COFs to functionalized COFs.[2,25–32] (B) Sample of topologies accessible through COF synthesis.[33–37]

Since Yaghi and colleagues reported the first COFs in 2005,[28] numerous papers have been published on utilizing these innovative materials in different applications. Low mass density, high thermal stability, permanent porosity, and large specific surface make COFs one of the most widely used materials in environmental pollution management. Compared with traditional adsorbents, COFs not only possess some common features but also many possess special advantages, such as (1) orderly porous channels offer abundant adsorption sites and accelerate the fast diffusion of pollutants; (2) the easily adjustable pore size and shape of COFs provide the possibility for the separation of different contaminants; (3) COFs with strong covalent bonds show high chemical and thermal stability; and (4) low density of COFs implies that they have high adsorption capacity. These advantages, together with the characteristics of predesigned structure, ordered porous structure, and adjustable physicochemical properties, make COFs promising next-generation materials with remarkable high sorption capacities for radioactive/toxic metal ions and organic contaminants.[48,49–71,72–89,90–115]

Water Decontamination

With the rapid growth of industrialization, water pollutants remain a serious issue of public health and environmental protection. Toxic heavy metal ions (e.g., Hg^{2+}, Pb^{2+}, Cd^{2+}, and Cu^{2+}), radionuclides (e.g., ^{128}Pd, ^{137}Cs, ^{89}Sr, ^{235}U, ^{79}Se, ^{99}Tc, ^{137}Cs, ^{59}Fe, ^{57}Co, ^{65}Zn, ^{153}Eu, and ^{129}I) in nuclear waste, and organic pollutants (e.g., Bisphenol A [BPA], methylene blue [MB], rhodamine B [RhB], CR, Methyl orange [MO], polycyclic aromatic hydrocarbons [PAHs], Sulfamerazine [SMT], and pharmaceutical ibuprofen) in industrial wastewater are the primary pollutants in aqueous solutions that accumulate in living organisms and further create a severe threat to humans and other species through the food chain.

Pollution sources containing heavy metal ions are created during the rapid development of mining, machinery manufacturing, chemical, electronics, instrumentation, and other industries. Heavy metal ions present in surface water are difficult to be degraded into clean and eco-friendly substances, and have the potential to induce acute and chronic toxicity on aquatic biota.[116] The highly toxic or carcinogenic heavy metals accumulate in living organisms and further cause great threat for human health. For example, mercury poisoning can cause severe injuries to basic cellular processes, brain tissue, kidney, and liver via its progressive accumulation, and multiple toxicity. Therefore, efficient separation and enrichment of notorious heavy metal ions in aqueous solution is still a necessary but challenging task for environmental pollution treatment.

As a distinguished new energy source, nuclear power, frequently referred to as the "solving the energy crisis," has recently received attention because of its ability to satisfy basic energy requirements and relieve energy pressures. However, the extensive operation and utilization of nuclear energy undisputedly produces radioactive pollution.[117] For example, the harmful effects of U(VI) include inducing leukemia, nervous system disease, cancer, kidney failure, and even death. According to WHO standards, the maximum concentration level of U in normal water is 50 $\mu g \cdot L^{-1}$.[118] Therefore, accelerating the enrichment of radionuclides in the environment is of considerable significance to public safety and environmental protection.

Organic contaminants are also a significant part of water pollution, and they mostly originate from artificial organic matter, such as organochlorine pesticides, synthetic detergents, and synthetic dyes. Organic pollutants, such as endocrine interferon BPA, organic dyes (such as MB, RhB, CR, and MO), organic pesticides, PAHs and their derivatives, sulfonamides, and tetracyclines, exist in the environment ubiquitously.[119] Their discharge into the environment affects not only human beings, but also all living organisms. In particular, persistent organic pollutants (POPs) have the characteristics of high toxicity, long-term residuality, high solubility, and are degradation resistant. Ingestion of small amounts may cause cancer and malformation. Organic pollutants are diversified and complicated, and most of them are poorly degraded totally in a short time by environmental self-purification. Hence, searching for efficient and practical strategies to decontaminate organic pollutants remains a severe challenge.

Environmental Adsorption Techniques

Adsorption technology has been widely used in the purification of environmental pollutants by taking advantage of the high adsorption capacities of adsorbents to remove specific pollutants. Generally, adsorbents are required to possess large specific surface area, high adsorption performance, outstanding selectivity, excellent chemical and thermal stability, are cheap, and have good regeneration and reusability. Adsorption behavior is affected by pollutant properties, pH values, coexisting substances, temperature, contact time, and adsorbent dosage. To our knowledge, adsorption mechanisms include ion exchange, electrostatic adsorption, hydrogen bonding, specific surface bonding, and chelation. Various techniques, such as Fourier transform infrared (FTIR) spectroscopy, X-ray photoelectron spectroscopy (XPS), X-ray absorption fine structure (XAFS) spectroscopy, density functional theory (DFT) calculation, and molecular simulations are commonly applied to unveil internal adsorption mechanism.[120] In the section entitled "Mechanism analysis of pollutants removal by COF-based materials," these techniques are discussed systematically.

Over the past few decades, enormous research about natural and man-made adsorbents, such as clays,[121,122] ACs,[123] organic resins,[124,125] CNTs,[126–128] order mesoporous carbon (OMC),[129] carbonaceous materials,[130–132] graphene oxide (GO),[133–139] metal oxides,[140,141] layered double hydroxides (LDHs),[142–145] and layered metal sulfides (LMS),[146] have been applied in pollution cleanup. However, these materials suffered from some insufficiencies: (1) LDHs and clays exhibit slow sorption kinetics and limited selectivity; (2) ACs and carbonaceous materials possess disadvantages of small pore volumes or pore sizes; (3) GO and CNTs are complicated to synthesize and produce; (4) the poor regeneration and reusability of organic resins; and (5) relatively low chemical and thermal stability of LMS.[147] Novel nanomaterials, such as polymer adsorbents,[148] 2D MXenes,[149–153] nanoscale zero-valent iron (NZVI),[154–159] g-C_3N_4,[120,160–164] MOFs,[165–168] and COFs,[169–171] are constantly applied to improve their applications in environmental pollution cleanup owing to their superior performance. MOFs and COFs represent porous crystalline materials for network topology. However, compared with MOFs, COFs showed superior structure and performance as adsorbents. COFs have low mass densities, which implies that COFs show higher adsorption capacity when pollutants fully occupy both COFs and MOFs of the same mass. In addition, tailoring and designing the pore structure of COFs is relatively easy, providing more options for selective elimination of target pollutants. In addition, pore-wall engineering can be used to endow COFs with more active adsorptive sites.[36]

To date, various traditional or advanced techniques, including adsorption, electrocoagulation, chemical precipitation, ultrafiltration, evaporative recovery, solvent extraction, reverse osmosis, photocatalysis, oxidation/reduction, biological treatments, membrane separation, and filtration, have been applied to eliminate pollutants from wastewater. However, most of these methods have some unavoidable disadvantages. For instance, although membrane separation is highly efficient, its low economic viability and high maintenance costs restrict its application in large scale. Precipitation and biological treatments are cost-effective but they are unable to reduce the levels of pollutants below the necessary limits and can produce abundant sludge.[172] Photocatalysis generally faces the problems of photoetching, rapid recombination of electron hole pairs, and catalyst ion aggregation.[173] Although adsorption technology has the disadvantage that parsing waste liquid is difficult to treat and that the pollutants cannot be degraded completely, adsorption is widely used, owing to its low-cost, simple operation environmental friendliness, simple regeneration, and large-scale application.[147,173]

The Purpose of This Review

To date, several reviews and monographs have systematically summarized the fundamental theory of COFs and their design synthesis, important structural properties, and applications. However, there are few reviews of COFs in environmental pollution management. A systematic summary about COFs and COF-based materials as adsorbents for the efficient removal of toxic metal ions, radionuclides, and organic pollutants is not available. In this review, we place the emphasis not only on the potential of COFs in practical applications but also on techniques for the characterization of their adsorption behaviors/mechanisms. Various methods for studying adsorption properties, including microscopic spectroscopic analysis and theoretical calculation, are summarized (Scheme 1). We believe that this review, focused on the emerging applications of COF-based materials in environmental pollution management, is of great importance for the future development of environmental pollution regulation and it also provides guiding strategies and clues for the design and synthesis of COF-based materials as high-performance adsorbents.

STRATEGIES FOR SYNTHESIS OF COFs AND COF-BASED MATERIALS

Basically, COF-based materials can be divided into four categories: boron-containing COFs, triazine-based COFs, imine-based COFs, and other COFs.[11] For certain applications, functional COFs should be constructed. The adsorption performances of COFs are controlled by their highly ordered framework structures, hydrophilicity, surface area, functionality, and pore size and distribution.[147] Like the construction of other functional materials, bottom-up, postmodification, and blending approaches are the general strategies for designing functional COFs (Figure 2).[36]

The Bottom-up Method

The bottom-up method is a straightforward but more difficult strategy for constructing functional COFs. It requires the selection of building units directly containing the functional moieties as monomers for COF synthesis. In addition, the functionalization of COFs can be achieved by a slight modification of monomers to COFs. The advantage is the homogeneous distribution of functional groups and the improved hydrothermal or chemical stability

Review

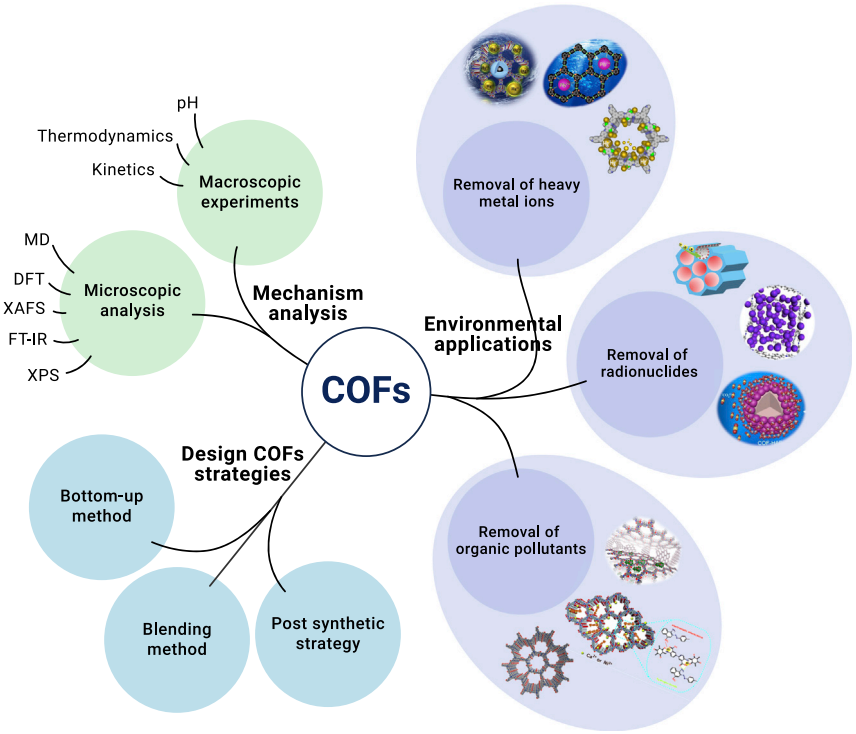

Scheme 1. Overview of this Article The design strategy that has been applied for the functional COFs is firstly introduced, followed by a systematic description of various toxic/radioactive metal ions and the adsorption properties of organic pollutants on COFs and their composites. Finally, the macroscopic/microscopic techniques used to analyze the adsorption mechanism are summarized.

of COFs. However, it causes more trouble in maintaining the structural regularity of the functional COFs.[174]

Designing efficient adsorbents with high abundance active sites is of significance to achieve quick uptake and high capacity for target pollutants. To date, organic building units, containing hydroxyl,[175] carboxyl,[176,177] phosphate groups,[178] amide groups,[179] and sulfide functional termini,[48] have been successfully used for functional COF synthesis. Oxygen in hydroxyl provides an open chelate site to bind Cd^{2+},[175] amide groups on COF skeletons are active sites for Pb^{2+},[179] and carboxyl groups on COFs significantly facilitate the dye adsorption.[177] In an interesting report,[178] functional COFs (P-WCA-POFs with $[P(O_2Ph)_3]^-$) have shown a nonideal performance because the nickel coupling agent blocked the pore opening during the reaction. After washing them with concentrated HCl, the obtained PA-POFs have shown a maximum adsorption capacity of 3,366 $mg \cdot g^{-1}$ for BPA, which is attributed to the removal of Ni impurities and more pores are created when P-O bonds are broken and ligands are etched away by the acid. This also indicates that COFs with free active functional groups could be used for further postmodification to acquire the best performance.

Postsynthesis Strategy

Postsynthesis strategy is most frequently used to prepare functional COFs. Subsequent modification, such as grafting or structural tailoring, can introduce functional moieties into the COF networks.[180] Besides, COF linkages are also transformed via chemical reactions.

The free functional groups in the COF skeleton are used as reaction anchors (e.g., -OH,[72,175] -CN[181] -C=C-,[182,183] and -C≡C-,[184,185]) and chemical modification is carried out through various reactions, including esterification reaction, "click reaction," and others. Besides, other chemical reactions, such as N-H bond deprotonation, enolketo tautomerism, and imine-amide transformation of COF linkages, are also adopted for structure modification.[36] Postmodified COF-COOCa and COF-COONi are obtained via embedded Ca^{2+} ions and Ni^{2+} ions in COF-COOH, respectively, and their adsorption capacity for CR is superior compared with that of COF-COOH, which is attributed to enhanced electrostatic interaction between metal ions and CR.[176] The simple treatment of CuP-DMNDA-COF with Fe(III) in acetone has led to the formation of Fe-coordinated COFs (CuP-DMNDA-COF/Fe),[186] which has shown ~100% RhB removal, while CuP-DMNDA-COF could only reach 20% RhB removal. The coordination interaction between Fe(III) ions in COF and the carboxy group of RhB plays a significant role in the excellent adsorption capacity of CuP-DMNDA-COF/Fe for RhB.

Postsynthesis strategies require specific anchor points on COFs as sites for later chemical modification. Postfunctionalized COFs exhibited intriguing adsorption performance for specific pollutants, which further signifies that the postsynthesis strategy is a facile, efficient, and practical functionalization strategy. However, the introduction of abrupt functional groups will affect the ordered crystal structure of COFs.

The Blending Method

The blending method could combine the functional materials to COFs to enable the elegant combinations of physicochemical properties, synergistic effects, and multiple functions of individual components. For adsorption, metal, graphene, and magnetic materials have been composited with COFs to increase their stability, selectivity, and adsorption capacity.[90,176,187]

Shapeless bulk materials are always formed in COFs, leading to an irregular morphology, because it is hard to control their growth rationally. Incorporation of COFs and magnetic nanoparticles has been confirmed as an effective strategy.[90] Solid spherical magnetic Fe_3O_4 cores can offer a center for COF growth and crystallization at all directions equally, which provides a possibility for controllable synthesis of magnetic core-shell COFs. Ag NPs@COF is formed by loading high dispersion of Ag on COFs and exhibits high Hg(II) ion removal efficiency from acidic water, which is interpreted by *in situ* formation of HgAg alloy.[40] In another fascinating study,[188] the use of baking soda to produce continuous CO_2, transforms 2D COFs into 3D COFs with ordered micropore structures, and synergistically allows different guests to quickly

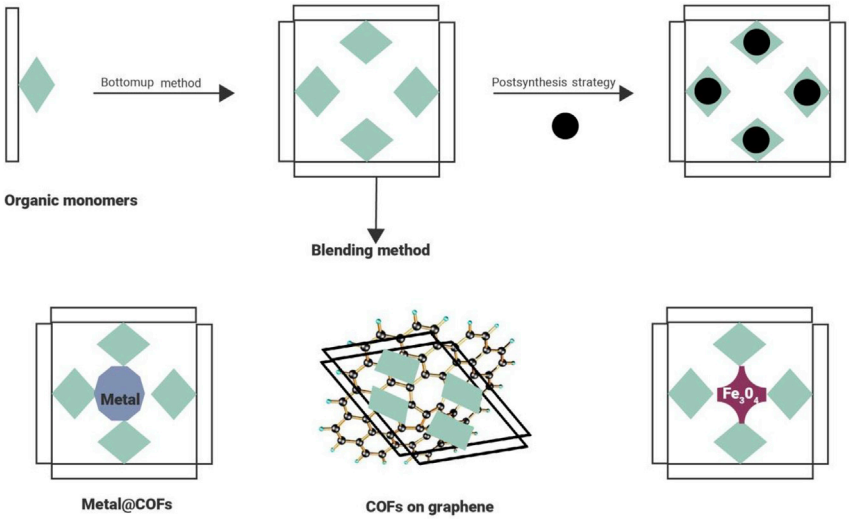

Figure 2. Functional Design Methods for COFs, the General Strategies for Designing Functional COFs Involve Bottom-up, Postmodification, and Blending Approaches

diffuse through the interconnected pore network. Blending COFs with other materials is an effective way to overcome the inherent shortcomings of COFs and accelerate their multidisciplinary applications.

REMOVAL OF TOXIC HEAVY METALS BY COF-BASED MATERIALS

"Heavy metals" refer to metals and metalloids with an atomic density of >4.5 $g \cdot cm^{-3}$ or more than five times of that of water, which are still toxic at low concentrations.[189,190] It will cause great harm to health if the cumulative concentration in the body exceeds the standard limit.[191,192] More importantly, unlike organic pollutants, heavy metals are very difficult to degrade into eco-friendly materials.[193]

Industrial wastewater containing heavy metals is usually acidic, so it requires adsorbents of high stability. Because COFs are connected by numerous strong covalent bonds, they are highly stable in strong acidic and basic conditions. The regular channels and adjustable pore size make it easier for the adsorbed heavy metal ions to diffuse in COFs uniformly and be captured effectively. Therefore, COF-based materials have good applications in removing heavy metals from wastewater.

Table 1 lists the adsorption performance and mechanism of COF-based materials for different heavy metal ions. The functional groups containing O, N, or S atoms have a good adsorption capacity for heavy metal ions. Therefore, through some elaborate designs, the integration of specific functional groups (e.g., -COOH, $-NH_2$, -CN, -SH, $-SCH_3$, and $-SO_3H$) into the framework of COFs will greatly improve the efficiency of metal ion removal. Currently, there are three main methods to synthesize COF-based materials with better adsorption performance: (1) directly synthesize COFs by selecting the building blocks containing specific functional groups; (2) prepare functionalized COFs by postsynthesis modification; and (3) combine COFs with other materials (such as metal nanoparticles and metal oxide). In practical applications, these methods are often combined reasonably.

Adsorption of Hg(II)

Hg can affect cell function and growth and even lead to cell necrosis by affecting intracellular metabolic pathways. Hg^{2+} can form stable covalent bonds with functional groups containing O, N, or S. In particular, the strong soft-soft interaction between sulfur derivatives and mercury has a strong affinity for Hg(II). Therefore, COFs and COF-based materials with high O, N, or S contents have a good effect on Hg adsorption.

Pristine COFs. O-, N-, or S-enriched COFs can be directly synthesized by selecting specific building blocks. Ding et al.[49] synthesized COF-LZU8 with thioether hydrazone bonding and applied it for Hg^{2+} removal with high selectivity, sensitivity and adsorption capacity. The rigid π conjugation structure acts as the fluorophore for signal sensing, and the evenly and densely distributed thioether side chains act as ion receptors for capturing Hg^{2+}. Huang et al.[48] synthesized an extremely stable TAPB-BMTTPA-COF by integrating the methyl sulfide units onto the edge of the phenyl groups and thus introducing sulfur-containing functional groups onto the COF skeleton. The shortest functional chain of sulfides is introduced, and these methyl sulfides are evenly distributed on the pore wall of COFs with high accessibility. The active sulfur sites could be fully exposed to capture Hg^{2+} with a saturated adsorption capacity of 734 $mg \cdot g^{-1}$. Li et al.[50] firstly proposed a solvent- and catalyst-free method to synthesize an azine-linked organic framework (ACOF) containing azide bonds. When ACOF adsorbs metal ions, its structure converts from enol to ketone form, which has stronger coordination with Hg(II) (175 $mg \cdot g^{-1}$). The structural transformation could improve ACOF adsorption performance. Li et al.[238] used Tp and flexible alkyl amine (ODH) as building blocks to synthesize a hydrazone-linked COF (TpODH). TpODH has irreversible enol-to-keto tautomerism and intramolecular hydrogen bonds with excellent crystallinity and stability. In addition, the large amount of oxygen and nitrogen in the skeleton of TpODH has strong electrostatic synergy and coordination for metal ions, i.e., Hg^{2+} (1,692 $mg \cdot g^{-1}$) and Cu^{2+} (324 $mg \cdot g^{-1}$). A 3D porous organic framework (POFct-1) with topological structure has been used to selectively remove Hg^{2+} and Cu^{2+},[51] and its color changes in the presence of hydrogen ions and visible light. The O-containing and N-containing functional groups of POFct-1 effectively adsorb Hg^{2+} and Cu^{2+} with adsorption capacities of 167.19 $mg \cdot g^{-1}$ (Hg^{2+}) and 135.60 $mg \cdot g^{-1}$ (Cu^{2+}). Cui et al.[52] used pyrene-based ligands (TFPPy) and a carbohydrazide linker (CHYD) to synthesize TFPPy-CHYD directly through a solvothermal route. Abundant secondary amine groups (-NH-) are evenly distributed on the pore wall of TFPPy-CHYD, and they are receptors to detect and remove Hg^{2+} selectively with a saturated adsorption capacity of 758 $mg \cdot g^{-1}$. The key advantage of TFPPy-CHYD is that the secondary amine groups could combine with Hg^{2+} reversibly. A novel stable triazine-based COF (T-COF)[53] could effectively adsorb Hg^{2+} in the solution within 15 min with a saturated adsorption capacity of 1,826 $mg \cdot g^{-1}$, which is attributed to the soft-soft interaction between N atoms in triazine and Hg^{2+}.

Modified COFs. Preparing functionalized COFs by postsynthesis modification is also an effective way to enhance the adsorption capability for heavy metal ions. Sun et al.[182] used 2,5-divinylterephthalaldehyde and 1,3,5-tris(4-aminophenyl)-benzene to synthesize vinyl-functionalized COF (COF-V). Then they modified COF-V with 1,2-ethanedithiol through thiol-ene "click" reaction to prepare COF-S-SH. The modified sulfur species has good accessibility, flexibility and density with strong affinity for soft metal ions, such as Hg^{2+}, Pb^{2+}, and Cu^{2+}. COF-S-SH could effectively remove Hg^{2+} from aqueous solution and gas phase, with a saturated adsorption capacity of

Table 1. The Adsorption Performance of COF-based Materials and Other Promising Materials to Various Heavy Metal Ions, Radionuclides, and Organic Pollutants

Materials	Target	Adsorption Equilibration Time (min)	Adsorption Capacity (mg g^{-1})	Adsorption Mechanism	Refs
COF-LZU8	Hg(II)	–	236	coordination of Hg and S atoms (thioether groups); electrostatic interaction	49
TAPB-DMTTPA-COF	Hg(II)	5	734	coordination of Hg and S atoms (thioether groups)	48
ACOF	Hg(II) U(VI)	5	175 169	interaction between Hg and keto groups (C=O)	50
TpODH	Hg(II) Cu(II)	~200	1,692 324	coordination of Hg and O and N atoms; electrostatic interaction	71
POFct-1	Hg(II) Cu(II)	720	167.19 135.60	coordination of Hg and O and N atoms	51
TFPPy-CHYD	Hg(II)	5	758	coordination of Hg and N atoms (-NH-)	52
T-COF	Hg(II)	15	1,826	coordination of Hg and N atoms; electrostatic interaction	53
COF-S-SH	Hg(II) Hg^0	10 3 d	1,350 863	coordination of Hg and S atoms (thiol and thioether groups)	182
COF-S-SH	Hg(II)	<50	588.2	coordination of Hg and S atoms	54
TPB-DMTP-COF-SH	Hg(II)	2	4,395	coordination of Hg and O and N and S atoms (triazole and thiol groups)	184
COF-SO_3H [NH_4^+][COF-SO_3^-]	Hg(II) Hg(II) Hg	10 10 12 h	1,033 1,299 932.6	coordination of Hg and O atoms (SO_3^-); coordination of Hg and O atoms (SO_3^-); ion exchange between NH_4^+ and Hg^{2+}	55
Fe_3O_4/M-COFs	Hg(II)	80	97.65	coordination of Hg and N atoms	56
M-COF-SH	Hg(II)	20	383	coordination of Hg and S atoms (thiol groups)	57
Ag NPs@COF-LZU1	Hg(II)	30	113	interaction between Hg and Ag nanoparticles	40
COF-TP COF-TE		~24 h	140 185.7	coordination of Pb and O and N atoms; electrostatic interaction	58
COOH@COF	Pb(II) Hg(II)	5	123.8 99.1	interaction between Hg/Pb and the carboxyl groups (-COOH)	179
COF-SH	Pb(II)	–	239	coordination of Pb and S atoms; electrostatic interaction	59
N-enriched COF	Cd(II)	20	396	coordination of Cd and N atoms; electrostatic interaction	60
COF-ETTA-2,3-Dha	Cd(II)	60	116	coordination of Cd and O atoms (ortho-dihydroxy groups)	175
COF-BTA-DHBZ	Cr(VI)	12 h	384	hydrogen bonds; electrostatic interaction	61
TpPa-1 Fe_3O_4@TpPa-1	Cr(VI)	60	310.8 245.45	hydrogen bonds; electrostatic interaction	62
COF1 COF2	Cr(VI)	–	462.85 635.06	hydrogen bonds; electrostatic interaction	63
QG-scaffolded COFs	Cu(II)	40 s	–	coordination of Cu and N atoms	64
TpPa-NH_2@EDTA	Ag(I), Pd(II), Cu(II), Ni(II), Fe(III), Cr(III)	5	~50	coordination of metal ions and EDTA	65
TTB-COF	Au(III)	1	560	coordination of Au and S atoms (thioether groups)	66
Fe^0/COFs	As(III)	–	135.78	hydrogen bonds; electrostatic interaction; As(III) is partially oxidized to As(V)	67
EB-COF:Br	As(V)	<1 h (DI water) 4–5 h (river)	53.1 (25°C) 27.5 (35°C) 5.1 (45°C)	hydrogen bonds; electrostatic interaction	68

(*Continued on next page*)

Table 1. *Continued*

Materials	Target	Adsorption Equilibration Time (min)	Adsorption Capacity (mg g^{-1})	Adsorption Mechanism	Refs
Glucan/chitosan (GL/CS) hydrogel	Cu(II) Co(II) Ni(II) Pb(II) Cd(II)	180	342 234 184 395 269	coordination of metal ions and O and N atoms	194
Magnetic graphene oxide (MGO)	Cd(II), As(V)	–	234 14	coordination of Cd and O atoms; electrostatic interaction; hydrogen bonds	195
Graphene/polydopamine modified multiwalled carbon nanotubes (MWCNT-PDA/GO)	Cu(II) Pb(II)	600	318.47 350.87	coordination of metal ions and O and N atoms; electrostatic interaction	196
Triamino-anchored monodispersed fibrous silica nanospheres (triamino-KCC-1)	Cr(VI)	~40	317	electrostatic interaction	197
Co-Fe_2O_3 Ni-Fe_2O_3 Fe_2O_3	Pb(II)	30 45	136.0 97.5 93.9	coordination of Pb and O atoms (hydroxyl groups)	198
Ni/Co-layered double hydroxide (NiCo-LDH)	Cr(VI)	80	99.9	electrostatic interaction; ion exchange	199
Nanoscale zero-valent iron (NZVI)	As(III)	<5 h <10 h	11.52	complexation, co-precipitation, and reduction	200
	Cd(II)		48.63		
	Pb(II)		85.37		
Graphitic-C_3N_4 (g-C_3N_4)	Co(II)	12 h	137.4	inner-sphere complexation	201
	Ni(II)		136.9		
	Cu(II)		134.1		
	Zn(II)		138.0		
Metal-organic framework-101 (MIL-101) iron-doped MIL-101 (Fe-MIL-101)	Pb(II)	90–120	57.96 86.20	coordination of Pb and O atoms (hydroxyl groups); electrostatic interaction	202
ZIF-8	Pb(II)	15 (2.0 g/L)	1,119.80	coordination of metal ions and N atoms	203
	Cu(II)	60 (0.5 g/L)	454.72		
ZIF-67	Pb(II)	120 (0.2 g/L)	1,348.42		
	Cu(II)	15	617.51		
COF-TpPa-1	U(VI)	300	152	chemisorption	76
COF-HBI	U(VI)	30	211	binding carboxyl groups	204
COF-COOH	U(VI)	120	213.8	binding carboxyl groups	204
COF-HAP	U(VI)	240	510	surface precipitation, complexation, and ion exchange	80
COF-TpAb-AO	U(VI)	90	408	coordination with amidoxime groups	181
o-GS-COF	U(VI)	20	144.2	coordination with oxime groups	81
COF-SO_3H	U(VI)	100	360	coordination interaction	82
$[NH_4]^+[COF\text{-}SO_3^-]$	U(VI)	100	851	coordination interaction and ion exchange	82
NFeU-AC	U(VI)	30	~20	surface complexation	205
CNFs	U(VI)	240	125	surface precipitation, complexation	130
MMT@C	U(VI)	300	20.76	inner-sphere surface complexation	206
Defective TiO_{2-x}	U(VI)	120	142	surface complexation	207
Fe_3O_4@LDHs	U(VI)	60	~30	chemisorption	208
nZVI/C	U(VI)	540	186.9	surface complexation	209
hypha/GO aerogel	U(VI)	30	288.4	coordination with carboxyl and hydroxyl groups	210

(*Continued on next page*)

Table 1. *Continued*

Materials	Target	Adsorption Equilibration Time (min)	Adsorption Capacity (mg g^{-1})	Adsorption Mechanism	Refs
PZS-TPP/CNT/Fe_3O_4	U(VI)	150	606	binding with polyphosphazene group	211
Fe@ZIF-8	U(VI)	720	277.7	chemisorption, surface complexation	212
azo-MOF	U(VI)	150	200	coordination with zao and amide units	213
TpPa-1-COF	Eu(III)	60	1107.6	chelating coordination	87
PAM/GO	Eu(III)	<720	189.2	strong complexation	214
g-C_3N_4 nanosheets	Eu(III)	<420	155	multilayer adsorption on heterogeneous surfaces	215
porous Al_2O_3	Eu(III)	25	223.37	hydroxy groups surface complexation	216
SCU-COF-1	TcO_4^-	1	702.4	electrostatic and van der Waals interactions	217
$DhaTG_{Cl}$	TcO_4^-	5	437	guanidine and hydroxyl groups complexation	89
MOF- SCU-101	TcO_4^-	10	217	coordination with H bond	218
UiO-66-NH_2	TcO_4^-	<720	159	–	219
Fe_3O_4@TpBD	BPA	5 min	160.6	hydrogen bonding; π-π interaction	90
Fe_3O_4@TpND	BPA	10 min	115.0	hydrogen bonding; surface complexation	91
TPT-DMBD-COF	MB	60 min	45.5	electrostatic attraction; π-π interaction	96
TPT-TAPB-COF	RhB	90 min	970.0	homogeneous adsorption	99
CuP-DMNDA-COF/Fe	RhB	–	378.0	surface complexation	186
COF-COONi	CR	120 min	781.3	electrostatic attraction; hydrogen bonding; π-π interaction	176
COF-TzDBd	CV	15 min	307.7	electrostatic attraction; π-π interaction; different size values	177
TPB-DMTP-COF	sulfamerazine	80 min	209.0	C–H···π interaction; electrostatic attraction	170
Magnetic TPB-DMTP-COF	diclofenac	50 min	109.0	C–H···π interaction; π-π interaction	169
NCCT	cefotaxime	8 h	309.3	electrostatic attraction; hydrogen bonding; π-π interaction	108
COF-3	TPhP	12 h	371.2	hydrogen bonding; π-π interaction; different size values	112
COFs	2-nitrophenol	90 min	239.9	π-π interaction; different size values; surface complexation	110
DhaTab-PBA	catechol	40 min	160.0	π-π interaction; homogeneous adsorption	113
TpBD-Me_2-COF	okadaic acid	60 min	279.0	heterogeneous adsorption	115

1,350 mg·g^{-1} for Hg^{2+} and 863 mg·g^{-1} for Hg^0. Similarly, Li et al.[54] selected a new triamino-monomer (TABPB) as a linker to synthesize a new kind of COF-S-SH, but its saturated adsorption capacity is lower (588.2 mg·g^{-1} for Hg^{2+}). Meri-Bofi et al.[184] synthesized TPB-DMTP-COF-SH by introducing triazole and thiol groups into the skeleton of COF. TPB-DMTP-COF-SH has the highest removal efficiency of Hg^{2+} (4,395 mg·g^{-1}) because of the strong synergistic chelation of triazole and thiol groups with Hg^{2+}. Tao et al.[55] reported a SO_3^--anchored COF material ([NH_4^+] [COF-SO_3^-]), which could selectively adsorb Hg^{2+} and Hg^0 through ion exchange with NH_4^+ and then be captured by independent SO_3^- cells through Hg-O coordination.

COF-based Composites. The performance of COFs can be improved by combining them with other materials. Magnetic COF composites are prepared by combining the COFs with iron oxide nanoparticles or other magnetic materials. On the basis of retaining their original excellent properties, it cannot only improve the adsorption performance but also facilitate solid-liquid separation. Ge et al.[56] prepared amino-functionalized Fe_3O_4-modified melamine-based COFs (M-COF) by a microwave method. The high density of N-containing groups could remove Hg^{2+} from wastewater selectively. The amino-functionalized Fe_3O_4 has excellent dispersivity and endows the COF composites with magnetism. Huang et al.[57] synthesized thiol-functionalized COFs (M-COF-SH) by using disulfide derivatives as specific building blocks. The thiol functional groups in M-COF-SH have a good chelating ability to Hg^{2+} within 10 min to achieve equilibration. This subsequent cutting strategy provides a new method for postsynthesis modification. In the report of Wang et al.,[40] Ag NPs@COF-LZU1 loaded with Ag nanoparticles was successfully prepared. Due to the large number of N-containing groups on COF skeleton, the stability and catalytic activity of Ag NPs could be promoted. The strong interaction between Ag and Hg could reduce Hg^{2+} to Hg^0 and form an Ag Hg nanoalloy, and thereby could remove Hg^{2+} in acidic aqueous solution effectively.

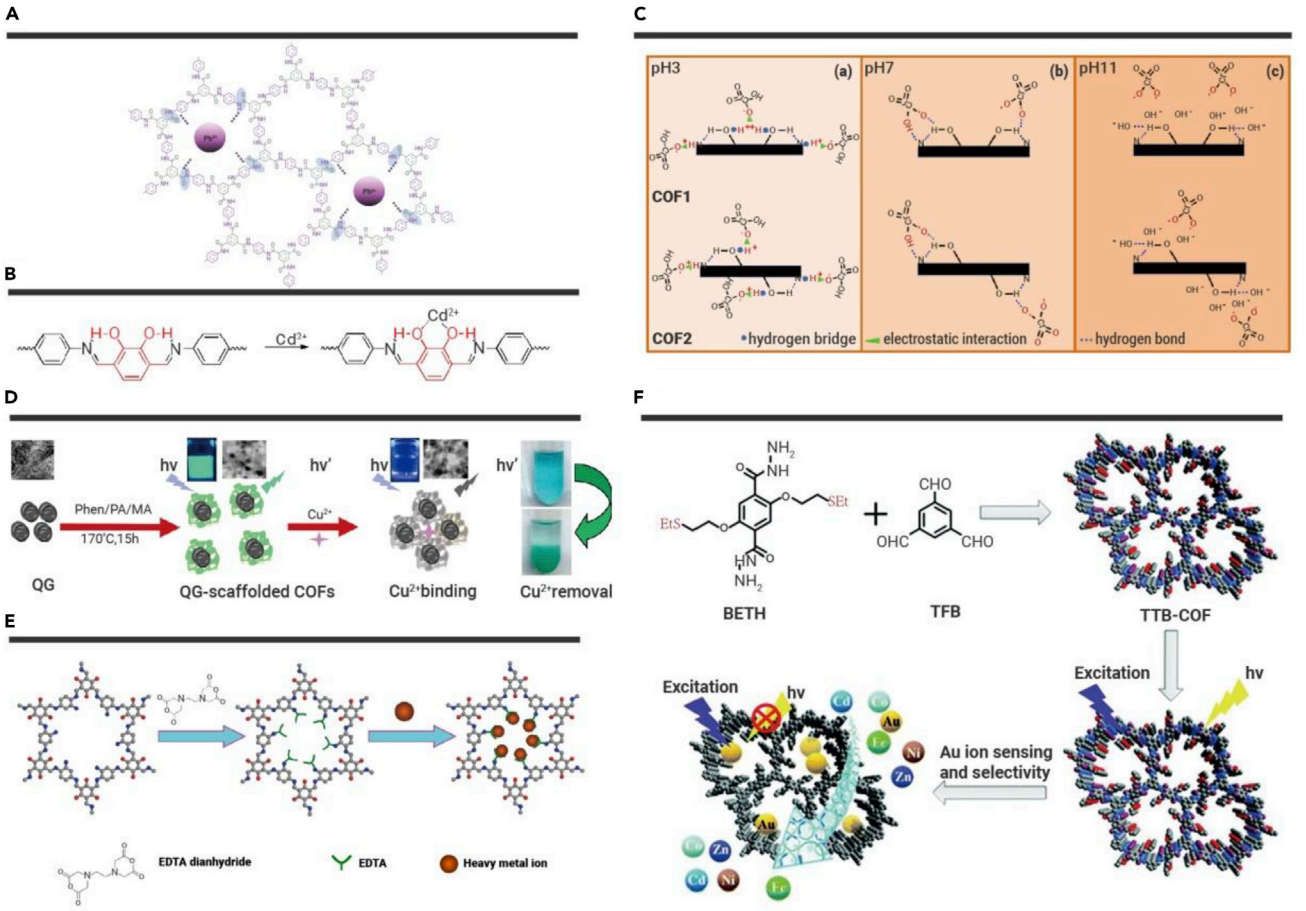

Figure 3. The Adsorption Mechanism of COF-based Materials for Some Heavy Metal Ions (A) Multi-coordination of Pb^{2+} with the amide groups in the structure pore of COF-TP.[179] (B) The intramolecular hydrogen bonding and chelation between a cadmium ion and the ortho-dihydroxy unit.[175] (C) The adsorption mechanism of Cr(VI) by COF1 and COF2.[63] (D) The fabrication of QG-scaffolded COFs with bright green fluorescence, which could be quenched by Cu^{2+} ions for Cu^{2+} removal.[64] (E) Synthesis of TpPa-NH_2@EDTA for the removal of heavy metal ions.[65] (F) Synthesis of TTB-COF and its application in selective detection and capture of Au ions.[66]

Adsorption of Pb(II)

Lead has a huge impact on the nervous system, immune system, and almost all other organ systems of the human body. It is known that O and N atoms have lone pairs of electrons to form coordination bonds with Pb^{2+}. Therefore, negatively charged ligands containing O and N atoms can form stable metal complexes with Pb^{2+}. Carboxyl-functionalized COFs (COOH@COF) prepared by postsynthesis modification have a good adsorption capacity and high selectivity for Hg^{2+} and Pb^{2+} with saturated adsorption capacities of 99.1 and 123.9 $mg \cdot g^{-1}$, respectively, due to the strong synergistic effect of carboxyl groups.[58] In particular, the adsorption capacity of COOH@COF remains almost constant after 20 cycles. Li et al.[179] synthesized two amide-rich layered COFs (COF-TP and COF-TE) and applied them for Pb^{2+} removal. Amide groups are considered as the active sites to capture Pb^{2+} through coordination with amido groups (Figure 3A), with saturated adsorption capacities of 140.0 and 185.7 $mg \cdot g^{-1}$ for COF-TP and COF-TE, respectively. COF-TE has better adsorption effect due to its fewer aromatic rings, weaker π-π stacking, larger layer spacing, and higher internal diffusion rate of Pb^{2+} compared with COF-TP. Interestingly, the removal efficiency of Pb^{2+} by the two materials is still above 95% after 10 cycles. Cao et al.[59] prepared a sulfhydryl functionalized COF (COF-SH) by a mild solvothermal solution suspension method. The large amount of sulfur substances distributed in the channels of COF-SH has a strong affinity with Pb^{2+} (239 $mg \cdot g^{-1}$) in solution due to the combined action of chelation and electrostatic attraction.

Adsorption of Cd(II)

Cadmium can cause anemia, hypertension, neuralgia, osteoporosis, nephritis, and other diseases. The well-known "Itai-Itai disease" is a typical case of chronic cadmium poisoning. Similar to Pb(II), the negatively charged COFs can absorb Cd^{2+} by electrostatic attraction, or use special functional groups containing O or N as active sites to capture Cd^{2+} through chelation. Dinari et al.[60] synthesized a novel N-enriched COF material through the condensation of triazine and trialdehyde. Due to the high N content and the accessible lone pairs of N electrons, it is easy to coordinate with Cd^{2+}. Moreover, the N-enriched COF would change into an anion form at high pH. The active centers are exposed, and have a strong electrostatic interaction with Cd^{2+} (396 $mg \cdot g^{-1}$). Liu et al.[175] successfully synthesized a novel heteropore COF (COF-ETTA-2,3-Dha) using a solvothermal method. In the crystal structure, there are triangular micropores and hexagonal mesopores with pore sizes of 5.9 and 26.3 Å, respectively. Due to the introduction of a catechol segment, intramolecular hydrogen bonds in the structure of COF could not only enhance stability but also provide accessible active sites. The ortho-dihydroxy groups could capture Cd^{2+} from solution by chelation (Figure 3B).

Adsorption of Cr(VI)

Cr(VI) has strong oxidability, which can cause carcinogenesis and teratogenesis, and its toxicity is about 100 times that of Cr(III). Cr(VI) exists in the form of oxyanions ($Cr_2O_7^{2-}$, $HCrO_4^-$, and CrO_4^{2-}) in water. So, the removal mechanism for metal cations is not applicable to Cr(VI). To improve the adsorption properties of COFs for Cr(VI), it is necessary to introduce

some specific functional groups that are easily protonated, such as -OH, $-NH_2$, and C=O, which can bind Cr(VI) effectively by electrostatic attraction or hydrogen bonds. It is worth noting that the adsorption of Cr(VI) is often accompanied by Cr(VI) reduction. Cui et al.[61] synthesized a dual-pore COF (COF-BTA-DHBZ) with hydroxyl groups and firstly applied it for Cr(VI) elimination. COF-BTA-DHBZ has triangular micropores and hexagonal mesopores with pore sizes of 12.7 and 22.0 Å, respectively. The density of hydroxyl is higher in triangular micropores, and the adsorbed Cr(VI) is mainly wrapped in triangular micropores. The hydroxyl groups could not only provide the active sites, but also reduce Cr(VI) to Cr(III). COF-BTA-DHBZ has shown fast adsorption kinetics and excellent adsorption capacity (384 $mg \cdot g^{-1}$). Zhong et al.[62] synthesized a novel magnetic COF material (Fe_3O_4@TpPa-1), and the amino groups of Fe_3O_4@TpPa-1 are changed into protonated cations ($-NH_3^+$) at pH 1.0, which had strong attraction to $HCrO_4^-$ and CrO_4^{2-}, so it could easily remove Cr(VI) from the solution. Zhu and colleagues[63] synthesized two kinds of COFs (COF1 and COF2) with different hydroxyl distributions. Due to the synergistic effect of electrostatic interaction and intramolecular hydrogen bonds, they could adsorb Cr(VI) effectively (462.85 $mg \cdot g^{-1}$ for COF1 and 635.06 $mg \cdot g^{-1}$ for COF2). Interestingly, the adsorption properties of the two materials are different at different Cr(VI) concentrations. At low concentration, the ortho-distribution of hydroxyl groups in COF1 is more conducive to adsorption, so the adsorption performance is better than that of COF2. However, at high concentration, the para-distribution of hydroxyl groups in COF2 could provide more active sites and thereby increases its adsorption performance (Figure 3C).

Adsorption of Other Heavy Metals

In recent years, there also have been a few reports about using COFs to adsorb heavy metals. Cai et al.[64] synthesized Q-graphene (QG)-scaffolded COFs (Figure 3D) to detect Cu^{2+} in solution and blood. QG-scaffolded COFs could not only detect Cu^{2+} but also remove Cu^{2+} effectively. Jiang et al.[65] synthesized TpPa-NH_2@EDTA by using EDTA to modify COF (Figure 3E). TpPa-NH_2@EDTA has a good adsorption effect on metal ions, such as soft Lewis acid (Ag^+, Pd^{2+}), borderline Lewis acid (Cu^{2+}, Ni^{2+}), and hard Lewis acid (Fe^{3+}, Cr^{3+}), with removal efficiencies of >85% within 5 min. Zhou et al.[66] synthesized a fluorescent thioether-functionalized COF (TTB-COF) to preconcentrate Au selectively in low concentrations (Figure 3F) with excellent stability. The strong coordination interaction between Au ions and S atoms in the thioether groups dominates the high Au adsorption (560 $mg \cdot g^{-1}$). The color of Au/TTB-COF has clearly changed from yellow to brown after treatment with Na_2S solution, suggesting the reduction of Au^{3+} to stable gold nanoparticles. Fe^0/TAPB-PDA[67] could adsorb As(III) from acidic wastewater in nonferrous smelting industry. The positively charged surface has electrostatic interaction with negatively charged As(III) species ($H_2AsO_3^-$). When the existing form of As(III) is H_3AsO_3, it could also form hydrogen bonds with the material. In addition, due to the presence of Fe^0, H_2O_2 and ·OH would be produced in the adsorption process to oxidize As(III) to As(V). Yang et al.[68] synthesized EB-COF:Br and applied it to remove As(V) from nearly neutral water. The $=N^+$ sites could produce electrostatic interaction with arsenate anions through the formation of hydrogen bonds with C-C=O groups.

Comparison between COF-based Materials and Other Materials in Removing Heavy Metals

Table 1 also lists some traditional materials for the removal of heavy metals. The adsorption kinetics of clay minerals, carbonaceous materials, and LDHs is slow, and the recyclability is poor. Metal oxides, mesoporous silica, and other materials are unstable under extremely alkaline or acidic conditions. NZVI has some advantages, such as large specific surface area, fast reaction rate, and rich active sites, but NZVI nanoparticles are easy to aggregate and oxidize. Mesoporous carbon nitride (CN) is a type of N-enriched material, which has triazine units in the structure that have a strong interaction with metal ions, but it is mainly used as a photocatalyst in the photocatalytic degradation of organic pollutants. MOFs have the advantages of high porosity, large specific surface area, and unsaturated metal sites. In contrast, COFs not only have the advantages of high porosity, large specific surface area, and stable structure, but also can be used as good modification platforms.

Functional groups, such as active amino, hydroxyl, and carboxyl groups, can be introduced into COFs through reasonable chemical modification. COFs have excellent adsorption performance because of their good adsorption capacity, fast adsorption kinetics, and great recyclability. Therefore, COFs have great application prospect and will remain a research hotspot in the future.

Strategy of Reduction and Immobilization

Due to limitations on the length of this paper, we only give the examples of heavy metal ion removal by adsorption. In fact, it is also a good strategy to reduce and fix heavy metal ions on COFs for heavy metal treatment. The adsorption of heavy metal ions by some COFs is often accompanied by a reduction reaction. For example, the toxicity of Cr(III) is much lower than that of Cr(VI); thus, Cr(VI) reduction to Cr(III) by using COFs has attracted a lot of attention.[69,70] The photoconductivity and photocatalytic activity of COFs can be improved by modifying specific groups on the skeleton or combining them with other materials. Therefore, it is a promising research direction to treat heavy metal ions with COFs through reduction and immobilization.

Some studies on the removal of heavy metal ions by COFs are listed here. Generally, the adsorption and removal mechanisms of COFs for heavy metal ions are as follows (1) adsorption to unsaturated coordination sites, (2) adsorption through electrostatic interaction, and (3) adsorption by forming hydrogen bonds. Through some elaborate designs, modifying some special functional groups on the skeleton of COFs will greatly improve their performance.

Although COFs are very promising materials for the removal of heavy metals, there are few studies on the adsorption of some heavy metals (such as Cd, Co, and Ni). Thus, there are still many challenges for the development of COFs in the adsorption of heavy metals: (1) there are few studies on the possible risk assessment of COFs on humans and the environment, (2) the key to improve the adsorption performance of COFs for heavy metal ions is to apply appropriate adsorption mechanisms and select better modified groups, and (3) it is necessary for the commercial availability of COFs to explore a simpler synthesis method, improve the yield, and reduce the preparation cost.

REMOVAL OF RADIONUCLIDES BY COF-BASED MATERIALS

With the continuous increase of human demand for energy, nuclear energy has gradually been considered as a very important and necessary energy source.[220] Although nuclear energy has the advantages of being clean and renewable, the generation of nuclear waste is a tricky question.[221] The release of radionuclides into the ecosystem poses a huge threat to the environment and seriously affects the safety of humans and other organisms.[222,223] Thus, the effective capture of radionuclides will bring huge gains to humanity.[223–225] Because of the high chemical stability and postsynthesis modification with functional groups,[226,227] COFs exhibit promising acid stability that can easily maintain original morphology and chemical property in acid conditions of 3 M, some even in conditions of 8 M.[217,228] Up to now, we have simply divided COFs into three groups, namely, single COFs, organic-group-functionalized COFs, and COF-based composites. By introducing functional groups, metal ions, or other materials into COFs, the adsorption performance toward radionuclides will be significantly improved.

Removal of U(VI)

Uranium is an actinide element, which generally exists as UO_2^{2+} in radioactive waste.[73] Long-time exposure to U(VI) can lead to liver damage and cancer risk.[74] US EPA set the acceptable limitation of <30 ppb for uranium levels in drinking water.[75] Thus, it is vital to remove U(VI) ions to ensure environmental safety. Recent progress regarding the adsorption of U(VI) on COFs and derivates is summarized in the succeeding subsections.

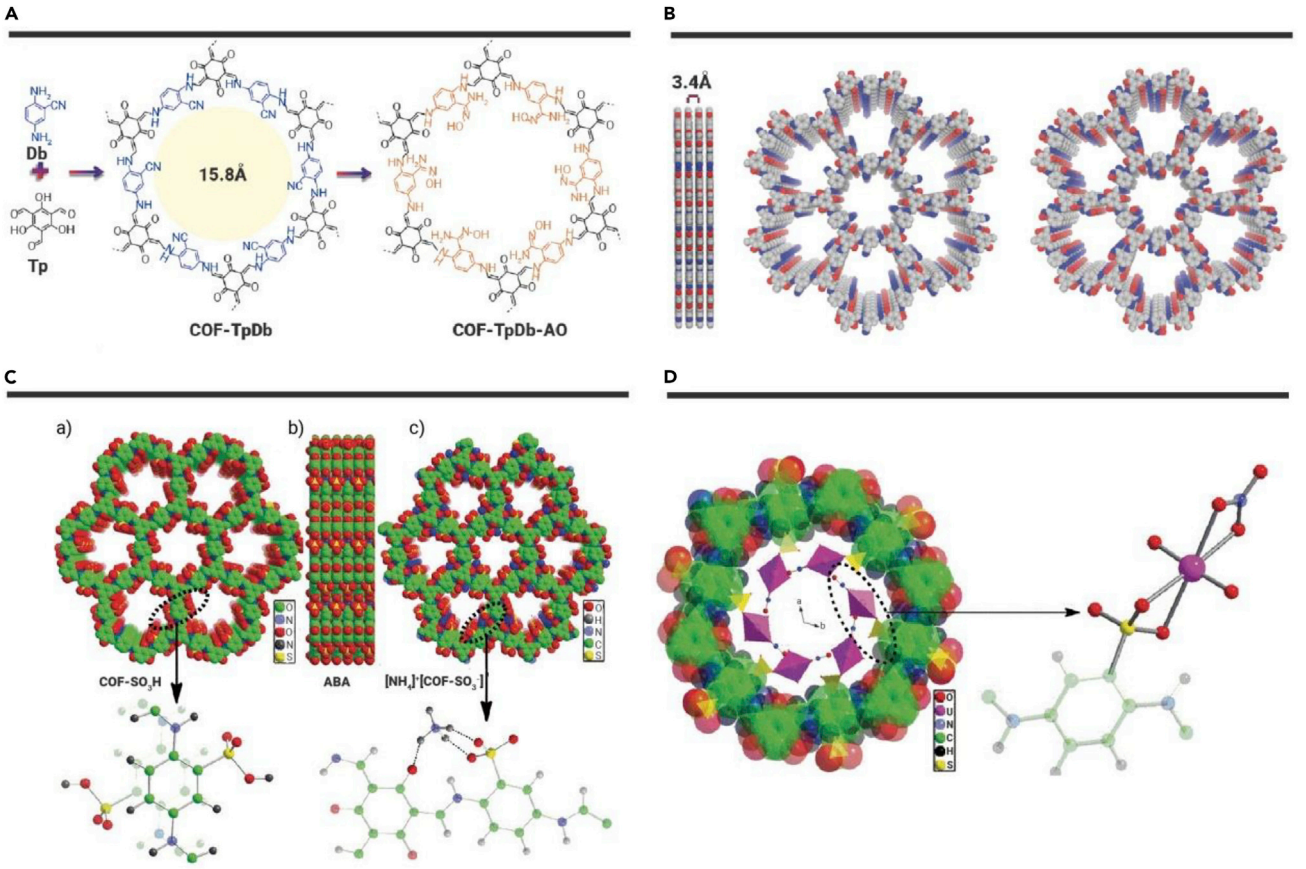

Figure 4. Modification of COF Structures (A) Synthetic scheme of COF-TpDb-AO. (B–D) (B) Graphic view of the eclipsed AA stacking structure of COF-TpDb and COF-TpDb-AO.[181] (C) Space-filling view of the structure of (a and b) COF-SO_3H and (c) $[NH_4]^+[COF\text{-}SO_3^-]$. The COF-$SO_3H$ shows the ABA stacking fashion, which means that the arrangement of -SO_3H in the layers (a) and (b) is in the opposite mode rather than the common same-side mode (see the insert); the location of NH_4^+ and the hydrogen bond interactions between NH_4^+ and COF skeleton are highlighted (see the insert). (D) View of the DFT optimized uranyl-loaded structure for the $[NH_4]^+[COF\text{-}SO_3^-]$ samples.[82]

Pristine COFs. Li et al.[76] synthesized a single COF-TpPa-1 using a solvothermal method. The COF-TpPa-1 has shown no significant difference before and after U(VI) adsorption, suggesting its high chemical stability after U(VI) loading. The adsorption of U(VI) onto this single COF-TpPa-1 is dependent on the completion of the chemisorption monolayer. The main adsorption capability results from surface physisorption rather than selective affinity, complexation, and ion exchange. Thus, the amount of uranium ions removed by single COFs is distinctively less than that of functionalized COFs and COF composites (Table 1).

Modified COFs. Numerous studies have confirmed that the functionalization of pristine COFs is an effective way to enhance their sorption performance.[77–79] You et al.[80] synthesized a COF-HAP composite using a solvothermal method to enhance U(VI) adsorption through the carboxyl groups by surface complexation. The uranyl cation is regarded as a strong Lewis acid with high affinity for hard oxygen donors, including carboxylate and hydroxide. In addition, the hydroxyl apatite in the COF-HAP could ionize partially under acidic conditions, which produces a spot of Ca^{2+} and PO_4^{3-} ions to immobilize UO_2^{2+} by surface precipitation. The introduction of the amino groups neighboring the amidoxime could alter the electron density of the complex, which could lower the overall charge of uranyl and provide an additional hydrogen bonding site to align uranyl species in a favorable coordination fashion, thereby increasing the affinity toward uranyl. Sun et al.[181] synthesized amidoxime-functionalized COFs (Figure 4A) for U(VI) extraction from potable water, well water, river water, and seawater. The U(VI) concentrations in these water samples could be reduced to less than 0.1 ppb with a single treatment by COFs. The ordered pore channels of COFs could facilitate the chelating groups to trap U(VI) ions. In addition, the stacking structure (Figure 4B) highly enhances U(VI) mobility, which again increases the contact opportunity between U(VI) ions and chelating groups. The selectivity of AO groups to U(VI) is attributed to the thermodynamically favorable η^2-binding interaction and strong chelating ability of amidoxime groups with U(VI). Based on XPS and FTIR analysis, the binding energy of U $4f_{5/2}$ of U@COF-AO (~392.4 eV) is lower than that of $UO_2(NO_3)\cdot 6H_2O$ (393.4 eV), and a significant red shift of antisymmetric vibrations of UO_2^{2+} for U@COF-AO (~933 cm^{-1}) compared with $UO_2(NO_3)\cdot 6H_2O$ (960 cm^{-1}) demonstrated the interaction between U(VI) and AO. The binding energies of N 1s XPS spectra (~400 eV) of GO-COF before and after U(VI) adsorption are almost unchanged, yet a distinct shift of O 1s is observed, revealing the high efficient interaction of O-containing groups rather than N-containing groups.[81] Thus, amidoxime- and oximation-modified COFs could serve as potential candidates for U(VI) uptake. The introduction of functional groups enhances the selective affinity of the COF skeleton toward radionuclides but, at the same time, the large cost of synthesis and little amount of production may limit industrial use of factories. Thus, a great effort still needs to be taken to optimize real practical applications.

COF-based Composites. With delicately and rationally designed properties, COFs combined with other materials can achieve considerably high adsorption performance because of synergistic effects. Wen et al.[81] prepared oximation-functionalized and graphene-synergized 2D COF (*o*-GS-COF). The π-π interaction strengthens the interconnection of active functional groups located in the interlayer and intralayer of the lamellar structure. This composite maintains effective adsorption when pH is >2, owing to the comprehensive influences derived from mutual intercalation and the supporting effects of the two participating materials. GO and TDCOF in the composite not only lead to a significant increase of specific surface area of GS-COF but also introduce TDCOF into GO. The adsorption capacity of this composite is

improved up to 221.1 $mg \cdot g^{-1}$ because the *o*-GO sheets offered additional adsorption sites. FTIR and XPS results show that U(VI) adsorption occurs due to definite coordination interactions. This composite also features better selectivity among 10 coexisting ions (Zn^{2+}, Co^{2+}, Ni^{2+}, Mn^{2+}, Sm^{3+}, Gd^{3+}, La^{3+}, Nd^{3+}, Sr^{2+}, and Ce^{3+}) and excellent acid stability after the treatment of 8 M HNO_3 for 12 h. Recently, Xiong et al.[82] synthesized COF-SO_3H with a combination of 2,4,6-triformylphloroglucinol and 1,2-dichlorobenzene, and then prepared $[NH_4]^+$[COF-SO_3^-] by immersing COF-SO_3H in $NH_3 \cdot H_2O$. The abundant $-SO_3^-$ units in the pore wall could implement the coordination interaction toward U(VI). The introduced abundant NH_4^+ groups could serve as a deprotonation and U exchanger and thus could increase U(VI) removal efficiency (421 $mg \cdot g^{-1}$ for COF-SO_3H and 869 $mg \cdot g^{-1}$ for $[NH_4]^+$[COF-SO_3^-]), which has exceeded many reported adsorbents (Table 1). The ultrahigh adsorption capacity and rapid adsorption kinetics are due to a synergistic effect from the robust and chemically stable porous framework, ion exchange between $[NH_4]^+$ and U(VI), as well as strong chemical adsorption sites of abundant freestanding -SO_3^- units on the pore wall. In the infrared (IR) spectra, new peaks at 926 and 918 cm^{-1} in the COF-SO_3H and $[NH_4]^+$[COF-SO_3^-] samples are assigned to the antisymmetric vibration of uranyl ions, indicating the strong coordination interactions between uranyl ions and -SO_3^- groups. The adsorption ability in the real nuclear acid wastewater shows highly effective U(VI) adsorption at pH 1 and 8, giving 100% and 98% removal efficiency, respectively. NH_4^+ cations replace the position of H^+ and are adsorbed near sulfonic functional groups by triple hydrogen bonds with two sulfonic oxygen atoms. Uranyl adsorption on $[NH_4]^+$[COF-SO_3^-] was in a way that NH_4^+ is rapidly displaced by $(UO_2)NO_3^+$, firstly leading to the release of NH_4NO_3, and then $(UO_2)NO_3^+$ is bound by sulfonic units (Figures 4C and 4D).

Although the combined COF composites possess many advantages to separate U(VI), their application is currently limited to laboratory setting. In addition, most combined materials are easy to collapse or hydrolyze due to their weak structural affinity and intensity. Meanwhile, the manufacturing cost is too high. Thus, the real application of COFs and COF-based materials in the separation of U(VI) from wastewater in large scale is still a great challenge.

Removal of Other Radionuclides

Some other radionuclides, such as Eu^{3+}, Th^{4+}, TcO_4^-, ReO_4^-, $^{129}I^-$, Co^{2+}, Cs^+, and Sr^{2+}, are also highly hazardous to human health.[83–86] In recent years, COF-based materials have shown a great potential in the preconcentration of radionuclides from radioactive wastewater.

Pristine COFs. Single COFs have limited variety compared with functionalized COFs and COF-based composites. Their functionality mainly results from different raw material ligands and different pore sizes and pore topologies. For example, TpPa-1-COF is synthesized via Schiff-base reactions for Eu(III) removal from polluted water.[87] SEM images and XRD patterns have demonstrated the snow-flake-like morphology, loose-layered structure, and π-π stacking of TpPa-1. Single TpPa-1-COF maintains effective adsorption ability in the range of pH 2–8, which makes it promising for practical application in spent nuclear fuel postprocessing. The $Eu3d_{5/2}$ spectrum of TpPa-1-Eu can be disintegrated into two peaks at 1,134.65 and 1,136.98 eV, corresponding to -OH···Eu^{3+} and $(\equiv X)_3 \cdots Eu^0$, suggesting good affinity between Eu(III) and TpPa-1-COF. According to the Langmuir model, the maximum adsorption capacity of Eu(III) on TpPa-1-COF is 1,107.63 mg g^{-1} at pH 6.5 and T = 298 K, which is much higher than that reported for other materials (Table 1). Yin et al.[88] synthesized a novel heterospore single COF (SIOC-COF-7) with two different micropores. These unprecedented COFs exist as hollow microspheres and exhibit an extremely high volatile iodine uptake (up to 481 wt%) by encapsulating iodine in the inner cavities and porous shells of the microspheres. Brunauer-Emmett-Teller (BET) surface area is estimated to be 618 $m^2 \cdot g^{-1}$ from the isotherm data in the range of P/P_0 = 0.01–0.3. The pore size distribution, as reflected by nonlocal DFT, reveals two main pore size distributions at 5.0 and 11.8 Å. The formation of two kinds of channels (diameters of ~5 and ~12 Å) across the shells of the COF spheres cannot only accommodate iodine molecules but also facilitate the diffusion of iodine molecules into the inner cavities of the microspheres. He et al.[217] synthesized a radiation-resistant COF (SCU-COF-1), which exhibits ultrahigh acid stability and great resistance toward both high-dose β- and γ-irradiation and $^{99}TcO_4^-$ ultrahigh uptake capacity with extremely fast sorption kinetics to reach equilibration within 1 min and good anion-exchange selectivity. The almost unchanged characteristic BET surface area and vibrational peaks in the IR spectra of the samples treated with 3 M HNO_3 further underscore the acidic stability. In addition, PXRD discloses that SCU-COF-1 can retain its crystal structure in THF, DMF, H_2O, aqueous HNO_3 (1 and 3 M), aqueous HCl (1 M), and NaOH (1 M) solutions and after β-irradiation at 200, 400, and 600 kGy for 48 h. In the presence of high concentrations of SO_4^{2-}, CO_3^{2-}, and PO_4^{3-}, SCU-COF-1 still exhibits excellent selectivity with removal percentages from 85% to 99%. The high selectivity is due to the hydrophobicity of the COF skeleton, which provides remarkable affinity for hydrophobic anion with low charge density.

Modified COFs. The capture of $^{99}TcO_4^-$ from nuclear waste is extremely desirable for waste disposal and environmental restoration. Da et al.[89] synthesized functionalized guanidine-based hydrolytically stable cationic covalent organic nanosheets (i.e., iCON, which resulted from self-exfoliation of COFs by incorporating positively charged building blocks into the intralayer of COFs) named as $DhaTG_{Cl}$ for effective uptake of ReO_4^- (a nonradioactive surrogate of TcO_4^-). $DhaTG_{Cl}$ has shown extremely fast exchange kinetics toward ReO_4^- with a high uptake capacity of 437 $mg \cdot g^{-1}$ and prominent distribution coefficient of 5.0×10^5. Meanwhile, $DhaTG_{Cl}$ shows an excellent selective capture of ReO_4^- in the presence of NO_3^-, CO_3^{2-}, PO_4^{3-}, and SO_4^{2-} in a simulated Hanford LAW Melter Recycle Stream. The weak interaction between chlorine ions and the skeleton contributes to the exchange of ReO_4^-. Lu et al.[72] synthesized a 3D carboxyl-functionalized COF (3D-COOH-COF) for selective extraction of Nd^{3+} ions. The extraction of Nd^{3+} is much higher than that of Sr^{2+} and Fe^{3+}, which could be ascribed to the greater charge density and the larger ionic radius of Nd^{3+} relative to Sr^{2+} and Fe^{3+}. IAST results showed that Nd^{3+} can be isolated from Sr^{2+} and Fe^{3+} solutions at high purity, which suggests that the coordination environment and strength of the metal ion framework interactions are very uniform in 3D-COOH-COF. Carbon-13 nuclear magnetic resonance signal of carbons in the carboxyl groups downfield has shifted 2.9 nm, demonstrating the strong interaction between Nd^{3+} and the carboxyl groups in Nd/3D-COOH-COF. The negative shift of 3.6 eV in the XPS spectrum is evidence of the interaction between Nd^{3+} and the carboxyl groups in Nd/3D-COOH-COF.

Strategy of Reduction and Immobilization

The oxidized U(VI) is highly hazardous and soluble, while reduced U(IV) poses no evident threat to ecosystem and is easy to separate. Thus, the perniciousness of radioactive ions could also be eliminated by changing the valence state. The reduction of radionuclides mainly takes place in two ways, namely, electric reduction and photocatalytic reduction. However, electric reduction, mostly used in lithium storage,[229] hydrogen evolution,[230] and CO_2 reduction,[231] is rarely used for adsorption-reduction of radionuclides.

To have an efficient photocatalytic activity, a higher planar extended π-conjugated system is critical to transmit the electrons freely in the π system. Cui et al.[232] synthesized the highly planar conjugated naphthalene-based sp^2-carbon $COF_{NDA\text{-}TN\text{-}AO}$ and interrupted π-conjugated $COF_{NDA\text{-}TN\text{-}AO}$ (Figures 5A and 5B). The ESI and photocurrent response measurements have demonstrated that $COF_{NDA\text{-}TN\text{-}AO}$ outperforms $COF_{BDA\text{-}TN\text{-}AO}$, indicating a much more efficient separation of charge carriers and interfacial charge transfer in the highly planar π-conjugated $COF_{NDA\text{-}TN\text{-}AO}$ skeleton. The excellent photoelectric effect of $COF_{NDA\text{-}TN\text{-}AO}$ could effectively release electrons from the skeleton and form a positive surface electric field around the skeleton, which shows a strong electrostatic attraction to $[UO_2(CO_3)_3]^{4-}$ to increase the extraction capacity of uranium. After irradiation by simulated sunlight, the U(VI) adsorption capacity of $COF_{NDA\text{-}TN\text{-}AO}$ increases from 486.4 to 589.1 $mg \cdot g^{-1}$ (21.2% increase, Figure 5C), while light irradiation of

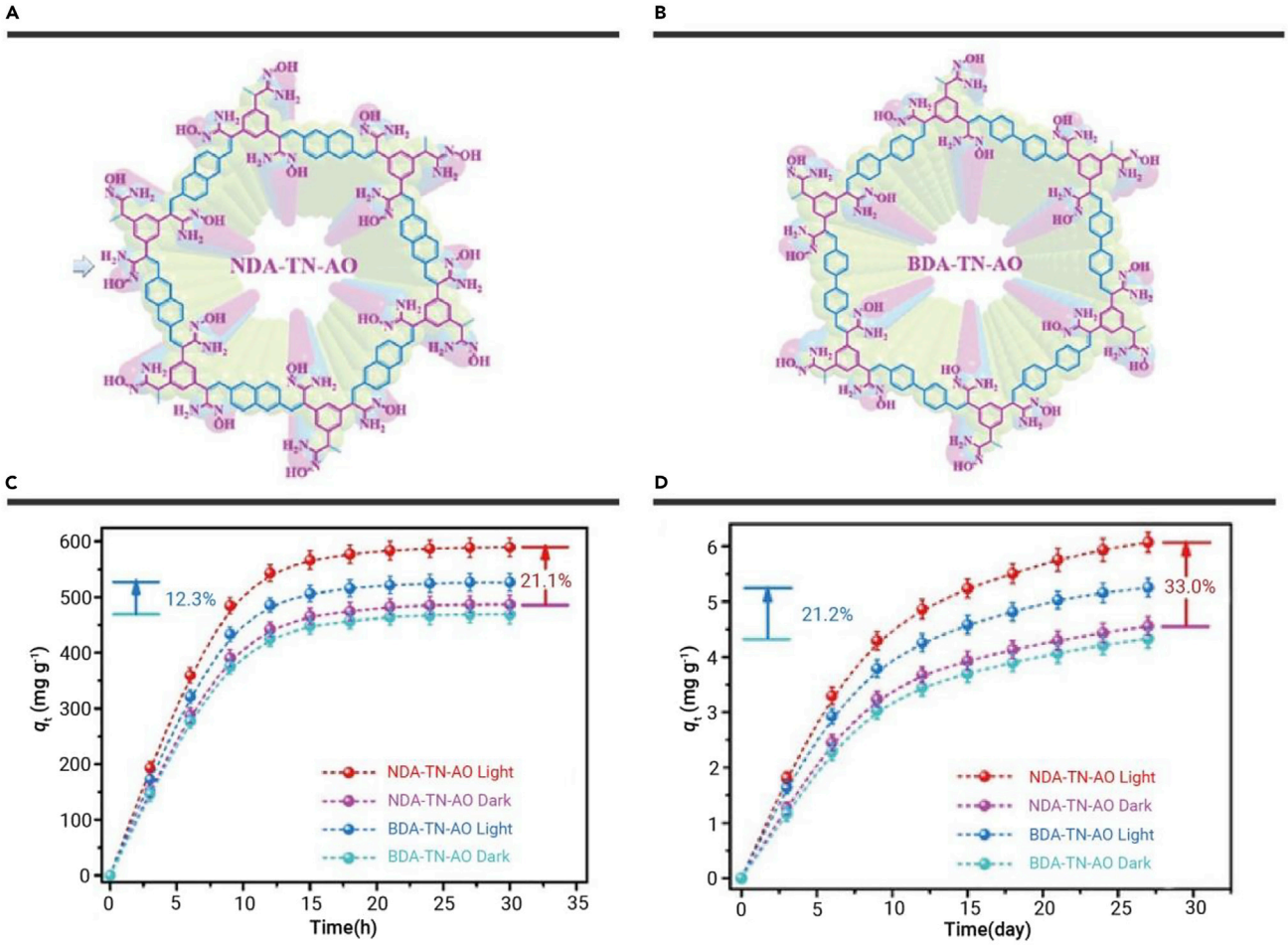

Figure 5. U(VI) Adsorption by Modified COF-based Materials (A) Fully planar π-conjugated BDATN-AO. (B) Interrupted π-conjugated NDA-TN-AO. (C) Uranium extraction capacity. (D) Adsorption of uranium from seawater.[232]

$COF_{BDA-TN-AO}$ only increases U(VI) adsorption capacity by 12.3%, which could be attributed to the much better photoelectric and photocatalytic activity of $COF_{NDA-TN-AO}$. XPS has demonstrated the coexistence of U(VI) and U(IV) under simulated sunlight irradiation. Under dark conditions, the adsorption capacities of $COF_{NDA-TN-AO}$ and $COF_{BDA-TN-AO}$ are 4.56 and 4.33 mg·g^{-1}, respectively. The uranium adsorption capacities of $COF_{NDA-TN-AO}$ and $COF_{BDA-TN-AO}$ increase by 33.0% and 21.2%, respectively, after 27 days of light exposure (Figure 5D), which is attributed to the photocatalytic and photoelectric activity.

Comparison between COF-based Materials and Other Adsorbents in Removing Radionuclides

Apart from the above-mentioned COF-based materials, many other COF-based materials have been applied for the adsorption of radionuclides (Table 1). Complexation and coordination are the main mechanisms of U(VI) sorption onto pristine COFs, owing to their highly ordered structures. For modified COFs and COF-based materials, coordination with the functional groups is an alternative interaction mechanism. The highest adsorption capacity for U(VI) has been reported to be 851 mg·g^{-1} for $[NH_4]^+$[COF-SO_3^-].[82] To the authors' knowledge, the most selective COF-based adsorbent for U(VI) reported to date is *o*-GS-COF.[81] The COF with the highest radiation stability reported is SCU-COF-1, which has been confirmed to maintain its physicochemical property even under irradiation of 600 kGy β-rays and 600 kGy γ-rays,[217] enough to meet the need of applications in radioactive waste management. As shown in Table 1, several COF-based materials have shown superior adsorption capacities, which are much higher than those of other widely used materials.

COF-BASED MATERIALS FOR ORGANIC POLLUTANTS ELIMINATION

Organic pollutants extensively exist in industry and agriculture production, arousing great attention.[233–235] In this section, the elimination of serval categories of pollutants by novel COF-based materials is summarized and analyzed. Also, different removal strategies, such as magnetic solid-phase extraction, solid-phase microextraction, membrane filtration, and interfacial adsorption are mentioned and described.

Removal of Bisphenol A

Over the last decades, endocrine-disrupting chemicals have been detected in various natural aqueous solutions due to their extensive applications in the fields of polycarbonate plastics, epikotes, flame retardants, and pesticides among others. BPA is a typical endocrine disruptor, which can result in hormone disorder, heart disease, and abnormal liver function in humans even in ultralow concentrations.[236] Here, the adsorption behaviors of BPA by different kinds of COF-based materials are summarized and discussed.

Magnetic COF-based materials are widely investigated due to their practicability and efficiency with regard to magnetic separation. Li et al.[90] reported a core-shell Fe_3O_4@TpBD with an inner core of super-paramagnetic Fe_3O_4 and a TpBD shell. Amino groups are introduced on the surface of Fe_3O_4 for pregrafting of the TpBD monomer (Figure 6A). The adsorption of BPA on Fe_3O_4@TpBD has shown equilibrium within 5 min with a maximum sorption capacity of 160.6 mg·g^{-1}. Hydrogen bonding and a π-π interaction between the benzene ring and BPA are the main removal mechanisms. Recently, our

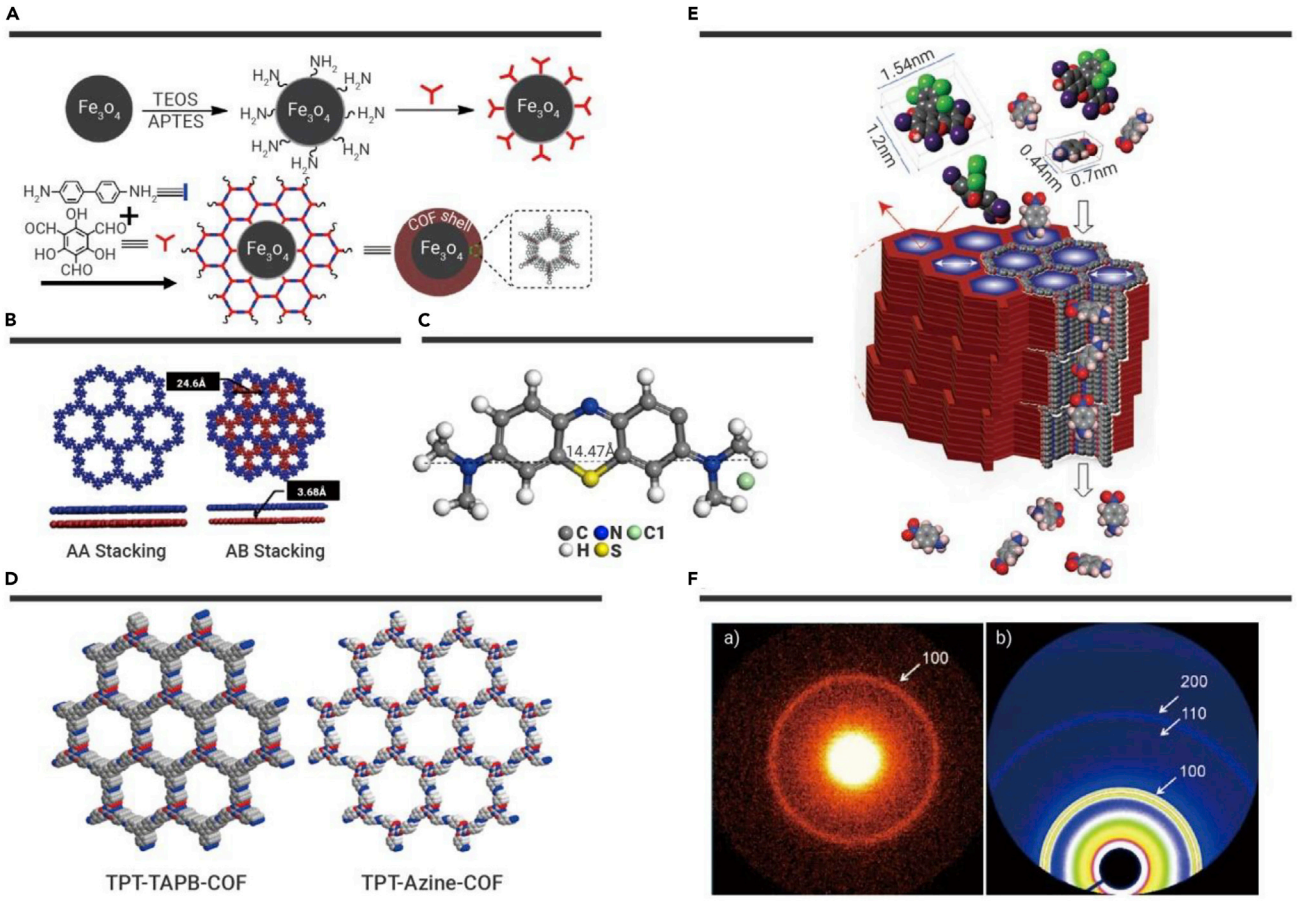

Figure 6. Characterization of COF-based Materials (A) Illustration of the *in situ* growth strategy for the fabrication of core-shell Fe_3O_4@TpBD nanospheres.[90] (B) Experimental PXRD pattern for TpND and calculated PXRD patterns for AA stacking and AB stacking.[91] (C) Modeling illustration of an MB molecule.[96] (D) Top views of TPT-TAPB-COF and TPT-Azine-COF[99]. (E) Schematic of the molecular sieving mechanism of the dye through TpBD.[101] (F) 2D SAXS and synchrotron SAXS profiles of PC-COF.[103]

group[91] investigated BPA adsorption by MSPE technology via macroscopic experiments, spectroscopic analyses, and theoretical calculation. The high tolerance of ionic-strength variation indicates that the removal of BPA is controlled by inner-surface complexation. PXRD has demonstrated that the arrangement of TpND belongs to staggered AB stacking rather than the eclipsed AA pattern and the crystal structure is due to a hexagonal space group with lattice parameters (Figure 6B). BPA can be adsorbed onto a TpND shell due to the existence of hydrogen bonds with phenolic aldehyde groups. Besides, TpND could provide sufficient binding sites and trap BPA molecules.

For the practical utilization of COF material, Liu et al.[92] shaped azine-linked COF powder into a hierarchically porous monolith via ring-opening polymerization. The surface functional hydrazine and aldehyde groups, crystallinity, and micropore of COF powder have remained well after integration into the monolith. Flow tests of BPA elimination by serial monoliths have illustrated that the BPA removal efficiency of M28 reached ~97%, with the cumulative pollutant volume achieved at 18 mL, and the monoliths are well regenerated with flowing methanol. The high capacities and rapid regeneration rates of COF monoliths are attributed to the π-π and hydrogen bond interactions.

Removal of Organic Dyes

More than 100,000 organic dyes have been utilized by the textile, printing, leather tanning, and plastic industries.[93] Most of the industrial waste effluent is discharged into the hydrosphere without proper management. The organic molecules and their complex characteristics and structural diversities potentially threaten the natural environment and human health due to their esthetic consequences, xenobiotic properties, toxicological properties, and other health-risk factors.[94] Based on the charge of the chromophore groups, various organic dyes can be classified into anionic, cationic, and nonionic dyes. In the following sections, we primarily summarize four typical organic dyes (MB, RhB, CR, and MO) and their sorption by COF-based materials.

Elimination of MB. MB is one of the most common cationic organic dyes applied in paper making and cellular staining. Although MB is not considered the most toxic and pathogenic organic pollutant, negative symptoms, such as increase in heart rate, vomiting, and obnubilation, are observed in humans after intake of low concentrations.[95] To uptake MB from water solutions, TPT-DMBD-COF has been utilized.[96] The well-fitted intraparticle diffusion model revealed a two-stage adsorption reaction: film diffusion and intraparticle diffusion. Moreover, electrostatic attraction, π-π stacking of aromatic rings, and differences in pore size between MB (Figure 6C) and COF have been confirmed to be the uptake mechanism. Zhu et al.[97] compared the adsorption processes of MB on task-specific TS-COF-1 and TS-COF-2. Based on the nonlocal DFT and pore size distribution, the pore size of TS-COF-1 was concentrated at 31 Å, which was sufficient to accommodate the transport of MB molecule (dimensions of 13.4 × 5.0 × 4.2 Å). According to Monte Carlo simulations, the saturation capacities of MB on TS-COF-1 and TS-COF-2 were computed to be ~1,200 and ~445 $mg \cdot g^{-1}$, which were consistent with the isothermal experimental data (~1,691 and 377 $mg \cdot g^{-1}$). Macroscopic experiments and *in silico* simulations indicated that the spatial effect of MB molecules and the essential pore size of COFs should be considered simultaneously in further elimination of organic dyes by COF-based materials.

Elimination of RhB. RhB, a typical fluorochrome, is widely utilized in food additives, cosmetics, and fluorescence probes. However, the carcinogenicity of RhB was reported by IARC, which revealed its potential threats.[98] Two types of COFs (TPT-azine-COF and TPT-TAPB-COF, Figure 6D) with a

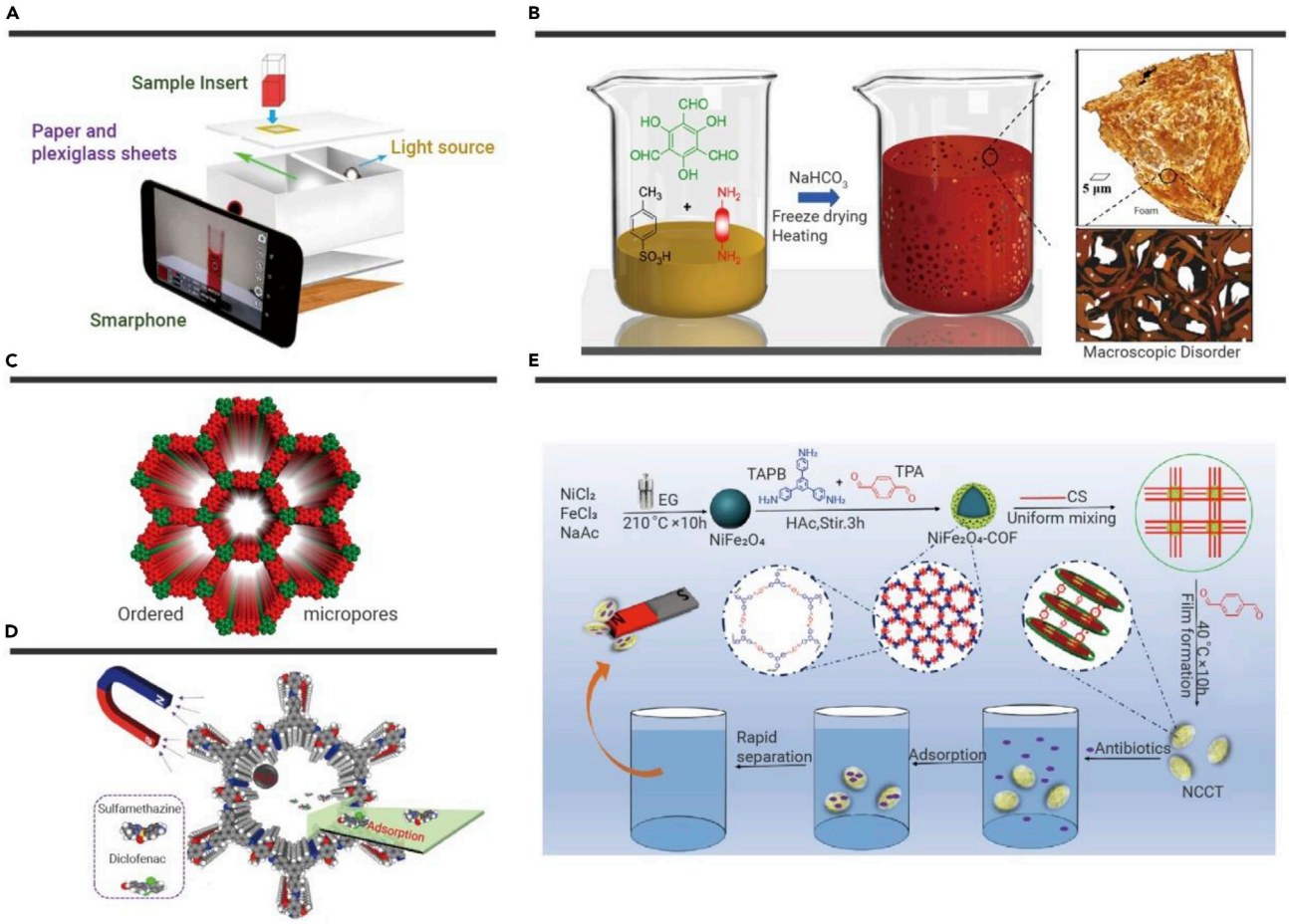

Figure 7. COF Foam Simulation and Application (A) The smartphone colorimeter system for DFS-4BS concentration estimation.[104] (B) Schematic illustration of COF foam synthetization and 3D volume rendered X-ray-computed images of the foam matrix and disordered macropores.[181] (C) Space-filled model of ordered micropores of 2D crystal TpPa.[188] (D) Graphical illustration of diclofenac and sulfamethazine elimination process by the MSPE strategy.[169] (E) The fabricated exhibition and antibiotic removal reaction of NCCT.[108]

heteroatom-rich linker TPT-CHO were applied for RhB removal.[99] The high RhB removal (725 $mg \cdot g^{-1}$ for TPT-azine-COF and 970 $mg \cdot g^{-1}$ for TPT-TAPB-COF) were in accordance with the BET surface areas (957 $m^2 \cdot g^{-1}$ for TPT-TAPB-COF and 1,020 $m^2 \cdot g^{-1}$ for TPT-azine-COF). Higher removal capacities of RhB demonstrated the excellent selectivity and regeneration capability of TPT-azine-COF and TPT-TAPB-COF.

CuP-DMNDA-COF, a novel imine-linked porphyrin COF, was synthesized with the construction of CuTAPP and DMNDA.[186] CuP-DMNDA-COF was modified with $FeCl_3$ in acetone to form CuP-DMNDA-COF/Fe. The enhanced adsorption performance of RhB on CuP-DMNDA-COF/Fe revealed that the removal process was affected by the coordinate interactions between Fe(III) ions in the COF and the carboxy group of RhB. Thermodynamics and the van't Hoff equation were used to investigate the adsorption process, and the results (positive ΔH and ΔS, negative ΔG) illustrated a spontaneous and endothermic process.

Elimination of CR. CR, a typical anionic dye, is extensively used in the paper making industry and as an acid-base indicator and biological dye.[100] The complicated chemical structure, high solubility, and carcinogenicity of CR demonstrate its high priority to be eliminated from the hydrosphere. To date, serial COF-based materials have been utilized for CR removal. A novel COF-COOH was synthesized through polymerization of Tp and DBA.[176] Afterward, modified ions (Ca^{2+}/Ni^{2+}) were further introduced to form COF-COOCa and COF-COONi. In the FTIR spectra, the new peaks at 1,574 and 1,224 cm^{-1} corresponding to C=C and C-N bonds demonstrate the formation of a keto structure in COF-COOH. The numerous hydrogen bonding sites and π-conjugated structure of COF-COOH contributed to good capture efficiency for CR. The adsorption capacities of CR on COF-COOCa and COF-COONi were calculated to be 704.2 and 781.3 $mg \cdot g^{-1}$ respectively, which were attributed to the enhanced electrostatic interaction of metal ion sites with CR.

A porous and crystalline COF membrane was fabricated by the methodology of baking organic linkers in the presence of PTSA and water.[101] A filter adsorption study for the decontamination of CR (MW = 696.6, dimension ≈0.75 × 1.9 nm) was conducted in comparison with Rose Bengal (MW = 1,017.6, ≈1.2 × 1.54 nm), MB (MW = 319.8, ≈0.75 × 1.52 nm), and nitroaniline (MW = 138, ≈0.44 × 0.7 nm). Compared with other pollutants, the lower rejection rate (80%) for CR removal was correlated to its bigger pore size than that of COM. The sieving mechanism (Figure 6E) shows that the difference between the pollutant dimension and COF pore sizes is the crucial mechanism besides hydrogen bonding and π-π interactions.

Elimination of MO. MO has been typically utilized as an indicator for acid-base titration, biological coloring, and textile printing. The acute toxicity and mutagenicity of MO have been previously confirmed.[102] Yu et al.[103] synthesized a polycationic 2D COF (PC-COF) using TAPB and $BFBP^{2+} \cdot 2Cl^-$ and applied it for the removal of MO. In the 2D SAXS profile and synchrotron profile (Figure 6F), the sharp scattering peak matching with the 100 facet and the synchrotron profile assigning to the 100, 110, and 200 facets indicated interlayer stacking in PC-COF despite the electrostatic repulsion between BIPY substances. Adsorption experiments showed a positive performance (85.1%) under strong solvation of dye molecules in aqueous solution. The main driving force was the electrostatic attraction between bipyridinium moieties of PC-COF and the anionic moieties of MO.

Elimination of Other Dyes. The decontamination of triphenylmethane dyes (CV and BG) by carboxyl COF-TzDBd was studied by Yan's group.[177] Although the adsorption processes of CV and BG onto COF-TzDBd displayed good resistance under an NaCl concentration of 0.2 $mol \cdot L^{-1}$, the adsorptive capacities sharply reduced when the concentration was above 0.2 $mol \cdot L^{-1}$, indicating that the electrostatic interaction was one of the removal mechanisms for triphenylmethane dye uptake. The synergistic effects of the π-π interaction from the conjugated aromatic structure of COF-TzDBd were further proved by an obvious red shift of characteristic peaks based on UV-vis spectroscopic analyses. In addition, the molecular sizes of cationic CV and BG were favorable for the capture by TzDBd with a pore size of ~40 Å and anionic surface.

To date, direct fast scarlet 4BS was applied widely as the advanced substitute of Congo red. Afshari and Dinari[104] reported an N-enriched T-COF for efficient adsorption of DFS-4BS from textile water. The N-enriched T-COF could adsorb DFS-4BS molecules for approximately 8.5 times of its own weight within 100 min. Interestingly, a smartphone colorimeter system was constructed with accessible equipment for accuracy comparison during the sorption of DFS-4BS. As shown in Figure 7A, the phone colorimeter system was structured with an LED lamp, quartz cell, and smartphone with Color Grab software 3.6.1. In this work, the dynamic range of the colorimetry system was limited to 70 $mg \cdot L^{-1}$, and an excellent concordance between spectrometer and phone colorimeter results was achieved in the removal of dye from real textile wastewater. The results further demonstrated that the proposed smartphone colorimeter system is a potential replacement for spectrometry.

Recently, Karak et al.[188] reported an *in situ* gas-phase foaming technique to induce disordered foam in ordered COF micropores. A schematic illustration of COF foams is depicted in Figures 7B and 7C. Various amines were reacted with PTSA, and then the generation of CO_2 contributed to the formation of COF foams. Among the serial COF foams synthesized with different amines, TpPa-2 foam manifested excellent removal capacities and high rates (within 10 s) for the elimination of various organic dyes from water solutions. All elimination efficiencies for Acid Fuchsin, Rose Bengal, iodine, MB, and RhB were over ~96%, and the pseudo-second-order rate constants were 1.4, 30.3, 4.3, 11.8, and 7.4 $g \cdot mg^{-1} \cdot min^{-1}$ correspondingly. The diffusion through macropores and remaining adsorption inside micropores and mesopores were regarded as the main interaction mechanisms.

Overall, the molecular size of organic pollutants and predesigned pore diameter are extremely important in adsorptive applications of the COFs. In addition, the introduction of additives could enhance the electrostatic interaction between COFs and pollutants, which could significantly improve the removal performance of COF-based materials.

Removal of Pharmaceuticals

Over the decades, the rapid development of pharmaceutical industries and increasing consumption of pharmaceuticals for personal health unavoidably lead to the improper discharge of PPCPs into the aqueous environment.[105] The toxicity, oncogenicity, teratogenicity, and mutagenicity of pharmaceuticals, such as ibuprofen, diclofenac, sulfamethazine, and ampicillin, severely threaten the ecosystem and humans.[106] The crucial mechanisms for pharmaceutical decontamination have been reported to be electrostatic attraction, H bonding, π-π interaction, and surface complexation between pollutants and COFs.

Sulfamerazine, a typical sulfonamide used as a bacteriostat and as an antiinfective, is commonly utilized in clinical practice. However, its potential threats to the ecological system have aroused extensive concern. Zhuang et al.[170] fabricated TPB-DMTP-COF for efficient elimination of sulfamerazine from aqueous solutions. Its highly crystalline structure, significant specific surface area (2,115 $m^2 \cdot g^{-1}$), and large channel (~3.3 nm) are favorable for considerable capacity (209 $mg \cdot g^{-1}$), fast reaction equilibrium (in 80 min), and good cyclability for sulfamerazine adsorption. Distinct pH-dependent sorption, zeta potential charge, and dissociation constants indicate electrostatic interaction as a vital mechanism for sulfamerazine elimination. Moreover, DFT calculations demonstrate that pollutant molecules could be adsorbed on the pore sites of COFs predominantly through the C-H···π interaction.

Ibuprofen, which is commonly selected as a lipophilic pharmaceutical contaminant, is frequently detected in effluent. Mellah et al.[107] synthesized TpBD-$(CF_3)_2$ and applied it for ibuprofen removal. Equilibrium was reached within 60 min. High removal amounts at neutral conditions (~119 $mg \cdot g^{-1}$) and pH 2 (~150 $mg \cdot g^{-1}$) revealed the strong resistance of COFs under harsh circumstances. In contrast, a significant decrease in removal rate under alkaline conditions illustrated repulsions against the ionic carboxylic acid moiety on the COF surface. The adsorption comparison among ibuprofen, acetaminophen, and ampicillin indicates the potential selectivity of TpBD-$(CF_3)_2$ in the decontamination of lipophilic pharmaceutical contaminants.

TPB and DMTA were utilized as monomers to fabricate the precursor TPB-DMTP-COF and then an Fe element was introduced to form a magnetic COF. MSPE technology was used to uptake pharmaceutical contaminants from water solutions, such as diclofenac (109 $mg \cdot g^{-1}$) and sulfamethazine (113.2 $mg \cdot g^{-1}$).[169] The specific surface area and pore size of magnetic COF were computed to be 2,245 $m^2 \cdot g^{-1}$ and 2.5 nm, respectively. DFT calculation was conducted to probe the removal mechanism, and the results illustrated that the adsorption of pharmaceutical contaminants was dominated by the π-π interaction and the C-H···π interaction, while H bonding was not observed. A graphical illustration of the removal process using the MSPE route is depicted in Figure 7D.

Although pharmaceutical antibiotics are widely used, they are identified as persistent contaminants due to their potential toxicity and due to the presence of bacteria resistant to them. Tetracycline and cefotaxime are frequently detected from aquatic environments and are difficult to eliminate. Li et al.[108] reported a novel COF-based material named as "NCCT" to eliminate pharmaceutical antibiotics using the MSPE method. A brief fabricated illustration and removal reaction of NCCT are depicted in Figure 7E. The synergic research in the distribution of TC and pH-dependent results in chemicals has demonstrated that the driving force of adsorption is controlled by electrostatic attraction and surface complexation. According to FTIR analyses, cation exchange between the protonated amino groups and π electrons on NCCT is involved in the adsorption process of TC. Further spectroscopic studies have confirmed the existence of the condensation reaction, electrostatic effect, H bonding, and π-π interaction. The high removal capacities of TC (388.52 $mg \cdot g^{-1}$) and CTX (309.26 $mg \cdot g^{-1}$) have further implied the potential application of NCCT on the management of antibiotic contaminants in wastewater.

Removal of Aromatic Compounds

Compounds with benzene ring structure (mostly) and aromaticity are classified as aromatic compounds, which are confirmed to be stable, toxic, and nonbiodegradable. Typical aromatic compounds include phenolates, chloroarenes, nitrobenzenes, aromatic ethers, terephthalate esters, and related compounds.[109]

Solid-phase microextraction technology has been used to remove phenols. Adsorption of six nitroaromatic compounds (NACs) (2-nitrophenol, 3-nitrophenol, 4-nitrophenol, 2,4-dinitrotoluene, 1-fluoro-2-nitrobenzene, and 2,4-difluoronitrobenzene) on porous COF[110] has shown fast dynamic performances (all NACs achieved equilibrium within 60 min) and experimental elimination amounts of NACs (239.88, 159.43, 158.25, 137.99, 98.50, and 78.63 $mg \cdot g^{-1}$). For application simulation, the recoveries of six NACs were in the range of 84.0%–112.3% in lake water, wastewater, and tap water samples. The extraction mechanism of NACs has indicated the size selectivity of COF for single-benzene ring compounds instead of multiple-benzene ring compounds, and that NACs with ortho groups possess better interaction with COF. Overall, the π-π stacking effect, hydrogen bonding, size difference, and functional group preference between COF and NACs are dominant forces. Wang et al.[111] reported a solid-phase microextraction approach to remove seven phenols (phenol, 4-chlorophenol, 4-bromophenol, 2,4-dichlorophenol, 2,3-dichlorophenol, 3,4-dichlorophenol, and 2,3,6-trichlorophenol) from wolfberry, *Robinia*, and *Codonopsis* honey samples. Selectivity experiments among phenols, PAHs, and n-alkanes have indicated that π-π stacking

interactions, π conjugation of aromatic groups, and hydrophobic interaction have dominated the capture reactions between SNW-1-coated fiber and contaminants.

Triphenyl phosphate, a typical aryl-organophosphorus flame retardant, is widely applied in ignition prevention for electronics equipment, plastics, and woods. Wang et al.[112] synthesized COF-1, COF-2, and COF-3 with increasing pore size by Schiff-base reactions and enol-to-keto tautomerization between TFP and linkers PDA, BD, and DT, respectively. All COFs have exhibited high stabilities under 350°C and harsh acid conditions (8 M HCl for 6 days). The maximum removal capacities of TPhP on COFs have been computed to be 86.1, 387.2, and 371.2 $mg \cdot g^{-1}$, revealing that the proper pore size of COFs is favorable for adsorption reactions.

Catechol (pyrocatechol or 1,2-dihydroxybenzene) is utilized as a fungicide, a pesticide, a perfume, and an electroplating additive. The group of Yan[113] reported a phenylboronic acid-functionalized COF (DhaTab-PBA) for efficient elimination of catechol. S 2p XPS spectra of DhaTab-PBA and organosulfur compounds have been observed due to the introduction of 4-mercaptophenylboronic acid. A negative enthalpy change has demonstrated excellent adsorption properties of DhaTab-PBA (160.0 $mg \cdot g^{-1}$). After five cycles of adsorption-desorption reactions, an inconspicuous decrease of adsorption capacities has revealed the good reusability of DhaTab-PBA. The selective study has indicated that the synergistic effect between the π-π interaction and phenylboronic acid moiety leads to a highly efficiency removal of catechol by DhaTab-PBA.

Elimination of Other Organic Pollutants

PFAS, such as PFOA and GenX, are utilized in fluoropolymer industries, as stain repellents, and as aqueous film-forming foams. Dichtel's group[114] reported a hexagonal imine-linked 2D COF loaded with serial concentrations of amine functional groups (X%[NH_2]-COFs) and azides (X%[N_3]-COFs), which has exhibited high affinity toward anionic PFAS. Nonlocal DFT analyses have represented narrow pore size distributions (~2.6 nm), and that the pore sizes have increased along with the reduction of azide and amine (X) concentrations. The results demonstrated the formation of 2D imine-linked COFs with amine loadings (1%–100% terephthaldehyde monomers). Compared with X%[N_3]-COF, higher GenX binding capacities have been obtained by X%[NH_2]-COF (240 $mg \cdot g^{-1}$ for 20%[NH_2]-COF). The amines in COF have produced beneficial microenvironments for GenX adsorption and a maximum of two GenX molecules could be bound under a sparsely distributed network.

Marine phycotoxin okadaic acid, the most extensive cause of diarrheic shellfish poisoning, could attribute to harmful algal blooms, which has caused great economic losses to seafood aquaculture. However, only a ow concentration of the toxin could be detected during an okadaic acid (OA) outbreak because most toxins are reserved in producer microalgae. Salonen et al.[115] utilized TpBD-Me_2-COF to eliminate OA from synthetic seawater under 19°C, and the reaction achieved equilibrium in 1 h, with a maximum adsorption capacity of 279 $mg \cdot g^{-1}$, which is much higher than that of previous studies. In addition, OA could be desorbed from TpBD-Me_2-COF efficiently and reused for three cycles, revealing the potential for *in situ* concentration of OA with the use of TpBD-Me_2-COF.

Overall, various organic matters are classified into EDCs, aromatic chemicals, dyes, and pharmaceutical pollutants. The adsorption performances by COF-based materials are exhaustively summarized and tabulated in Table 1. The abundant active sites, surface functional groups, high BET surface areas, opposite charges, and appropriate pore size distributions of COFs and modified materials contributed to the high capacities and efficiencies of contaminant elimination. Moreover, the sorption processes are mostly dominated by electrostatic attraction, π-π interaction, and hydrogen bond interaction, and some of the mechanisms are ascribed to surface complexation, molecular sieving, and functional group selectivity.

MECHANISM ANALYSIS OF REMOVAL OF POLLUTANTS BY COF-BASED MATERIALS

Investigating the mechanism of action of pollutants is predominant in the explanation of the removal process, which is vitally important to determine the reaction conditions of adsorption, desorption, and regeneration. Interaction mechanisms are mostly performed with the use of comprehensive experimental observations, spectroscopic analyses, and theoretical calculations. Adsorption performances are highly affected not only by multiple weak intermolecular interactions (e.g., hydrophobicity, hydrophilicity, electrostatic interactions, hydrogen bonding, and van der Waals [vdW] interactions) but also by intrinsic characteristics (e.g., surface charge, pore size, shape, electronic states, crystallinity, surface-to-mass ratio, decorated functional groups, and surface wrapping in the biological medium) of various adsorbents.[237] Therefore, multiple mechanisms may simultaneously control pollutant adsorption, and the exact removal mechanism could be understood via macroscopic experiments and microscopic analysis.

Macroscopic Experiments

Typically, the adsorption mechanism may be ascribed to diverse types of interactions, which could be determined based on the reaction conditions. Therefore, investigating environmental conditions, such as pH, reaction time, and temperature, is useful to understand the removal mechanism. Typical kinetic and thermodynamic models are summarized in Table S1.

Background pH Value. Generally, the states of adsorbents, species of adsorbates, and their interaction are greatly influenced by solution pH values.[96,170] The effects of solution pH on the adsorption process are mainly as follows (1) influencing the species distribution of pollutants, (2) altering the functional groups by protonation/deprotonation, and (3) changing the surface charge of adsorbents.[76,87] For example, the adsorption process of U(VI) is strongly dependent on pH because of the different U(V) species at different pH conditions.[76] UO_2^{2+} is the main species at pH < 3; polymerized hydrolysis ions, such as $UO_2(OH)^+$, $(UO_2)_2(OH)_2^{2+}$, and $(UO_2)_3(OH)^{5+}$, become the dominant species at pH > 3; and U(VI) directly becomes a precipitate (schoepite) at pH > 8.[80] In terms of Hg(II), Hg^{2+} exists at pH < 3, while Hg^{2+}, $Hg(OH)^+$, and $Hg(OH)_2$ are dominant states at pH 3–6. Insoluble $Hg(OH)_2$ can be formed at pH > 6.[58] Most BPA would not dissociate and exist in molecular form at pH < 9. However, BPA are deprotonated into anionic BPA ($HBPA^-$ and BPA^{2-}) at pH ≥ 9.[62]

The surface charge of adsorbents is also dependent upon solution pH, which dramatically influences the adsorption ability of COF-based materials. At values less than pH_{zpc}, the adsorbent surface is protonated, and increasing the positive charge will lead to a higher electrostatic interaction between adsorbent and anionic adsorbate. On the contrary, the surface charge of adsorbent turns to negative at pH > pH_{zpc}, and leads to electrostatic repulsion between adsorbent and anionic pollutants.[104] Taking TpPa-1 as an example, the amino groups of TpPa-1 and Fe3O4@TpPa-1 can be protonated to positive (-NH3$^+$) at pH 1.0, which have a strong attraction to negatively charged chromium species ($HCrO_4^-$ and $Cr_2O_4^{2-}$). Therefore, chromium anions could be easily removed from aqueous solution via electrostatic attraction.[62] The removal of Cd(II) on N-enriched COF is negligible in mildly acidic conditions because the active sites of adsorbency are occupied through protonation by the nitrogen groups. By increasing the solution pH, an anionic form of COF is formed, so active centers of adsorbent are accessible for Cd(II) removal.[60] Above all, the electrostatic interaction plays a vital role in the adsorption process.

Thermodynamic Analyses. Based on Brownian movement theory, the adsorption process of pollutants toward COF-based materials can be directly influenced by the temperature.[58,238] Several isotherm models, such as the Langmuir, Freundlich, Dubinin-Radushkevich (D-R), and Temkin models, have been applied to reveal the interaction. The Langmuir and Freundlich models are extensively utilized for adsorption simulation. The applicability of isotherms is compared by recognizing the correlation coefficients and error analysis.[60,71] The suitable model can accurately depict these adsorption processes and evaluate the bonding properties of COF-based materials.[110] Assuming that there is no interaction between adsorbates, and that all the sorption sites on the solid surface are the same and distributed uniformly, then a uniform monolayer adsorption can be confirmed by the Langmuir model. Supposing that the adsorbate arrives at the nonuniform surface of adsorbents from the liquid phase and that the adsorbent has different

adsorption sites on the surface, thus leading to different adsorption energies and unevenly distributed surface adsorption heat, then the uneven multilayer adsorption is in accordance with the Freundlich model.[76,80] In brief, the Langmuir equation assumes homogeneous surface monolayer coverage, and the Freundlich model is an empirical multilayer adsorption model.[169,178] The D-R isotherm has been studied to determine the nature of the adsorption (physical or chemical), which is related to the sorption mean free energy (E, kJ/mol).[87] The dimensionless parameter R_L is derived from the equation of K_L, and the value demonstrates the acceptable adsorption for $0 > R_L > 1$, unfavorable for $R_L > 1$, linear for $R_L = 1.0$, and irreversible for $R_L = 0$.[87] The 1/n value of the Freundlich constant refers to the favorability of the adsorption process. An $n > 1$ implies a favorable adsorption process, while $n = 1$ displays an irreversible adsorption.[239] For E_D (kJ/mol) (D-R isotherm), $E_D < 8$ (kJ/mol) suggests physical adsorption, while $E_D = 8–20$ (kJ/mol) demonstrates chemical adsorption. Also, b_T (the Temkin constant) is related to the heat of adsorption, and $b_T < 20$ kJ/mol suggests a good consistency of superior physical adsorption.[60]

The Langmuir model has proved to be more suitable than the Freundlich model for describing the adsorption process of U(VI) on COF-TpPa-1,[76] Hg(II) on TPB-DMTP-COF-SH,[184] and six types of NACs on novel porous COFs.[110] The adsorption of these pollutants toward COF adsorbents is dependent on the completion of the chemisorption monolayer and likely homogeneously dispersed on the porous scaffold. From the Langmuir equation, the maximum adsorption capacities of COF-TpPa-1 and TPB-DMTP-COF-SH are calculated to be 168.1 $mg \cdot g^{-1}$ for U(VI),[76] and 4,395 $mg \cdot g^{-1}$ for Hg(II), respectively.[184] The adsorption isotherm of BPA on PA-POF-2 is better fitted with the Freundlich model as compared with the Langmuir model, suggesting that multilayer adsorption, rather than monolayer adsorption, controlled the elimination process. The K_F value (1,276 $mg \cdot L^{-1}$) and 1/n (0.4185) obtained from the Freundlich model indicate the large adsorption capacity of BPA.[178] Sips model, which takes into account more comprehensive conditions, is more advanced than the Langmuir and Freundlich models to describe the adsorption process. The Sips model is a combination of both models and can be simplified into the Langmuir or Freundlich models under specific conditions.[169] Both TCS and TCC have similar adsorption processes on Fe_3O_4@COFs. The Freundlich model is well fitted in the low-concentration region, while the Langmuir model is more appropriate at high concentration levels. This phenomenon might be multilayer adsorption through the interactions of space embedding effect, vdW forces, and benzene ring π-π stacking at low-concentration levels, and monolayer adsorption through strong π-π stacking between TCS or TCC and Fe_3O_4@COFs at high concentration levels.[237] The synthesized N-enriched COF exhibits excellent performance in Cd(II) removal with high capacity (396 $mg \cdot g^{-1}$) by the Langmuir model. More importantly, b_T (<20 $kJ \cdot mol^{-1}$) is in good agreement with superior physical adsorption. Moreover, E_d has been measured experimentally to be 1.4145 $kJ \cdot mol^{-1}$, indicating that the major mechanism is physical adsorption.[60] Therefore, using isotherm models can confirm the good adsorption capacity of COF-based materials, and that the adsorption process can be put forward based on the experimental data.

To evaluate the adsorption thermodynamics, Gibbs free energy (ΔG^0, kJ/mol), changes in standard values of enthalpy (ΔH^0, kJ/mol) and entropy (ΔS^0, kJ/(mol·K)) are generally calculated from temperature-dependent adsorption isotherms.[62,240] For example, the removal of U(VI) by COF-TpPa-1 has shown that the adsorption process is endothermic, shows an increase in freedom, and is spontaneous with positive ΔH^0 (48.605 kJ/mol), positive ΔS^0 (221.77 J/(mol·k)), and negative ΔG^0 (−17.515, −19.733, and −21.950 kJ/mol at 298.15, 308.15, and 318.15 K, respectively). Besides, ΔG^0 decreases with increasing temperature, indicating an increased reaction at high temperature.[76] As for Cr(VI)/BPA adsorption on TpPa-1, the thermodynamic study has confirmed its spontaneous, endothermic, and chemisorption processes. The negative ΔG^0 value demonstrates the thermodynamic feasibility as well as a spontaneous adsorption process. Positive ΔH^0 indicates an endothermic process, implying that chemisorption is the principal reaction mechanism. In addition, positive ΔS^0 values not only reflect the affinity between adsorbents and adsorbates, but also improve the level of disorder at the solid-liquid interfaces.[62] The adsorption of BPAF and BPA on Fe_3O_4@TpBD is confirmed to be a thermodynamically spontaneous process with both negative ΔH^0 and ΔS^0.[40] TzDBd also exhibited good affinity for CV and BG. The carboxyl group in TzDBd forms H bonds with water molecules, resulting in a higher state of ordering with a lower entropy value. When adsorption reaction occurs, CV and BG molecules replace water molecules due to electrostatic interaction. As a result, more water molecules are released and the hydration shell is disrupted, leading to an increase of enthalpy.[240]

Above all, investigating the temperature effect on the adsorption process is vital to assess the application scope of COF-based materials. Different surface adsorption models have been used to determine the adsorption types and properties between adsorbents and adsorbates. Adsorption capacities of COF-based materials are also calculated from the models. Adsorption thermodynamics can further confirm the extent and driving force of the adsorption process, and different parameters can reflect the affinity between adsorbents and adsorbates.

Adsorption Kinetics Analyses. Adsorption kinetics are mainly utilized to investigate the diffusion mechanism, adsorption control step, and influencing factors of adsorbed velocity.[87,237] To further investigate the kinetic adsorption process, the pseudo-first-order kinetic model, the pseudo-second-order kinetic model, the intraparticle diffusion model, and the Elovich model are widely used.[80] The correlation coefficient (R^2) is used to check the validity of each model.[60,76]

Generally, the adsorption rate of adsorbate on a porous adsorbent mainly depends on intraparticle diffusion. The intraparticle diffusion model is applied to fit the adsorption kinetic data to clarify the diffusion process.[112] The simulation of TPhP adsorption on COFs of three different pore sizes (COF1<COF2<COF3) by the intraparticle diffusion model implies that intraparticle diffusion is the rate-controlling step for COF1 and COF2, while the model fails to fit TPhP adsorption on COF3. Therefore, TPhP could more easily diffuse into a larger pore size of COFs.[112] For the adsorption of Hg(II) over DAPS50-COF-SH, the rate-controlling step is controlled by chemisorption, intraparticle diffusion, and external diffusion according to the intraparticle diffusion and film diffusion models.[57] The intraparticle diffusion model can also provide relevant information at different stages of the adsorption process.[96] In addition, it is adopted to simulate dynamics data of Cr(VI)/BPA on Fe_3O_4@TpPa-1, and two phases with varying rates of adsorption have been observed. The first phase indicates instantaneous external surface adsorption or boundary layer diffusion, with the second phase corresponding to the slower internal-particle diffusion indicating that Cr(VI)/BPA diffuse into mesoporous of TpPa-1, which serves as a rate-determining step. Beyond that, the second-phase simulation curve did not pass through the origin, suggesting a chemical complex reaction or a chemical oxidation-reduction process.[62]

The pseudo-first-order model that describes that the adsorption of the adsorbate from the solution to the solid surface is controlled by the diffusion step, which is based on the assumption that the adsorption rate is controlled by a chemical process (electrostatic interaction, sharing of electrons, and ion exchange) or strong surface complexation.[87,96] The pseudo-second-order model simulation of U(VI)/Eu(III) on TpPa-1 demonstrates that chemisorption or strong surface complexation govern adsorption processes.[87] The pseudo-second-order model simulation suggests the rate-limiting factor of NAC adsorption to COFs.[110] The pseudo-second-order kinetic model is more satisfactory in illustrating the adsorption of CV and BG on TzDBd, which also confirms the electrostatic interactions between the cationic dye molecules and the anionic carboxyl group of TzDBd.[240] The adsorption of TCS and TCC onto Fe_3O_4@COFs is both better fitted by the pseudo-second-order model, and the process could be divided into two steps: a diffusion process via vdW forces dominates the first step in the initial 10 min, while the second step is dominated by special intermolecular π-π stacking interactions between benzene rings of pollutants and Fe_3O_4@COFs and the space-embedding effect of TCS and TCC on the Fe_3O_4@COFs mesoporous surface over 10 min.[237]

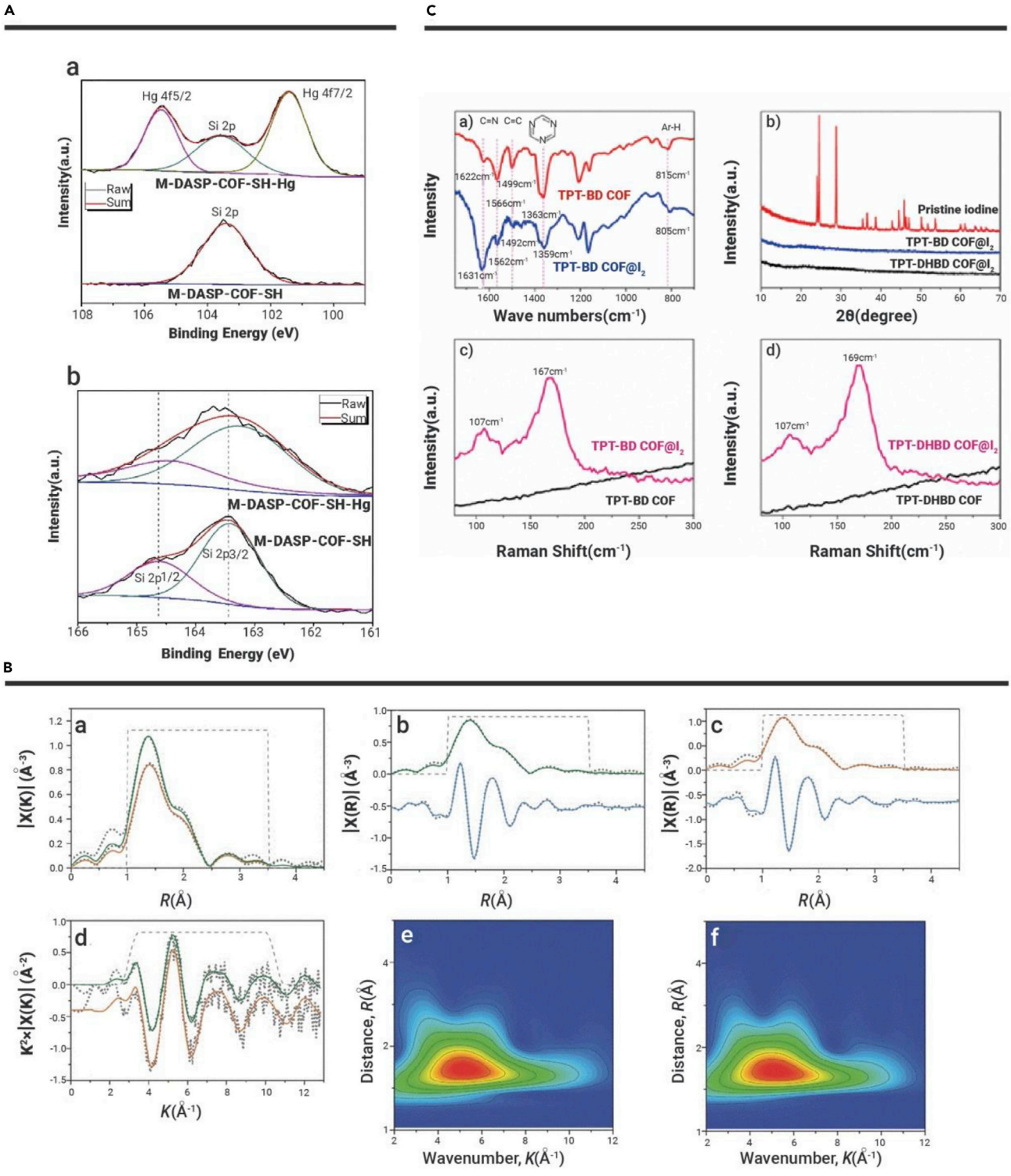

Figure 8. Advanced Spectroscopy Analysis of Interaction Mechanism (A) XPS spectra of Hg 4f (a) and S 2p (b) of M-DAPS50-COF-SH and Hg-loading samples.[57] (B) (a) Fourier transform of U L_{III}-edge EXAFS spectra of POP-TpDb-AO (green line) and COF-TpDb-AO (orange line) in R-space, (b) Fourier transform of U L_{III}-edge EXAFS spectrum of COF-TpDb-AO in R-space. The magnitude of Fourier transform is fitted by a green line; the real component is fitted with a blue line. (c) Fourier transform of U L_{III}-edge EXAFS spectrum of POP-TpDb-AO in R-space. The magnitude of Fourier transform is fitted by an orange line; the real component is fitted with a blue line. (d) Accompanying k^2-weighted $\chi(k)$ data and fit for POP and COF (green and orange lines, respectively). (e) Wavelet transform analysis of COF-TpDb-AO and (f) POP-TpDb-AO, demonstrating the extreme similarity between datasets. In all panels, gray dashes denote the fit window.[181] (C) (a) FTIR spectra of TPT-BD COF and TPT-BD COF@I_2, (b) Raman spectra of TPT-BD COF, and (c) TPT-DHBD COF before and after volatile iodine adsorption. (d) PXRD patterns of the pristine iodine and iodine-loaded COFs.[243]

The Elovich model can reveal the irregularities of adsorption data that might be ignored by other kinetic models.[80] The Elovich model simulation of Pb(II) kinetics adsorption on COF-TP and COF-TE has shown to be the best fitting, suggesting a heterogeneous process of Pb(II) diffusion into the lamellar COF materials. The fitting parameter α from the Elovich model is an initial rate parameter, and COF-TE (454.1 $mg \cdot g^{-1} \cdot h^{-1}$) presents a higher

α value than COF-TP (356.3 $mg \cdot g^{-1} \cdot h^{-1}$), indicating that Pb(II) has a higher diffusion rate toward COF-TE. Weaker and less tight π-π stacking and larger interlayer spacing in COF-TE account for favorable diffusion and adsorption.[179]

Therefore, research on adsorption kinetics is essential to understand the mechanism of the adsorption process. According to different kinetic models, the rate-controlling steps and adsorption diffusion mechanism can be estimated using chemisorption, strong surface complexation, intraparticle diffusion, and film diffusion.

Microscopic Analysis

Besides macroscopic analysis, various characterization technologies not only determine the surface properties of COF-based materials but also help us to understand the reaction pathway and mechanism via analysis of elemental species and surface functional groups before and after reactions.[177,241,242]

XPS Analysis. XPS can provide the surface composition of atoms and determine the valence of elements on the surface of materials.[177,242] For example, in the XPS spectrum of Hg(II)-loaded M-$DAPS_{50}$-COF-SH, the peaks at 101.4 and 105.4 eV are assigned to Hg $4f_{7/2}$ and Hg $4f_{5/2}$, confirming the successful adsorption of Hg(II) via chemical bonding (Figure 8A(a)). Compared with the Hg-loaded sample, the corresponding binding energy of S 2p in M-$DAPS_{50}$-COF-SH shows a slight shift toward a higher energy (~0.4 eV) (Figure 8A(b)), demonstrating the involvement of S functional groups during Hg(II) adsorption.[57] In addition, the 2P XPS spectra of S before and after Hg adsorption showed a movement of 0.3 eV.[184] Therefore, the thiol and triazole functional groups in COF-based materials are confirmed to be the determining factor for the enhancement of Hg(II) adsorption. High-resolution Cr 2p spectrum undoubtedly confirms the successful adsorption of Cr(VI) on TpPa-1. Moreover, the peak of Cr $2p_{3/2}$ is deconvoluted into two components, which suggests the reduction of Cr(VI) to Cr(III). According to the inconspicuous fluctuation of molar percentage of Cr(III) after the introduction of Fe_3O_4, the reduction of Cr(VI) is mainly caused by electron donor groups of TpPa-1, with the aid of π electrons.[62] The spectra of U 4f and Eu 3d confirm that U(VI) and Eu(III) are successfully adsorbed onto TpPa-1.[87] Above all, applying XPS spectroscopy can identify the different species of the metals before and after adsorption. It can concluded that the removal of metal ions is not only by adsorption on the typical structures of the COFs but also by reduction with the functional group of the COF materials.

FTIR Analysis. The FTIR technique involves profound investigation into the molecular structures and surface functional groups of adsorbents, which gives direct evidence of the bonding information in adsorption.[80]

FTIR characterization has been used to track the interaction between COF-PDAN-AO and U(VI) species. A new vibration peak at 920 cm^{-1} belonging to O=U=O confirms the successful adsorption of U(VI) on COF-PDAN-AO.[244] Noticeable changes occur on the FTIR spectra of COF-Tz-OH after Pb(II) adsorption. The shifting of the stretching vibration band of the hydroxyl group and the adsorption bands of the triazine unit indicate that the adsorption process involves the interaction between Pb(II) and the surface hydroxyl and triazine moieties of COF-Tz-OH.[224] In the FTIR spectra of DAPS50-COF-SH before and after Hg(II) loading, a new peak at 1,388 cm^{-1}, which is attributed to the S-Hg stretching is clearly observed, suggesting the chemical bond between S and Hg.[57] In the FTIR spectrum of TpBD-$(CF_3)_2$ after ibuprofen adsorption, the presence of the pharmaceutical is evident due to the appearance of C=O stretching of the ibuprofen carboxylic acid moiety at ~1,720 cm^{-1}. The slight blue shift of free ibuprofen indicates the importance of hydrophobic interactions in pharmaceutical adsorption.[107] The corresponding peaks in the FTIR spectra can confirm the presence of a functional group and its variation after adsorption. Therefore, the interaction between pollutants and COF-based materials, such as hydrophobic interactions, and electrostatic interactions, can be clearly explained.

XAFS Analysis. XAFS spectroscopy, including XANES and EXAFS, is useful for determining the binding environment and microstructure of metal ions.[245,246] XANES spectroscopy provides persuasive evidence for the district oxidation-reduction state of metal ions by directly observing the energy shift of the absorption edge.[247] EXAFS spectroscopy has been considered as a useful analytical technique for measuring the microstructures from the coordination numbers (N), bond distance (R), and Debye Waller factor (s_2).[143,247]

Despite its widespread use in the fields of geochemistry and material science, XAFS has a limited application in COF research to characterize the adsorption on COF materials.[242] To gain more insight into the coordination environment of mercury in the three thiol- or thioether-functionalized COF materials, Sun et al.[182] collected the EXAFS spectra at the Hg L_{III}-absorption edge (12.284 keV). In contrast to previous EXAFS data, no Hg-O contributions were observed. This reveals that each Hg is bound exclusively by two S rather than through -Hg-O-Hg- layering or formation of terminal Hg-OH species, and confirms the adsorption of Hg by the COF materials rather than precipitation as HgO. The U L_{III}-absorption edge (17.166 keV) further shows the coordination environment of U(VI) in both COF-TpDb-AO and POP-TpDb-AO (Figure 8B).[181] Inspection of the data suggests that the U(VI) coordination environment is similar between the two porous frameworks, and that reasonable fits are obtained from applying the same uranyl-benzamidoxime η^2 binding motif model to both COF-TpDb-AO and POP-TpDb-AO (Figure 8B(a, b)). The successful simultaneous fitting of the EXAFS dataset with the same structure model, in conjunction with affording refined parameters within experimental uncertainty of each other, demonstrates a common uranium-binding model. In addition, the wavelet transform is applied for a common U-binding between both POP and COF materials (Figure 8B(c–f)). In contrast to the commonly used Fourier transform, the wavelet transform provides information regarding the localization of different EXAFS signal components in both k- and R-spaces simultaneously. This approach affords superior discrimination of EXAFS contributions from different species, as the phase and backscattering amplitude from different elements are emphasized in different regions of the k-space. The similarity between wavelet transforms for POP and COF indicates identical U-binding environments. However, compared with the randomly populated form in the POPs, the COF-based adsorbents are observed with improved performance, which suggested that the well-oriented chelating groups on the COFs are more ready to bind with U species. The difference is also confirmed by the above IR and XPS results. The computation results also predict that the binding angle of amidoxime groups and uranyl ions affects the overall energy of the resultant complex. Thus, one can conclude that the structural differences in the adsorbent framework are responsible for the divergent performance in adsorption. Applying XAFS spectroscopy can further confirm the ways of bonding and environments between pollutants and COF-based materials, which are essential to understand the interaction.

Combining Multi-technique Analysis. Besides the above-mentioned methods, other techniques, such as XPS, Raman, FTIR, UV-vis, and PXRD can reveal the mechanism on one side, while combining two or more techniques can explain the reaction process in more detail.

The adsorption mechanism of Cu(II) on TpODH has been explored by high-resolution FTIR and XPS analyses. In the FTIR spectrum, the band at 3,373 cm^{-1} weakened and shifted to 3,320 cm^{-1}, and the bands at 1,540 and 1,237 cm^{-1} became broader and shifted to 1,519 and 1,227 cm^{-1}, respectively. The shift of these peaks might reflect the electrostatic and ion exchange interactions between metallic ions and the functional group (-NH) of the material. The reduction in the intensity of FTIR signals demonstrates that coordination interactions between Cu(II) and amide, amino, and carbonyl groups have occurred. In the high-resolution XPS spectrum of TpODH-Cu, the binding energies at 932.5 and 952.2 eV, which correspond to the peaks of Cu $2p_{3/2}$ and Cu $2p_{1/2}$, indicate the interactions between Cu(II) and functional groups (-NH, -C=O). N 1s and O 1s XPS spectra of TpODH and TpODH-Cu further confirm the adsorption via electrostatic interaction and coordination interaction.[238] The mechanism of I_2 enrichment on COFs has been preliminarily studied by combing FTIR spectra, Raman spectra, and PXRD patterns. In FTIR spectra, the characteristic peak position of the materials changes significantly before and after the adsorption. The C=C and C-H bonds of the phenyl ring in TPT-BD COF have shifted from 1,499 and 815 cm^{-1} to 1,492 and 805 cm^{-1}, respectively, and the C=N bonds of the

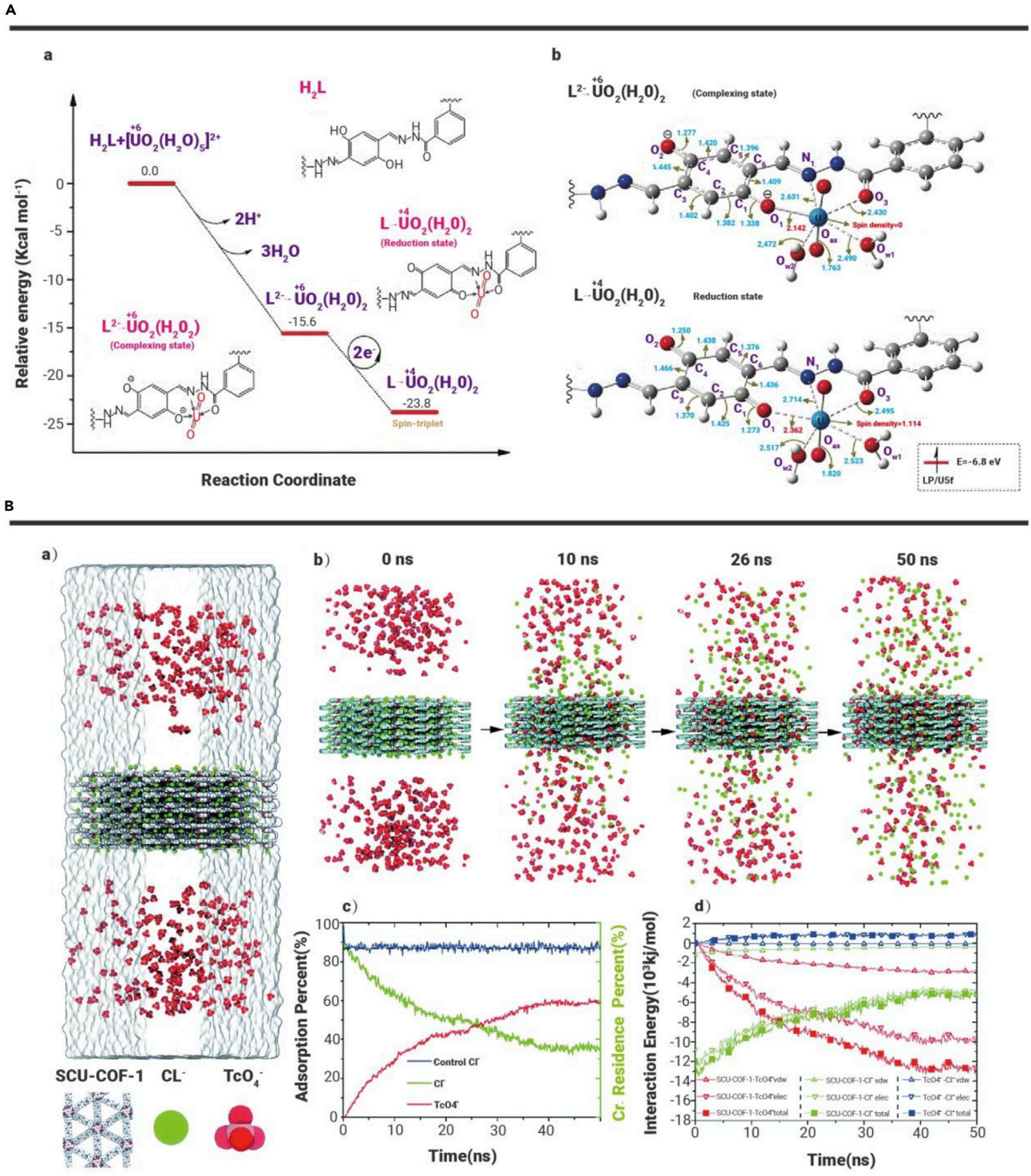

Figure 9. Computational Simulation (A) (a) The species involved in the calculation and the relative free energy profiles (in kcal/mol) for the complexing and redox reaction between RedoxCOF1 and uranyl ions obtained by the DFT calculations. (b) The optimized structures of the stationary points for adsorption structure of the complexing state and the reduction state. Furthermore, the spin density of uranium atom and important bond lengths (Å) are also shown in this figure.[248] (B) MD simulations on the adsorption of $^{99}TcO_4^-$ anions into SCU-COF-1. (a) The initial configuration for MD simulations. (b) A time-series of snapshots to show the adsorbing dynamics of $^{99}TcO_4^-$ anions into SCU-COF-1. The blue framework is the simulation box edge. (c) Time evolution of the adsorption rate of $^{99}TcO_4^-$ anions (red) and the residence rate of Cl^- anions in SCU-COF-1 (green); as well as the residence rate of Cl-anions in SCU-COF-1 in pure water as the control (blue curve). (d) The nonbonded interaction energies (including electrostatic, vdW, and their sum) of SCU-COF-$^{99}TcO_4^-$, SCU-COF-Cl^-, and $^{99}TcO_4^-$-Cl^- as the function of simulation time.[217]

triazine ring at 1,566 and 1,363 cm^{-1} have shifted to 1,562 and 1,359 cm^{-1}, respectively. The imine linkages change markedly from 1,622 to 1,631 cm^{-1}, indicating that iodine adsorption could simultaneously occur at imine linkage, triazine ring, and phenyl ring in the materials (Figure 8C(a)). Raman spectroscopy has been used to detect the species of iodine in TPT-BD COF and TPT-DHBD COF (Figure 8C(b,c)), and the strongest peak at ~167 cm^{-1} is confirmed to be the signature peak of I_5^- (consistent with I_5^- in the V or L configuration). The generation of I_5^- might occur through a charge transfer

interaction between iodine guest molecules and the electron-rich TPT-DHBD$_X$ COFs. In addition, diffraction peaks of TPT-BD COF@I_2 and TPT-DHBD COF@I_2 in PXRD patterns did not show any characteristic peaks belonging to molecular iodine under saturated adsorption, suggesting the transformation of iodine as well (Figure 8C(d)). Based on these results, the high nitrogen content and abundant electron-rich π-conjugated system of TPT-DHBDX COFs lead to its reversible and ultrahigh adsorption capacities for volatile iodine.[243]

EDS can show the presence of significant amounts of captured adsorbates and their homogeneous distribution on COF-based materials.[181] The evident bathochromic change of the characteristic peaks in UV-vis spectra can confirm the interaction during the adsorption process.[240] IR spectroscopy and Raman spectroscopy are vibrational spectra, and can identify the functional groups.[177] Therefore, to trace the interaction between the adsorbents and pollutants, multiple characterization methods can be performed together as a complement with each other.

Theoretical Calculations. Theoretical calculations are also urgently needed to probe the intrinsic adsorption behavior and establish structure property relationships.[143] Such theoretical calculation are useful to elucidate the interaction mechanism, which is extremely difficult to achieved from experimental results.[91] Combining structural information, such as bond length, bond angle, and binding energy, as well as the system charge density, underlying mechanisms can be successfully identified by theoretical calculation.[143] The structural features of robust skeleton, high surface area, open mesopore channel, and density nitrogen sites of Ttba-TPDA-COF with RhB are evaluated by combining experimental results and DFT calculations.[224]

DFT can calculate the behavior of materials based on quantum mechanics.[170] The most important advantage of DFT calculation is the simulation of the interaction processes and probing the species and microstructures at molecular levels under very complicated conditions. For example, DFT is utilized to explore and analyze the selective removal of uranyl ions by Redox-COF1. The species involved in the calculation and their relative free energy profiles are shown in Figure 9A(a). The relative free energy profiles of Redox-COF1 decreased from 0 to −15.6 kcal/mol after the removal of two protons and coordination with UO_2^{2+} to form a complex state. Next, two electrons of the complex state are transferred from oxygen to uranium to form a reduction state, and the process further lowers the relative free energy from −15.6 to −23.8 kcal/mol, indicating the reduction of U(VI) to U(IV) by Redox-COF1. The spin density of U changes from 0 to 1.114, which corresponds to 5f orbital occupancy (the lower right corner of Figure 9A(b)), suggesting that the electrons transfer from the O atom to U 5f orbitals. After electron transfer, bond lengths of C1-C2, C3-C4, C4-C5, and C1-C6 become longer, while those of C2-C3, C5-C6, C1-O1, and C4-O2 become shorter. The results are well consistent with the fact that hydroquinone is oxidized by uranyl ions to form a benzoquinone structure.[248] Wang et al.[40] simulated Hg interaction with Ag NPs@COF-LZU1. Comparing the calculated adsorption energies (using PW91/BS-II) for Hg(II) adsorption to different pure sites of the substrate, the highest adsorption energy is for the top sites of Ag NPs in COF-LZU1. In addition, the adsorption energies for Hg on COF-LZU1 are also very much large (using M06-2X/BS-I). These results suggest that the chemical adsorption between Hg and Ag NPs and physical adsorption with COF-LZU1 play roles simultaneously. The charge distribution analysis indicate the electron density of Hg atoms has increased, while that of Ag NPs has decreased, indicating that electrons are transferred from COF and Ag NPs to Hg atoms during the adsorption process. Therefore, a micro-redox reaction occurred on Ag NP surface (proton donors) during Hg (proton acceptors) adsorption from water. The COF material does not only serve as a supporting matrix but also as an electron donor during Ag Hg nanoalloy formation.[40] In general, π-π interaction and H bonding interaction are found to contribute to organic pollutant adsorption onto COFs. Wei et al.[91] used the DFT calculation to study the adsorption of BPA to TpND and found that BPA is preferentially captured by TpND phenolic aldehyde groups via the hydrogen bonds. Comparing the potential adsorbing sites, including the amine group (N1), the phenolic aldehyde groups (O1 and O2), and the benzene ring, they found that BPA molecules are prone to bind with TpND phenolic aldehyde groups with high adsorption energy. After calculating the density difference of the cluster, the main electron transfer occurs between the oxygen atoms (O1 and O2) in TpND phenolic aldehyde groups and the BPA hydrogen atoms (H1 and H2), suggesting a hydrogen bonding interaction during the adsorption process.[91] The C-H···π interaction also plays an important role in the adsorption process of organic pollutants. Zhuang et al.[169] simulated the partial mechanism of the adsorption between SMT/DCF and magnetic COFs, and found that the π-π interaction is the dominant interlayer interaction for the formation of the layered stacking structure, and that the C-H···π interaction contributes to the adsorption of SMT/DCF onto COFs. Zhuang et al.[170] also proposed that the C-H···π interaction derived from the T-shaped or edge-to-face modes should be responsible for SMT adsorption by COFs according to the DFT calculation, which is also used to clarify the complicated relationship between pore size and sorption capacity. The DFT calculation of TPhP adsorption on three COFs with different pore sizes[112] has proven that TPhP molecules could be easily diffused into COF2 and COF3 with larger pore sizes, while they are prevented from entering the pore structure of COF1 due to its relatively small pore size, resulting in an extremely low sorption capacity of TPhP on COF1. Although TPhP molecules could diffuse into the pore of COF3, the larger pore size could decrease the affinity of the pore structure for TPhP molecules and increase the tendency of TPhP molecules to escape outwards. The affinity is the result of multiple adsorption interactions, including the hydrophobic interaction and the π-π interaction, which occur between the aromatic groups on TPhP and COFs. According to the statistical results of annealing configurations, almost all SMT is trapped in the pore site rather than top site of the COFs. Although SMT molecules could be adsorbed on the top site by π-π interaction, available top adsorption sites are rather limited because of the AA stacking mode. The symmetry of regular hexagon pores and its extending channels account for the optimal symmetric adsorption site distribution on COF pore walls.[170]

Molecular dynamics (MD) simulations are a comprehensive technique to simulate properties of molecular structures and explore dynamic interactions through the calculation of interaction energy and driving forces.[145] He et al.[217] used MD simulations to explore $^{99}TcO_4^-$ adsorption dynamics to SCU-COF-1 and the underlying uptake mechanism (Figure 9B(a)). In the process, many Cl^- anions that originally dwelt in the SCU-COF-1 pores are desorbed from the solid structure. To quantitatively describe the dynamics process, the adsorption kinetics of $^{99}TcO_4^-$ from solution environment (red curve in Figure 9B(c)) and the residence kinetic of original Cl^- in SCU-COF-1 (green curve in Figure 9B(c)), along with the interaction time, were calculated. As shown in Figure 9B(c), after ~26 ns, the amount of $^{99}TcO_4^-$ ions entering SCU-COF-1 exceeds the amount of Cl^- ions that still remain in SCU-COF-1. However, another control simulation in pure water demonstrates that nearly 87.2% of Cl^- ions could be retained in SCU-COF-1 in the absence of $^{99}TcO_4^-$ (blue curve in Figure 9B(c)). The simulation results suggest that the adsorption of $^{99}TcO_4^-$ ions has initiated and furthered the anion exchange. To uncover the driving forces in the anion-exchange processes, time evolution of the nonbonded interaction energies of COF-Cl^-, COF-$^{99}TcO_4^-$, and $^{99}TcO_4^-$-Cl^- were calculated, and they were further deconvoluted into the contributions from the vdW and electrostatic interactions as well (Figure 9B(d)). During the main $^{99}TcO_4^-$ adsorption processes along with desorbing Cl^- ions, the nonbonded interaction energy between SCU-COF-1 and $^{99}TcO_4^-$ ions sharply decreased by ~13,000 kJ/mol, of which the electrostatic part was ~10,000 kJ/mol, about 3.3-fold of the vdW part (~3,000 kJ/mol). The nonbonded interaction energy between Cl^- ions and SCU-COF-1 increased by ~8,000 kJ/mol, with the electrostatic part being ~7,400 kJ/mol and the vdW part ~600 kJ/mol. Meanwhile, the nonbonded interaction energy between $^{99}TcO_4^-$ and Cl^- ions increased by ~850 kJ/mol. The electrostatic part increased by 900 kJ/mol (repulsive), whereas the vdW part decreased by ~50 kJ/mol (attractive). The strong direct nonbonded interaction between SCU-COF-1 and $^{99}TcO_4^-$ ions is intensively derived in this vigorous $^{99}TcO_4^-$ adsorption process. Moreover, the direct electrostatic repulsive interaction between Cl^- and $^{99}TcO_4^-$ further promotes Cl^- desorption. Thereby, the anion-exchange process could be revealed as: the strong binding free energy between SCU-COF-1 and $^{99}TcO_4^-$ led to the successful substitution of Cl^- by

taking over the anion binding sites in SCU-COF-1 as contact time progresses. On the other hand, the occupation of $^{99}TcO_4^-$ significantly weakened the direct interactions between Cl^- and SCU-COF-1 and gradually excluded Cl^-.[217] MD simulations were also carried out to investigate BPA movement from the external solvent to the interior porous structure of TpND. Three BPA of different molecular numbers (Num 5, 10, and 20) were randomly settled in the box under the favorable adsorption conditions. For Num 5, the BPA molecules could easily pass through the surface and then be trapped in the interior of the TpND. For Num 10, a portion of BPA molecules are aggregated into the chain-type cluster and intercalated between the inner layers. With a continuous increase of the number of BPA molecules (Num 20), a mass of them aggregates into a big cluster and embed on the surface of TpND. Therefore, the TpND porous structure also plays significant roles in the adsorption process. The BPA molecules are trapped in the TpND porous structure, and the aggregating effect plays a vital role in the adsorption process at a high concentration of BPA.[91]

Above all, the theoretical calculations can confirm the results from experimental results at molecular level. From the DFT calculation, the adsorption binding sites and the reduction of some radionuclides/heavy metals can be simulated clearly. In addition, DFT can also reveal the complicated relationship between pore size and sorption capacity. MD simulations can further study the movement of adsorbates in solution and uncover the driving force in adsorption. The role of the porous structure in adsorption, ion exchange and electrostatic interactions is also confirmed by MD simulation. Therefore, theoretical calculation can play a primary role in the mechanism study.

CONCLUSIONS AND PERSPECTIVES

The orderly porous structure of the COFs provides a high surface area and abundant porous channels, which are conducive to adsorption and fast diffusion of pollutants. These properties endow the COFs with the potential to be excellent adsorbents. To obtain COF-based materials with superior properties, specific functional groups are introduced into the COFs to enhance their interaction with the target pollutants. COF-based materials containing N, O, and S functional groups have higher adsorption capacity than single COFs due to electrostatic interaction, coordination, and chelation with metal ions.[48,49,51,53,71] In addition, the configuration transformation of functional groups (i.e., the structure would convert from the enol form to the ketone form) can improve the adsorption performance.[50] Combining the functional materials with COFs could enable an elegant combination of physical and chemical properties, synergistic effects, and multiple functions of individual components. Furthermore, the pore structure (e.g., pore size and shape) of COFs can be easily tailored by various methods, offering abundant options for the selective isolation of different pollutants. The hydrophobic skeleton structures of COFs with tailorable pore size also endow COFs with high adsorption performance toward toxic organic molecules via molecular sieving, π-π interaction, and H bonding among others. In addition, the pore-wall engineering of COFs is of great importance with regard to enriching them with more active adsorption sites.

We provide a comprehensive review of recent works on COFs and COF-based materials to remove toxic heavy metal ions, radionuclides, and organic pollutants. We elaborate the analyses of adsorption performance and approaches for mechanism investigations, including adsorption kinetics, adsorption thermodynamics, advanced spectroscopy techniques, and theoretical calculations at the molecular level. The adsorption performance of COFs and their composites with other traditional and advanced nanomaterials are compared. The outstanding adsorption capacities of COFs and COF-based composites mainly resulted from interactions between target ions and functional binding groups on COFs. The low density, permanent porosity, high specific surface area, highly ordered porous structure, and abundant porous channels also work together, which accelerates the diffusion rate of pollutants into the inner structures. Grafting appropriate functional groups onto COFs or blending them with other functional materials to tune their structures and properties have been proven to be efficient strategies for increasing their selectivity and adsorption capacity for targeted contaminants. The great potential of COFs and COF-based materials in environmental remediation has been gradually noted. COF-based catalysts can also be utilized in photocatalysis, redox reaction for pollutant degradation, or metal ion reduction. Various types of COF-based catalysts, including metal-free, heterometal, and hybrid ones, have been fabricated to increase their catalytic activities. However, study on these aspects is still at the initial stage and few studies have been reported.

While some intriguing progress and achievements have been achieved, the study of COFs and COF-based materials in environmental applications is still in its infancy. Several challenges in future development are discussed and some suggestions are proposed as follows: (1) to date, construction of functional COFs with desired performance, such as high adsorption capacity, strong forehead stability, and excellent ductility, still remains a challenging task. Therefore, more efforts should be devoted in the methods of synthesis of COFs and COF-based materials with excellent properties. (2) The disadvantages of high cost of synthesis, intricate operation, and low yield of COFs similarly hinder their further application in the field of environment decontamination. Thus, exploring green, simple, low-cost, and straightforward approaches is also a challenge of great urgency. (3) In general, COFs exhibit excellent removal effects toward a single target pollutant, but, in actual water bodies, there are often complex conditions in which multiple pollutants coexist. Therefore, a study on selective adsorption of COF materials is of more crucial practical value and should be further explored. (4) A large number of studies on the removal of environmental pollutants by COFs and COF-based materials have been reported, but the relationship between the structure, performance, and mechanism of COFs remains uncertain. The calculation of DFT, *in situ* XRD, XPS, EXAFS, and other advanced spectral techniques are highly recommended to detect the reaction process to distinguish reactive intermediates from the active sites.

The application of COFs and COF-based materials still presents many challenges in the efficient elimination of pollutants in real applications in large scale, such as the reusability, price, selectivity under complicated conditions, and separation from wastewater. Such problems will be resolved with the development of technology in the future. We believe that COFs and COF-based materials will have huge prospect in environmental pollution management.

REFERENCES

1. Waller, P.J., Gandara, F., and Yaghi, O.M. (2015). Chemistry of covalent organic framework. Acc. Chem. Res. ***48***, 3053–3063.
2. Pyles, D.A., Crowe, J.W., Baldwin, L.A., et al. (2016). Synthesis of benzobisoxazole-linked two-dimensional covalent organic frameworks and their carbon dioxide capture properties. ACS. Macro. Lett. ***5***, 1055–1058.
3. Feng, X., Ding, X.S., and Jiang, D.L. (2012). Covalent organic frameworks. Chem. Soc. Rev. ***41***, 6010–6022.
4. Costa, J.A.S., de Jesus, R.A., da Silva, C.M.P., et al. (2017). Efficient adsorption of a mixture of polycyclic aromatic hydrocarbons (PAHs) by Si-MCM-41 mesoporous molecular sieve. Powder Technol. ***308***, 434–441.
5. Yang, Z.Y., Wang, D.C., Meng, Z.Y., et al. (2019). Adsorption separation of CH4/N-2 on modified coal-based carbon molecular sieve. Sep. Purif. Technol. ***218***, 130–137.
6. Furukawa, H., ordova, K.E., 'Keeffe, M., et al. (2013). The chemistry and applications of metal-organic frameworks. Science ***341***, 974.
7. Wibowo, E., Rokhmat, M., Sutisna, K., et al. (2017). Reduction of seawater salinity by natural zeolite (clinoptilolite): adsorption isotherms, thermodynamics and kinetics. Desalination ***409***, 146–156.
8. Demiral, H., and Gungor, C. (2016). Adsorption of copper(II) from aqueous solutions on activated carbon prepared from grape bagasse. J. Clean. Prod. ***124***, 103–113.
9. Mohan, D., and Pittman, C.U. (2006). Activated carbons and low cost adsorbents for remediation of tri- and hexavalent chromium from water. J. Hazard. Mater. ***137***, 762–811.
10. Pi, Y.H., Li, X.Y., Xia, Q.B., et al. (2018). Adsorptive and photocatalytic removal of persistent organic pollutants (POPs) in water by metal-organic frameworks (MOFs). Chem. Eng. J. ***337***, 351–371.
11. Wu, J.M., Zhou, J.K., Wang, W.A., et al. (2019). Progress in synthesis and application of covalent organic frameworks. Ekoloji ***28***, 4369–4378.
12. Ashourirad, B., Sekizkardes, A.K., Altarawneh, S., et al. (2015). Exceptional gas adsorption properties by nitrogen-doped porous carbons derived from benzimidazole-linked polymers. Chem. Mater. ***27***, 1349–1358.

13. Gao, Q., Bai, L.Y., Zhang, X.J., et al. (2015). Synthesis of microporous nitrogen-rich covalent-organic framework and its application in CO_2 capture. Chin. J. Chem. ***33***, 90–94.
14. Thote, J., Aiyappa, H.B., Deshpande, A., et al. (2014). A covalent organic framework-cadmium sulfide hybrid as a prototype photocatalyst for visible-light-driven hydrogen production. Chem Eur. J. ***20***, 15961–15965.
15. Pachfule, P., Kandambeth, S., Diaz, D.D., et al. (2014). Highly stable covalent organic framework-Au nanoparticles hybrids for enhanced activity for nitrophenol reduction. Chem. Commun. (Camb.) ***50***, 3169–3172.
16. Stegbauer, L., Schwinghammer, K., and Lotsch, B.V. (2014). A hydrazone-based covalent organic framework for photocatalytic hydrogen production. Chem. Sci. ***5***, 2789–2793.
17. Bhanja, P., Bhunia, K., Das, S.K., et al. (2017). New triazine-based covalent organic framework for high-performance capacitive energy storage. ChemSusChem ***10***, 921–929.
18. Vyas, V.S., Haase, F., Stegbauer, L., et al. (2015). A tunable azine covalent organic framework platform for visible light-induced hydrogen generation. Nat. Commun. ***6***, 8508.
19. Xu, F., Jin, S.B., Zhong, H., et al. (2015). Electrochemically active, crystalline, mesoporous covalent organic frameworks on carbon nanotubes for synergistic lithium-ion battery energy storage. Sci. Rep. ***5***, 8225.
20. Kaleeswaran, D., Vishnoi, P., and Murugavel, R. (2015). [3+3] Imine and beta-ketoenamine tethered fluorescent covalent-organic frameworks for CO_2 uptake and nitroaromatic sensing. J. Mater. Chem. ***3***, 7159–7171.
21. Dalapati, S., Jin, S.B., Gao, J., et al. (2013). An azine-linked covalent organic framework. J. Am. Chem. Soc. ***13***, 17310–17313.
22. Bai, L.Y., Phua, S.Z.F., Lim, W.Q., et al. (2016). Nanoscale covalent organic frameworks as smart carriers for drug delivery. Chem. Commun. (Camb.) ***52***, 4128–4131.
23. Zhang, G.Y., Li, X.L., Liao, Q.B., et al. (2018). Water-dispersible PEG-curcumin/amine-functionalized covalent organic framework nanocomposites as smart carriers for in vivo drug delivery. Nat. Commun. ***9***, 2785.
24. Wu, M.X., and Yang, Y.W. (2017). Applications of covalent organic frameworks (COFs): from gas storage and separation to drug delivery. Chin. Chem. Lett. ***28***, 1135–1143.
25. Colson, J.W., Mann, J.A., DeBlase, C.R., et al. (2015). Patterned growth of oriented 2D covalent organic framework thin films on single-layer graphene. J. Polym. Sci. Pol. Chem. ***53***, 378–384.
26. Sun, B., Liu, J., Cao, A.M., Song, W.G., et al. (2017). Interfacial synthesis of ordered and stable covalent organic frameworks on amino-functionalized carbon nanotubes with enhanced electrochemical performance. Chem. Commun. (Camb.) ***53***, 6303–6306.
27. Yao, B.J., Li, J.T., Huang, N., et al. (2018). Pd NP-loaded and covalently cross-linked COF membrane microreactor for aqueous CBs dechlorination at room temperature. ACS Appl. Mater. Interfaces ***10***, 20448–20457.
28. Cote, A.P., Benin, A.I., Ockwig, N.W., et al. (2005). Porous, crystalline, covalent organic frameworks. Science ***310***, 1166–1170.
29. El-Kaderi, H.M., Hunt, J.R., Mendoza-Cortes, J.L., et al. (2007). Designed synthesis of 3D covalent organic frameworks. Science ***316***, 268–272.
30. Kuhn, P., Antonietti, M., and Thomas, A. (2008). Porous, covalent triazine-based frameworks prepared by ionothermal synthesis. Angew. Chem. Int. Ed. ***47***, 3450–3453.
31. Zhao, Y.F., Yao, K.X., Teng, B.Y., et al. (2013). A perfluorinated covalent triazine-based framework for highly selective and water-tolerant CO_2 capture. Energ. Environ. Sci. ***6***, 3684–3692.
32. Yang, H., Yang, L.X., Wang, H.J., et al. (2019). Covalent organic framework membranes through a mixed-dimensional assembly for molecular separations. Nat. Commun. ***10***, 2101.
33. Gui, B., Lin, G.Q., Ding, H.M., et al. (2020). Three-dimensional covalent organic frameworks: from topology design to applications. Acc. Chem. Res. ***53***, 2225–2234.
34. Gao, C., Li, J., Yin, S., Sun, J.L., et al. (2020). Twist building blocks from planar to tetrahedral for the synthesis of covalent organic frameworks. J. Am. Chem. Soc. ***142***, 3718–3723.
35. Wu, C.Y., Liu, Y.M., Liu, H., et al. (2018). Highly conjugated three-dimensional covalent organic frameworks based on spirobifluorene for perovskite solar cell enhancement. J. Am. Chem. Soc. ***140***, 10016–10024.
36. Wang, J.L., and Zhuang, S.T. (2019). Covalent organic frameworks (COFs) for environmental applications. Coordin. Chem. Rev. ***400***, 213046.
37. Haug, W.K., Moscarello, E.M., Wolfson, E.R., et al. (2020). The luminescent and photophysical properties of covalent organic frameworks. Chem. Soc. Rev. ***49***, 839–864.
38. Lan, Y.S., Han, X.H., Tong, M.M., et al. (2018). Materials genomics methods for high-throughput construction of COFs and targeted synthesis. Nat. Commun. ***9***, 5274.
39. Wang, Z.G., Zhang, B.F., Yu, H., et al. (2010). Microporous polyimide networks with large surface areas and their hydrogen storage properties. Chem. Commun. (Camb.) ***46***, 7730–7732.
40. Wang, L.L., Xu, H.M., Qiu, Y.X., et al. (2020). Utilization of Ag nanoparticles anchored in covalent organic frameworks for mercury removal from acidic waste water. J. Hazard. Mater. ***389***, 121824.
41. Xu, S.Q., Zhan, T.G., Wen, Q., et al. (2020). Diversity of covalent organic frameworks (COFs): a 2D COF containing two kinds of triangular micropores of different sizes. Acs Macro Lett. ***5***, 99–102.
42. Uribe-Romo, F.J., Hunt, J.R., Furukawa, H., et al. (2009). A crystalline imine-linked 3-D porous covalent organic framework. J. Am. Chem. Soc. ***131***, 4570.
43. Waller, P.J., AlFaraj, Y.S., Diercks, C.S., et al. (2018). Conversion of imine to oxazole and thiazole linkages in covalent organic frameworks. J. Am. Chem. Soc. ***40***, 9099–9103.
44. Zhuang, X.D., Zhao, W.X., Zhang, F., et al. (2016). A two-dimensional conjugated polymer framework with fully sp(2)-bonded carbon skeleton. Polym. Chem. ***7***, 4176–4181.
45. Zhao, C.F., Diercks, C.S., Zhu, C.H., et al. (2018). Urea-linked covalent organic frameworks. J. Am. Chem. Soc. ***140***, 16438–16441.
46. Chandra, S., Kandambeth, S., Biswal, B.P., et al. (2013). Chemically stable multilayered covalent organic nanosheets from covalent organic frameworks via mechanical delamination. J. Am. Chem. Soc. ***135***, 17853–17861.
47. Wang, H., Wang, H., Wang, Z.W., et al. (2020). Covalent organic framework photocatalysts: structures and applications. Chem. Soc. Rev. ***49***, 4135–4165.
48. Huang, N., Zhai, L.P., Xu, H., et al. (2017). Stable covalent organic frameworks for exceptional mercury removal from aqueous solutions. J. Am. Chem. Soc. ***139***, 2428–2434.
49. Ding, S.Y., Dong, M., Wang, Y.W., et al. (2016). Thioether-based fluorescent covalent organic framework for selective detection and facile removal of mercury(II). J. Am. Chem. Soc. ***138***, 3031–3037.
50. Li, X., Qi, Y., Yue, G.Z., et al. (2019). Solvent- and catalyst-free synthesis of an azine-linked covalent organic framework and the induced tautomerization in the adsorption of U(VI) and Hg(II). Green. Chem. ***21***, 649–657.
51. Li, W.T., Zhuang, Y.T., Wang, J.Y., et al. (2019). A three-dimensional porous organic framework for highly selective capture of mercury and copper ions. ACS Appl. Polym. Mater. ***1***, 2797–2806.
52. Cui, W.R., Jiang, W., Zhang, C.R., et al. (2020). Regenerable carbohydrazide-linked fluorescent covalent organic frameworks for ultrasensitive detection and removal of mercury. Acs. Sustain. Chem. Eng. ***8***, 445–451.
53. Afshari, M., Dinari, M., Zargoosh, K., et al. (2020). Novel triazine-based covalent organic framework as a superadsorbent for the removal of mercury(II) from aqueous solutions. Ind. Eng. Chem. Res. ***59***, 9116–9126.
54. Li, Y.F., Hu, T.L., Chen, R., et al. (2020). Novel thiol-functionalized covalent organic framework as adsorbent for simultaneous removal of BTEX and mercury (II) from water. Chem. Eng. J. ***398***, 125566.
55. Tao, Y., Xiong, X.H., Xiong, J.B., et al. (2020). High-performance removal of mercury ions (II) and mercury vapor by SO_3-anchored covalent organic framework. J. Solid State Chem. ***282***, 121126.
56. Ge, J.L., Xiao, J.D., Liu, L.L., et al. (2016). Facile microwave-assisted production of Fe_3O_4 decorated porous melamine-based covalent organic framework for highly selective removal of Hg^{2+}. J. Porous. Mater. ***23***, 791–800.
57. Huang, L.J., Shen, R.J., Liu, R.Q., et al. (2020). Thiol-functionalized magnetic covalent organic frameworks by a cutting strategy for efficient removal of Hg^{2+} from water. J. Hazard. Mater. ***392***, 122320.
58. Lu, X.F., Ji, W.H., Yuan, L., et al. (2019). Preparation of carboxy-functionalized covalent organic framework for efficient removal of Hg^{2+} and Pb^{2+} from water. Ind. Eng. Chem. Res. ***58***, 17660–17667.
59. Cao, Y., Hu, X., Zhu, C.Q., et al. (2020). Sulfhydryl functionalized covalent organic framework as an efficient adsorbent for selective Pb(II) removal. Colloid. Surf. A ***600***, 125004.
60. Dinari, M., and Hatami, M. (2019). Novel N-riched crystalline covalent organic framework as a highly porous adsorbent for effective cadmium removal. J. Environ. Chem. Eng. ***7***, 102907.
61. Cui, F.Z., Liang, R.R., Qi, Q.Y., et al. (2019). Efficient removal of Cr(VI) from aqueous solutions by a dual-pore covalent organic framework. Adv. Sustain. Syst. ***3***, 1800150.
62. Zhong, X., Lu, Z.P., Liang, W., et al. (2020). The magnetic covalent organic framework as a platform for high-performance extraction of Cr(VI) and bisphenol a from aqueous solution. J. Hazard. Mater. ***393***, 122353.
63. Cao, Y., Hu, X., Zhu, C.Q., et al. (2020). Highly efficient and selective removal of Cr(VI) by covalent organic frameworks: structure, performance and mechanism. Colloid. Surf. A ***600***, 124910.
64. Cai, Y.Y., Jiang, Y., Feng, L.P., et al. (2019). Q-Graphene-scaffolded covalent organic frameworks as fluorescent probes and sorbents for the fluorimetry and removal of copper ions. Anal. Chim. Acta ***1057***, 88–97.
65. Jiang, Y.Z., Liu, C.Y., and Huang, A.S. (2019). EDTA-functionalized covalent organic framework for the removal of heavy-metal ions. ACS Appl. Mater. Interfaces ***11***, 32186–32191.
66. Zhou, Z.M., Zhong, W.F., Cui, K.X., et al. (2018). A covalent organic framework bearing thioether pendant arms for selective detection and recovery of Au from ultra-low concentration aqueous solution. Chem. Commun. (Camb.) ***54***, 9977–9980.
67. Liu, X.S., Xu, H.M., Wang, L.L., et al. (2020). Surface nano-traps of Fe_0/COFs for arsenic(III) depth removal from wastewater in non-ferrous smelting industry. Chem. Eng. J. ***381***, 122559.

68. Yang, C.H., Chang, J.S., and Lee, D.J. (2020). Covalent organic framework EB-COF:Br as adsorbent for phosphorus (V) or arsenic (V) removal from nearly neutral waters. Chemosphere ***253***, 126736.
69. Chen, W.B., Yang, Z.F., Xie, Z., et al. (2019). Benzothiadiazole functionalized D-A type covalent organic frameworks for effective photocatalytic reduction of aqueous chromium(VI). J. Mater. Chem. A ***7***, 998–1004.
70. Xue, K.H., He, R., Yang, T.L., et al. (2019). MOF-based In_2S_3-X_2S_3 (X=Bi; Sb)@TFPT-COFs hybrid materials for enhanced photocatalytic performance under visible light. Appl. Surf. Sci. ***493***, 41–54.
71. Firoozi, M., Rafiee, Z., and Dashtian, K. (2020). New MOF/COF hybrid as a robust adsorbent for simultaneous removal of auramine O and rhodamine B dyes. ACS Omega ***5***, 9420–9428.
72. Lu, Q.Y., Ma, Y.C., Li, H., et al. (2018). Postsynthetic functionalization of three-dimensional covalent organic frameworks for selective extraction of lanthanide ions. Angew. Chem. Int. Ed. ***57***, 6042–6048.
73. Liu, W., Zhang, L., Chen, F., et al. (2020). Efficiency and mechanism of adsorption of low-concentration uranium from water by a new chitosan/aluminum sludge composite aerogel. Dalton Trans. ***49***, 85643.
74. Schnug, E., and Lottermoser, B.G. (2013). Fertilizer-derived uranium and its threat to human health. Environ. Sci. Technol. ***47***, 2433–2434.
75. Casagrande, M.F.S., Moreira, C.A., and Targa, D.A. (2020). Study of generation and underground flow of acid mine drainage in waste rock pile in an uranium mine using electrical resistivity tomography. Pure Appl. Geophys. ***177***, 703–721.
76. Li, Z.D., Zhang, H.Q., Xiong, X.H., et al. (2019). U(VI) adsorption onto covalent organic frameworks-TpPa-1. J. Solid State Chem. ***277***, 484–492.
77. Li, X., Yadav, P., and Loh, K.P. (2020). Function-oriented synthesis of two-dimensional (2D) covalent organic frameworks—from 3D solids to 2D sheets. Chem. Soc. Rev. ***49***, 85964.
78. Kim, G., Yang, J., Nakashima, N., et al. (2017). Highly microporous nitrogen-doped carbon synthesized from azine-linked covalent organic framework and its supercapacitor function. Chem. Eur. J. ***6***, 85632.
79. Jiang, D., Chen, X., Geng, K., et al. (2020). Covalent organic frameworks: chemical approaches to designer structures and built-in functions. Angew. Chem. Int. Ed. ***6***, 89632.
80. You, Z., Zhang, N., Guan, Q., et al. (2019). High sorption capacity of U(VI) by COF-based material doping hydroxyapatite microspheres: kinetic, equilibrium and mechanism investigation. J. Inorg. Organomet. Polym. Mater. ***30***, 1966–1979.
81. Wen, R., Li, Y., Zhang, M.C., et al. (2018). Graphene-synergized 2D covalent organic framework for adsorption: a mutual promotion strategy to achieve stabilization and functionalization simultaneously. J. Hazard. Mater. ***358***, 273–285.
82. Xiong, X.H., Yu, Z.W., Gong, L., et al. (2019). Ammoniating covalent organic framework (COF) for high-performance and selective extraction of toxic and radioactive uranium ions. Adv. Sci. ***6***, 1900547–1900565.
83. Cai, Y., Yuan, F., Wang, X., et al. (2016). Synthesis of core-shell structured Fe_3O_4@carboxymethyl cellulose magnetic composite for highly efficient removal of Eu(III). Cellulose ***24***, 1–16.
84. Neeway, J.J., Asmussen, R.M., Lawter, A.R., et al. (2016). Removal of TcO_4-from representative nuclear waste streams with layered potassium metal sulfide materials. Chem. Mater. ***6***, 86536.
85. Falciglia, P.P., Gagliano, E., Brancato, V., et al. (2020). Microwave based regenerating permeable reactive barriers (MW-PRBs): proof of concept and application for Cs removal. Chemosphere ***251***, 126582.
86. Singh, R., Shitiz, K., and Singh, A. (2020). Immobilization of bacterial cells in hydrogels prepared by gamma irradiation for bioremoval of strontium ions. Water Air Soil Pollut. ***231***, 86956.
87. Zhong, X., Liang, W., Lu, Z., et al. (2020). Highly efficient enrichment mechanism of U(VI) and Eu(III) by covalent organic frameworks with intramolecular hydrogen-bonding from solutions. Appl. Surf. Sci. ***504***, 144403.
88. Yin, Z.J., Xu, S.Q., Zhan, T.G., et al. (2017). Ultrahigh volatile iodine uptake by hollow microspheres formed from a heteropore covalent organic framework. Chem. Commun. (Camb.) ***53***, 7266–7269.
89. Da, H.J., Yang, C.X., and Yan, X.P. (2019). Cationic covalent organic nanosheets for rapid and selective capture of perrhenate: an analogue of radioactive pertechnetate from aqueous solution. Environ. Sci. Technol. ***53***, 5212–5220.
90. Li, Y., Yang, C.X., and Yan, X.P. (2017). Controllable preparation of core-shell magnetic covalent-organic framework nanospheres for efficient adsorption and removal of bisphenols in aqueous solution. Chem. Commun. (Camb.) ***53***, 2511–2514.
91. Wei, D.L., Li, J.C., Chen, Z.S., et al. (2020). Understanding bisphenol-A adsorption in magnetic modified covalent organic frameworks: experiments coupled with DFT calculations. J. Mol. Liq. ***301***, 112431.
92. Liu, Z., Wang, H., Ou, J., et al. (2018). Construction of hierarchically porous monoliths from covalent organic frameworks (COFs) and their application for bisphenol A removal. J. Hazard. Mater. ***355***, 145–153.
93. Gupta, V.K., Kumar, R., Nayak, A., et al. (2013). Adsorptive removal of dyes from aqueous solution onto carbon nanotubes: a review. Adv. Colloid. Interf. Sci. ***193***, 24–34.
94. Yagub, M.T., Sen, T.K., Afroze, S., et al. (2014). Dye and its removal from aqueous solution by adsorption: a review. Adv. Colloid. Interf. Sci. ***209***, 172–184.
95. Rafatullah, M., Sulaiman, O., Hashim, R., et al. (2010). Adsorption of methylene blue on low-cost adsorbents: a review. J. Hazard. Mater. ***177***, 70–80.
96. Huo, J., Luo, B., and Chen, Y. (2019). Crystalline covalent organic frameworks from triazine nodes as porous adsorbents for dye pollutants. ACS Omega ***4***, 22504–22513.
97. Zhu, X., An, S.H., Liu, Y., et al. (2017). Efficient removal of organic dye pollutants using covalent organic frameworks. Aiche J. ***63***, 3470–3478.
98. Su, X.M., Li, X.Y., Li, J.J., et al. (2015). Synthesis and characterization of core-shell magnetic molecularly imprinted polymers for solid-phase extraction and determination of rhodamine B in food. Food Chem. ***171***, 292–297.
99. Li, Y., Chen, W., Hao, W., et al. (2018). Covalent organic frameworks constructed from flexible building blocks with high adsorption capacity for pollutants. ACS. Appl. Nano. Mater. ***1***, 4756–4761.
100. Raval, N.P., Shah, P.U., and Shah, N.K. (2016). Adsorptive amputation of hazardous azo dye Congo red from wastewater: a critical review. Environ. Sci. Pollut. Res. Int. ***23***, 14810–14853.
101. Kandambeth, S., Biswal, B.P., Chaudhari, H.D., et al. (2017). Selective molecular sieving in self-standing porous covalent-organic-framework membranes. Adv. Mater. ***29***, 1603945.
102. Haque, E., Jun, J.W., and Jhung, S.H. (2011). Adsorptive removal of methyl orange and methylene blue from aqueous solution with a metal-organic framework material, iron terephthalate (MOF-235). J. Hazard. Mater. ***185***, 507–511.
103. Yu, S.B., Lyu, H., Tian, J., et al. (2016). A polycationic covalent organic framework: a robust adsorbent for anionic dye pollutants. Polym. Chem. ***7***, 3392–3397.
104. Afshari, M., and Dinari, M. (2020). Synthesis of new imine-linked covalent organic framework as high efficient absorbent and monitoring the removal of direct fast scarlet 4BS textile dye based on mobile phone colorimetric platform. J. Hazard. Mater. ***385***, 121514.
105. Rivera, U.J., Sánchez, P.M., Ferro, G.M.Á., et al. (2013). Pharmaceuticals as emerging contaminants and their removal from water. A review. Chemosphere ***93***, 1268–1287.
106. Wang, J., and Wang, S. (2016). Removal of pharmaceuticals and personal care products (PPCPs) from wastewater: a review. J. Environ. Manage. ***182***, 620–640.
107. Mellah, A., Fernandes, S.P.S., Rodriguez, R., et al. (2018). Adsorption of pharmaceutical pollutants from water using covalent organic frameworks. Chem. A. Eur. J. ***24***, 10601–10605.
108. Li, Z.H., Liu, Y.Y., Zou, S.Y., et al. (2020). Removal and adsorption mechanism of tetracycline and cefotaxime contaminants in water by $NiFe_2O_4$-COF-chitosan-terephthalaldehyde nanocomposites film. Chem. Eng. J. ***382***, 123008.
109. Lamichhane, S., Krishna, K.C.B., and Sarukkalige, R. (2016). Polycyclic aromatic hydrocarbons (PAHs) removal by sorption: a review. Chemosphere ***148***, 336–353.
110. Gao, M.J., Fu, Q.F., Wang, M., et al. (2019). Facile synthesis of porous covalent organic frameworks for the effective extraction of nitroaromatic compounds from water samples. Anal. Chim. Acta ***1084***, 21–32.
111. Wang, W., Wang, J., Zhang, S., et al. (2016). A novel Schiff base network-1 nanocomposite coated fiber for solid-phase microextraction of phenols from honey samples. Talanta ***161***, 22–30.
112. Wang, W., Deng, S.B., Ren, L., et al. (2018). Stable covalent organic frameworks as efficient adsorbents for high and selective removal of an aryl-organophosphorus flame retardant from water. ACS Appl. Mater. Interfaces ***10***, 30265–30272.
113. Ji, S.L., Qian, H.L., Yang, C.X., et al. (2019). Thiol-ene click synthesis of phenylboronic acid-functionalized covalent organic framework for selective catechol removal from aqueous medium. ACS Appl. Mater. Interfaces ***11***, 46219–46225.
114. Ji, W., Xiao, L.L., Ling, Y.H., et al. (2018). Removal of GenX and perfluorinated alkyl substances from water by amine-functionalized covalent organic frameworks. J. Am. Chem. Soc. ***140***, 12677–12681.
115. Salonen, L.M., Pinela, S.R., Fernandes, S.P.S., et al. (2017). Adsorption of marine phycotoxin okadaic acid on a covalent organic framework. J. Chromatogr. A. ***1525***, 17–22.
116. Feng, M.B., Zhang, P., Zhou, H.C., et al. (2018). Water-stable metal-organic frameworks for aqueous removal of heavy metals and radionuclides: a review. Chemosphere ***209***, 783–800.
117. Imam, E.A., El-Sayed, I.E., Mahfouz, M.G., et al. (2018). Synthesis of alpha-aminophosphonate functionalized chitosan sorbents: effect of methyl vs phenyl group on uranium sorption. Chem. Eng. J. ***352***, 1022–1034.
118. Hu, Y.Z., Wang, X.X., Zou, Y.D., et al. (2017). Superior sorption capacities of Ca-Ti and Ca-Al bimetallic oxides for U(VI) from aqueous solutions. Chem. Eng. J. ***316***, 419–428.
119. Liu, X.L., Ma, R., Zhuang, L., et al. (2020). Recent developments of doped g-C_3N_4 photocatalysts for the degradation of organic pollutants. Crit. Rev. Environ. Sci. Technol. https://doi.org/10.1080/10643389.2020.1734433.
120. Wu, Y.H., Pang, H.W., Liu, Y., et al. (2019). Environmental remediation of heavy metal ions by novel-nanomaterials: a review. Environ. Pollut. ***246***, 608–620.
121. Zhao, G.X., Zhang, H.X., Fan, Q.H., et al. (2010). Sorption of copper(II) onto superadsorbent of bentonite-polyacrylamide composites. J. Hazard. Mater. ***173***, 661–668.

122. Yang, S.T., Sheng, G.D., Tan, X.L., et al. (2011). Determination of Ni(II) uptake mechanisms on mordenite surfaces: a combined macroscopic and microscopic approach. Geochim. Cosmochim. Acta ***75***, 6520–6534.
123. Ren, X.M., Li, J.X., Tan, X.L., et al. (2013). Comparative study of graphene oxide, activated carbon and carbon nanotubes as adsorbents for copper decontamination. Dalton Trans. ***42***, 5266–5274.
124. Bhatti, A.A., Memon, S., and Memon, N. (2014). Dichromate extraction by calix[4]arene appended amberlite XAD-4 resin. Sep. Sci. Technol. ***49***, 664–672.
125. Zheng, Q.X., Li, Z.L., Miao, X.X., et al. (2017). Preparation and characterization of novel organic chelating resin and its application in recovery of Zn(II) from aqueous solutions. Appl. Organomet. Chem. ***31***, e3546.
126. Li, J., Chen, C.L., Zhang, S.W., et al. (2014). Surface functional groups and defects on carbon nanotubes affect adsorption-desorption hysteresis of metal cations and oxoanions in water. Environ. Sci. Nano ***1***, 488–495.
127. Wang, X.X., Yang, S.B., Shi, W.Q., et al. (2015). Different interaction mechanisms of Eu(III) and Am-243(III) with carbon nanotubes studied by batch, spectroscopy technique and theoretical calculation. Environ. Sci. Technol. ***49***, 11721–11728.
128. Wang, X.K., Chen, C.L., Hu, W.P., et al. (2005). Sorption of ^{243}Am(III) to multiwall carbon nanotubes. Environ. Sci. Technol. ***39***, 2856–2860.
129. Zou, Y.D., Cao, X.H., Luo, X.P., et al. (2015). Recycle of U(VI) from aqueous solution by situ phosphorylation mesoporous carbon. J. Radioanal. Nucl. Chem. ***306***, 515–525.
130. Sun, Y.B., Wu, Z.Y., Wang, X.X., et al. (2016). Macroscopic and microscopic investigation of U(VI) and Eu(III) adsorption on carbonaceous nanofibers. Environ. Sci. Technol. ***50***, 4459–4467.
131. Cheng, W.C., Ding, C.C., Wang, X.X., et al. (2016). Competitive sorption of As(V) and Cr(VI) on carbonaceous nanofibers. Chem. Eng. J. ***293***, 311–318.
132. Ding, C.C., Cheng, W.C., Wang, X.X., et al. (2016). Competitive sorption of Pb(II), Cu(II) and Ni(II) on carbonaceous nanofibers: a spectroscopic and modeling approach. J. Hazard. Mater. ***313***, 253–261.
133. Zhao, G.X., Li, J.X., Ren, X.M., et al. (2011). Few-layered graphene oxide nanosheets as superior sorbents for heavy metal ion pollution management. Environ. Sci. Technol. ***45***, 10454–10462.
134. Li, J., Zhang, S.W., Chen, C.L., et al. (2012). Removal of Cu(II) and fulvic acid by graphene oxide nanosheets decorated with Fe_3O_4 nanoparticles. ACS Appl. Mater. Interfaces ***4***, 4991–5000.
135. Liu, X.L., Ma, R., Wang, X.X., et al. (2019). Graphene oxide-based materials for efficient removal of heavy metal ions from aqueous solution: a review. Environ. Pollut. ***252***, 62–73.
136. Sun, Y.B., Shao, D.D., Chen, C.L., et al. (2013). Highly efficient enrichment of radionuclides on graphene oxide-supported polyaniline. Environ. Sci. Technol. ***47***, 9904–9910.
137. Guo, R., Jiao, T.F., Li, R.F., et al. (2018). Sandwiched Fe_3O_4/carboxylate graphene oxide nanostructures constructed by layer-by-layer assembly for highly efficient and magnetically recyclable dye removal. ACS. Sustain. Chem. Eng. ***6***, 1279–1288.
138. Xing, R.R., Wang, W., Jiao, T.F., et al. (2017). Bioinspired polydopamine sheathed nanofibers containing carboxylate graphene oxide nanosheet for high-efficient dyes scavenger. ACS. Sustain. Chem. Eng. ***5***, 4948–4956.
139. Liu, J.M., Zhu, K., Jiao, T.F., et al. (2017). Preparation of graphene oxide-polymer composite hydrogels via thiol-ene photopolymerization as efficient dye adsorbents for wastewater treatment. Colloid. Surf. A ***529***, 668–676.
140. Tan, X.L., Fan, Q.H., Wang, X.K., et al. (2009). Eu(III) sorption to TiO_2 (Anatase and Rutile): batch, XPS, and EXAFS studies. Environ. Sci. Technol. ***43***, 3115–3121.
141. Yang, S.T., Sheng, G.D., Montavon, G., et al. (2013). Investigation of Eu(III) immobilization on gamma-Al_2O_3 surfaces by combining batch technique and EXAFS analyses: role of contact time and humic acid. Geochim. Cosmochim. Acta ***121***, 84–104.
142. Li, J., Fan, Q.H., Wu, Y.J., et al. (2016). Magnetic polydopamine decorated with Mg-Al LDH nanoflakes as a novel bio-based adsorbent for simultaneous removal of potentially toxic metals and anionic dyes. J. Mater. Chem. A ***4***, 1737–1746.
143. Wen, T., Wu, X.L., Tan, X.L., et al. (2013). One-pot synthesis of water-swellable Mg-Al layered double hydroxides and graphene oxide nanocomposites for efficient removal of As(V) from aqueous solutions. ACS Appl. Mater. Interfaces ***5***, 3304–3311.
144. Wu, X.L., Tan, X.L., Yang, S.T., et al. (2013). Coexistence of adsorption and coagulation processes of both arsenate and NOM from contaminated groundwater by nanocrystallined Mg/Al layered double hydroxides. Water Res. ***47***, 4159–4168.
145. Gu, P.C., Zhang, S., Li, X., et al. (2018). Recent advances in layered double hydroxide-based nanomaterials for the removal of radionuclides from aqueous solution. Environ. Pollut. ***240***, 493–505.
146. Manos, M.J., and Kanatzidis, M.G. (2016). Metal sulfide ion exchangers: superior sorbents for the capture of toxic and nuclear waste-related metal ions. Chem. Sci. ***7***, 4804–4824.
147. Li, J., Wang, X.X., Zhao, G.X., et al. (2018). Metal-organic framework-based materials: superior adsorbents for the capture of toxic and radioactive metal ions. Chem. Soc. Rev. ***47***, 2322–2356.
148. Zhao, G.X., Huang, X.B., Tang, Z.W., et al. (2018). Polymer-based nanocomposites for heavy metal ions removal from aqueous solution: a review. Polym. Chem. ***9***, 3562–3582.
149. Wang, H.H., Cui, H.Z., Song, X.J., et al. (2020). Facile synthesis of heterojunction of MXenes/TiO_2 nanoparticles towards enhanced hexavalent chromium removal. J. Colloid Interface Sci. ***561***, 46–57.
150. Gan, D.F., Huang, Q., Dou, J.B., et al. (2020). Bioinspired functionalization of MXenes ($Ti_3C_2T_x$) with amino acids for efficient removal of heavy metal ions. Appl. Surf. Sci. ***504***, 144603.
151. Jun, B.M., Kim, S., Heo, J., et al. (2019). Review of MXenes as new nanomaterials for energy storage/delivery and selected environmental applications. Nano. Res. ***12***, 471–487.
152. Zhang, Y.J., Wang, L., Zhang, N.N., et al. (2018). Adsorptive environmental applications of MXene nanomaterials: a review. Rsc. Adv. ***8***, 19895–19905.
153. Guo, X., Zhang, X.T., Zhao, S.J., et al. (2016). High adsorption capacity of heavy metals on two-dimensional MXenes: an ab initio study with molecular dynamics simulation. Phys. Chem. Chem. Phys. ***18***, 228–233.
154. Zhang, T.T., Yang, Y.L., Gao, J.F., et al. (2020). Synergistic degradation of chloramphenicol by ultrasound-enhanced nanoscale zero-valent iron/persulfate treatment. Sep. Purif. Technol. ***240***, 116575.
155. Li, J., Fana, M.J., Li, M., et al. (2020). Cr(VI) removal from groundwater using double surfactant-modified nanoscale zero-valent iron (NZVI): effects of materials in different status. Sci. Total. Environ. ***717***, 137112.
156. Wu, J.X., Wang, B., Cagnetta, G., et al. (2020). Nanoscale zero valent iron-activated persulfate coupled with Fenton oxidation process for typical pharmaceuticals and personal care products degradation. Sep. Purif. Technol. ***239***, 116534.
157. Zhang, Y.T., Jiao, X.Q., Liu, N., et al. (2020). Enhanced removal of aqueous Cr(VI) by a green synthesized nanoscale zero-valent iron supported on oak wood biochar. Chemosphere ***245***, 125542.
158. Zhang, X., Cao, X.Q., Li, G., et al. (2020). Preparation of novel ALRCs/NZVI composite and its removal of Cr(VI) from aqueous. Int. J. Environ. Res. ***14***, 123–133.
159. Lye, J.W.P., Saman, N., Noor, A.M.M., et al. (2020). Application of nanoscale zero-valent iron-loaded natural zeolite for tetracycline removal process. Chem. Eng. Technol. ***43***, 1285–1296.
160. Yi, F.T., Ma, J.Q., Lin, C.W., et al. (2020). Insights into the enhanced adsorption/photocatalysis mechanism of a $Bi_4O_5Br_2$/g-C_3N_4 nanosheet. J. Alloy. Compd. ***821***, 153557.
161. Sahoo, S.K., Padhiari, S., Biswal, S.K., et al. (2020). Fe_3O_4 nanoparticles functionalized GO/g-C_3N_4 nanocomposite: an efficient magnetic nanoadsorbent for adsorptive removal of organic pollutants. Mater. Chem. Phys. ***244***, 122710.
162. Asadi, F., Goharshadi, E.K., and Sadeghinia, M. (2020). Highly efficient solar-catalytic degradation of reactive black 5 dye using mesoporous plasmonic Ag/g-C_3N_4 nanocomposites. ChemistrySelect ***5***, 2735–2745.
163. He, H.B., Luo, Z.Z., and Yu, C.L. (2020). Diatomite-anchored g-C_3N_4 nanosheets for selective removal of organic dyes. J. Alloy. Compd. ***816***, 152652.
164. Feng, Z.M., Huang, C.H., Guo, Y.H., et al. (2020). Graphitic carbon nitride derivative with large mesopores as sorbent for solid-phase microextraction of polycyclic aromatic hydrocarbons. Talanta ***209***, 120541.
165. Fan, W.W., Liu, X.L., Cheng, Y., et al. (2020). Two-dimensional metal-organic framework nanobelts for selective Fe^{3+} removal from aqueous solution with high adsorption capacity. Sep. Purif. Technol. ***239***, 116559.
166. Sun, S.W., Yang, Z.H., Cao, J., et al. (2020). Copper-doped ZIF-8 with high adsorption performance for removal of tetracycline from aqueous solution. J. Solid State Chem. ***285***, 121219.
167. Wu, Y.H., Li, B.Y., Wang, X.X., et al. (2019). Magnetic metal-organic frameworks (Fe_3O_4@ZIF-8) composites for U(VI) and Eu(III) elimination: simultaneously achieve favorable stability and functionality. Chem. Eng. J. ***378***, 122105.
168. Wu, Y.H., Li, B.Y., Wang, X.X., et al. (2018). Synthesis of rod-like metal-organic framework (MOF-5) nanomaterial for efficient removal of U(VI): batch experiments and spectroscopy study. Sci. Bull. ***63***, 831–839.
169. Zhuang, S.T., Chen, R., Liu, Y., et al. (2020). Magnetic COFs for the adsorptive removal of diclofenac and sulfamethazine from aqueous solution: adsorption kinetics, isotherms study and DFT calculation. J. Hazard. Mater. ***385***, 121596.
170. Zhuang, S.T., Liu, Y., and Wang, J.L. (2020). Covalent organic frameworks as efficient adsorbent for sulfamerazine removal from aqueous solution. J. Hazard. Mater. ***383***, 121126.
171. Sharma, R.K., Yadav, P., Yadav, M., et al. (2020). Recent development of covalent organic frameworks (COFs): synthesis and catalytic (organic-electro-photo) applications. Mater. Horiz. ***7***, 411–445.
172. Narayani, M., and Shetty, K.V. (2013). Chromium-resistant bacteria and their environmental condition for hexavalent chromium removal: a review. Crit. Rev. Environ. Sci. Technol. ***43***, 955–1009.
173. Zhang, S., Gu, P.C., Ma, R., et al. (2019). Recent developments in fabrication and structure regulation of visible-light-driven g-C_3N_4-based photocatalysts towards water purification: a critical review. Catal. Today ***335***, 65–77.
174. Ding, S.Y., and Wang, W. (2013). Covalent organic frameworks (COFs): from design to applications. Chem. Soc. Rev. ***42***, 548–568.

175. Liu, N., Shi, L.F., Han, X.H., et al. (2020). A heteropore covalent organic framework for adsorptive removal of Cd(II) from aqueous solutions with high efficiency. Chin. Chem. Lett. ***31***, 386–390.
176. Yue, J.Y., Wang, L., Ma, Y., et al. (2019). Metal ion-assisted carboxyl-containing covalent organic frameworks for the efficient removal of Congo red. Dalton Trans. ***48***, 17763–17769.
177. Li, L.Y., Hu, J.W., Shi, X.D., et al. (2016). Nanoscale zero-valent metals: a review of synthesis, characterization, and applications to environmental remediation. Environ. Sci. Pollut. Res. Int. ***23***, 17880–17900.
178. Liu, Y.Q., and Landskron, K. (2017). Anionic porous organic frameworks as advanced functional adsorbents for CO_2 and organic micropollutants in water. J. Mater. Chem. A ***5***, 23523–23529.
179. Li, G.L., Ye, J.R., Fang, Q.L., et al. (2019). Amide-based covalent organic frameworks materials for efficient and recyclable removal of heavy metal lead(II). Chem. Eng. J. ***370***, 822–830.
180. Wang, Z.Q., and Cohen, S.M. (2009). Postsynthetic modification of metal-organic frameworks. Chem. Soc. Rev. ***38***, 1315–1329.
181. Sun, Q., Aguila, B., Earl, L.D., et al. (2018). Covalent organic frameworks as a decorating platform for utilization and affinity enhancement of chelating sites for radionuclide sequestration. Adv. Mater. ***30***, 1705479.
182. Sun, Q., Aguila, B., Perman, J., et al. (2017). Postsynthetically modified covalent organic frameworks for efficient and effective mercury removal. J. Am. Chem. Soc. ***139***, 2786–2793.
183. Bai, C.Y., Zhang, M.C., Li, B., et al. (2016). Modifiable diyne-based covalent organic framework: a versatile platform for in situ multipurpose functionalization. Rsc. Adv. ***6***, 39150–39158.
184. Meri-Bofi, L., Royuela, S., Zamora, F., et al. (2017). Thiol grafted imine-based covalent organic frameworks for water remediation through selective removal of Hg(II). J. Mater. Chem. A ***5***, 17973–17981.
185. Xu, H., Chen, X., Gao, J., et al. (2014). Catalytic covalent organic frameworks via pore surface engineering. Chem. Commun. (Camb.) ***50***, 1292–1294.
186. Hou, Y.X., Zhang, X.M., Wang, C.M., et al. (2017). Novel imine-linked porphyrin covalent organic frameworks with good adsorption removing properties of RhB. New J. Chem. ***41***, 6145–6151.
187. Colson, J.W., Woll, A.R., Mukherjee, A., et al. (2011). Oriented 2D covalent organic framework thin films on single-layer graphene. Science ***332***, 228–231.
188. Karak, S., Dey, K., Torris, A., et al. (2019). Inducing disorder in order: hierarchically porous covalent organic framework nanostructures for rapid removal of persistent organic pollutants. J. Am. Chem. Soc. ***141***, 7572–7581.
189. Hawkes, J.S. (1997). Heavy metals. J. Chem. Educ. ***74***, 1369–1374.
190. Duruibe, J.O., Ogwuegbu, M.O.C., and Egwurugwu, J.N. (2007). Heavy metal pollution and human biotoxic effects. Int. J. Phys. Sci. ***2***, 112–118.
191. Kurniawan, T.A., Chan, G.Y.S., Lo, W.H., et al. (2006). Physico-chemical treatment techniques for wastewater laden with heavy metals. Chem. Eng. J. ***118***, 83–98.
192. Azimi, A., Azari, A., Rezakazemi, M., et al. (2017). Removal of heavy metals from industrial wastewaters: a review. Chembioeng Rev. ***4***, 37–59.
193. Lv, S.W., Liu, J.M., Wang, Z.H., et al. (2019). Recent advances on porous organic frameworks for the adsorptive removal of hazardous materials. J. Environ. Sci. ***80***, 169–185.
194. Jiang, C.L., Wang, X.H., Wang, G.H., et al. (2019). Adsorption performance of a polysaccharide composite hydrogel based on crosslinked glucan/chitosan for heavy metal ions. Compos. B Eng. ***169***, 45–54.
195. Huang, D., Wu, J., Wang, L., et al. (2019). Novel insight into adsorption and co-adsorption of heavy metal ions and an organic pollutant by magnetic graphene nanomaterials in water. Chem. Eng. J. ***358***, 1399–1409.
196. Zhan, W.W., Gao, L., Fu, X., et al. (2019). Green synthesis of amino-functionalized carbon nanotube-graphene hybrid aerogels for high performance heavy metal ions removal. Appl. Surf. Sci. ***467***, 1122–1133.
197. Zarei, F., Marjani, A., and Joshaghani, A.H. (2019). Triamino-anchored KCC-1: a novel and promising adsorbent for fast and highly effective aqueous Cr-VI removal. J. Environ. Chem. Eng. ***7***, 103309.
198. Chen, W.Q., Lu, Z.H., Xiao, B.H., et al. (2019). Enhanced removal of lead ions from aqueous solution by iron oxide nanomaterials with cobalt and nickel doping. J. Clean. Prod. ***211***, 1250–1258.
199. Hu, H.J., Liu, J.Y., Xu, Z.H., et al. (2019). Hierarchical porous Ni/Co-LDH hollow dodecahedron with excellent adsorption property for Congo red and Cr(VI) ions. Appl. Surf. Sci. ***478***, 981–990.
200. Li, Z.T., Wang, L., Meng, J., et al. (2018). Zeolite-supported nanoscale zero-valent iron: new findings on simultaneous adsorption of Cd(II), Pb(II), and As(III) in aqueous solution and soil. J. Hazard. Mater. ***344***, 1–11.
201. Liao, Q., Pan, W., Zou, D.S., et al. (2018). Using of g-C_3N_4 nanosheets for the highly efficient scavenging of heavy metals at environmental relevant concentrations. J. Mol. Liq. ***261***, 32–40.
202. Thanh, H.T.M., Phuong, T.T.T., Hang, P.T.L., et al. (2018). Comparative study of Pb(II) adsorption onto MIL-101 and Fe-MIL-101 from aqueous solutions. J. Environ. Chem. Eng. ***6***, 4093–4102.
203. Huang, Y., Zeng, X.F., Guo, L.L., et al. (2018). Heavy metal ion removal of wastewater by zeolite-imidazolate frameworks. Sep. Purif. Technol. ***194***, 462–469.
204. Li, J., Yang, X.D., Bai, C.Y., et al. (2015). A novel benzimidazole-functionalized 2D COF material: synthesis and application as a selective solid-phase extractant for separation of uranium. J. Colloid Interface Sci. ***437***, 211–218.
205. Mahmoud, M.E., Khalifa, M.A., El Wakeel, Y.M., et al. (2017). Engineered nano-magnetic iron oxide-urea-activated carbon nanolayer sorbent for potential removal of uranium(VI) from aqueous solution. J. Nucl. Mater. ***487***, 13–22.
206. Zhang, R., Chen, C., Li, J., et al. (2015). Preparation of montmorillonite@carbon composite and its application for U(VI) removal from aqueous solution. Appl. Surf. Sci. ***349***, 129–137.
207. Song, S.A., Huang, S.Y., Zhang, R., et al. (2017). Simultaneous removal of U(VI) and humic acid on defective TiO_{2-x} investigated by batch and spectroscopy techniques. Chem. Eng. J. ***325***, 576–587.
208. Yan, L.G., Yang, K., Shan, R.R., et al. (2015). Kinetic, isotherm and thermodynamic investigations of phosphate adsorption onto core-shell Fe_3O_4@LDHs composites with easy magnetic separation assistance. J. Colloid Interface Sci. ***448***, 508–516.
209. Liu, H.B., Li, M.X., Chen, T.H., et al. (2017). New synthesis of nZVI/C composites as an efficient adsorbent for the uptake of U(VI) from aqueous solutions. Environ. Sci. Technol. ***51***, 9227–9234.
210. Li, Y., Li, L.Y., Chen, T., et al. (2018). Bioassembly of fungal hypha/graphene oxide aerogel as high performance adsorbents for U(VI) removal. Chem. Eng. J. ***347***, 407–414.
211. Liu, Y., Zhao, Z., Yuan, D., et al. (2018). Fast and high amount of U(VI) uptake by functional magnetic carbon nanotubes with phosphate group. Ind. Eng. Chem. Res. ***57***, 14551–14560.
212. Zhang, X., Liu, Y., Jiao, Y., et al. (2019). Enhanced selectively removal uranyl ions from aqueous solution by Fe@ZIF-8. Microporous Mesoporous Mater. ***277***, 52–59.
213. Yang, L.X., Feng, X.F., Yin, W.H., et al. (2018). Metal-organic framework containing both azo and amide groups for effective U(VI) removal. J. Solid State Chem. ***265***, 148–154.
214. Song, W., Wang, X., Wang, Q., et al. (2015). Plasma-induced grafting of polyacrylamide on graphene oxide nanosheets for simultaneous removal of radionuclides. Phys. Chem. Chem. Phys. ***17***, 398–406.
215. Liao, Q., Zou, D.S., Pan, W., et al. (2018). Highly efficient capture of Eu(III), La(III), Nd(III), Th(IV) from aqueous solutions using g-C_3N_4 nanosheets. J. Mol. Liq. ***252***, 351–361.
216. Huang, S.Y., Pang, H.W., Li, L., et al. (2018). Unexpected ultrafast and high adsorption of U(VI) and Eu(III) from solution using porous Al_2O_3 microspheres derived from MIL-53. Chem. Eng. J. ***353***, 157–166.
217. He, L.W., Liu, S.T., and Long, C. (2019). Mechanism unravelling for ultrafast and selective $^{99}TcO^{4-}$ Uptake by a radiation-resistant cationic covalent organic framework: a combined radiological experiment and molecular dynamics simulation study. Chem. Sci. ***10***, 4293–4305.
218. Zhu, L., Sheng, D.P., Xu, C., et al. (2017). Identifying the recognition site for selective trapping of $^{99}TcO_4^-$ in a hydrolytically stable and radiation resistant cationic metal-organic framework. J. Am. Chem. Soc. ***139***, 14873–14876.
219. Banerjee, D., Xu, W.Q., Nie, Z.M., et al. (2016). Zirconium-based metal-organic framework for removal of perrhenate from water. Inorg. Chem. ***55***, 8241–8253.
220. Cheng, R., Kang, M., and Zhuang, S. (2019). Adsorption of Sr(II) from water by mercerized bacterial cellulose membrane modified with EDTA. J. Hazard. Mater. ***364***, 645–653.
221. Basu, H., Pimple, M.V., and Saha, S. (2020). TiO_2 microsphere impregnated alginate: a novel hybrid sorbent for uranium removal from aquatic bodies. New J. Chem. ***44***, 85325.
222. Wang, X., Dai, X., Shi, C., et al. (2019). A 3,2-hydroxypyridinone-based decorporation agent that removes uranium from bones in vivo. Nat. Commun. ***10***, 85632.
223. Panda, A., Yanqin, Y., Venkateswarlu, S., et al. (2020). Highly durable covalent organic framework for the simultaneous ultrasensitive detection and removal of noxious Hg^{2+}. Micropor. Mesopor. Ma. ***6***, 523–536.
224. Xu, T., An, S., Peng, C., et al. (2020). Construction of large-pore crystalline covalent organic framework as high-performance adsorbent for rhodamine B dye removal. Ind. Eng. Chem. Res. ***6***, 86954.
225. Rahmanian, O., Falsafin, M., and Dinari, M. (2020). High surface area benzimidazole based porous covalent organic framework for removal of methylene blue from aqueous solutions. Polym. Int. ***69***, 712–718, https://doi.org/10.1002/pi.6007.
226. Ding, H., Mal, A., and Wang, C. (2020). Tailored covalent organic frameworks by post-synthetic modification. Mater. Chem. Front. ***4***, 113–127.
227. Jiang, C.L., Wang, X.H., Wang, G.H., et al. (2020). Amino bearing core-shell structured magnetic covalent organic framework nanospheres: preparation, postsynthetic modification with phenylboronic acid and enrichment of monoamine neurotransmitters in human urine. Anal. Chim. Acta ***1093***, 61–74.
228. Li, H., Li, H., Dai, Q., et al. (2018). Hydrolytic stability of boronate ester-linked covalent organic frameworks. Adv. Theor. Simul. ***6***, 1700015.

229. Lei, Z.D., Yang, Q.S., Xu, Y., et al. (2018). Boosting lithium storage in covalent organic framework via activation of 14-electron redox chemistry. Nat. Commun. ***9***, 576.
230. Liu, Q., Fang, Q., Chu, W.S., et al. (2017). Electron-doped 1T-MoS_2 via interface engineering for enhanced electrocatalytic hydrogen evolution. Chem. Mater. ***29***, 4738–4744.
231. Zhang, W.J., Hu, Y., Ma, L.B., et al. (2018). Progress and perspective of electrocatalytic CO_2 reduction for renewable carbonaceous fuels and chemicals. Adv. Sci. ***5***, 1700275–1700286.
232. Cui, W.R., Li, F.F., Xu, R.H., et al. (2020). Regenerable covalent organic frameworks for photo-enhanced uranium adsorption from seawater. Angew. Chem. Int. Ed. ***6***, 75078.
233. Aksu, Z. (2005). Application of biosorption for the removal of organic pollutants: a review. Process. Biochem. ***40***, 997–1026.
234. Das, R., Vecitis, C.D., Schulze, A., et al. (2017). Recent advances in nanomaterials for water protection and monitoring. Chem. Soc. Rev. ***46***, 6946–7020.
235. Gibson, L.T. (2014). Mesosilica materials and organic pollutant adsorption. Part B. Removal from aqueous solution. Chem. Soc. Rev. ***43***, 5173–5182.
236. Lin, K., Liu, W., and Gan, J. (2009). Oxidative removal of bisphenol A by manganese dioxide: efficacy, products, and pathways. Environ. Sci. Technol. ***43***, 3860–3864.
237. Li, Y.X., Zhang, H., Chen, Y., et al. (2019). Core-shell structured magnetic covalent organic framework nanocomposites for triclosan and triclocarban adsorption. ACS Appl. Mater. Interfaces ***11***, 22492–22500.
238. Li, Y., Wang, C., Ma, S.J., et al. (2019). Fabrication of hydrazone-linked covalent organic frameworks using alkyl amine as building block for high adsorption capacity of metal ions. ACS Appl. Mater. Interfaces ***11***, 11706–11714.
239. Arica, T.A., Ayas, E., and Arica, M.Y. (2017). Magnetic MCM-41 silica particles grafted with poly(glycidylmethacrylate) brush: modification and application for removal of direct dyes. Micropor Mesopor Mat ***243***, 164–175.
240. Li, Y., Yang, C.X., Qian, H.L., et al. (2019). Carboxyl-functionalized covalent organic frameworks for the adsorption and removal of triphenylmethane dyes. ACS Appl. Nano Mater. ***2***, 7290–7298.
241. Yu, S.J., Wang, X.X., Pang, H.W., et al. (2018). Boron nitride-based materials for the removal of pollutants from aqueous solutions: a review. Chem. Eng. J. ***333***, 343–360.
242. Bae, S., Collins, R.N., Waite, T.D., et al. (2018). Advances in surface passivation of nanoscale zerovalent iron: a critical review. Environ. Sci. Technol. ***52***, 12010–12025.
243. Guo, X.H., Tian, Y., Zhang, M.C., et al. (2018). Mechanistic insight into hydrogen-bond-controlled crystallinity and adsorption property of covalent organic frameworks from flexible building blocks. Chem. Mater. ***30***, 2299–2308.
244. Li, F.F., Cui, W.R., Jiang, W., et al. (2020). Stable sp2 carbon-conjugated covalent organic framework for detection and efficient adsorption of uranium from radioactive wastewater. J. Hazard. Mater. ***392***, 122333.
245. Hu, J., Tan, X.L., Ren, X.M., et al. (2012). Effect of humic acid on nickel(II) sorption to Ca-montmorillonite by batch and EXAFS techniques study. Dalton Trans. ***41***, 10803–10810.
246. Ren, X.M., Yang, S.T., Hu, F.C., et al. (2013). Microscopic level investigation of Ni(II) sorption on Na-rectorite by EXAFS technique combined with statistical F-tests. J. Hazard. Mater. ***252***, 2–10.
247. Chen, C.C., McKimmy, E.J., Pinnavaia, T.J., et al. (2004). XAS study of mercury(II) ions trapped in mercaptan-functionalized mesostructured silicate with a wormhole framework structure. Environ. Sci. Technol. ***38***, 4758–4762.
248. Li, Y., Guo, X.H., Li, X.F., et al. (2020). Redox-active two-dimensional covalent organic frameworks (COFs) for selective reductive separation of valence-variable, redox-sensitive and long-lived radionuclides. Angew. Chem. Int. Ed. ***59***, 4168–4175.

ACKNOWLEDGMENTS

Financial support from NSFC (21836001), National Key Research and Development Program of China (2017YFA0207002 and 2018YFC1900105), Science Challenge Project (TZ2016004), and Beijing Outstanding Young Scientist Program were greatly appreciated.

DECLARATION OF INTERESTS

The authors declare that they have no conflicts of interest.

SUPPLEMENTAL INFORMATION

Supplemental Information can be found online at https://doi.org/10.1016/j.xinn.2021.100076.

The Innovation, Volume *2*

Supplemental Information

Orderly Porous Covalent Organic Frameworks-based Materials: Superior Adsorbents for Pollutants Removal from Aqueous Solutions

Xiaolu Liu, Hongwei Pang, Xuewei Liu, Qian Li, Ning Zhang, Liang Mao, Muqing Qiu, Baowei Hu, Hui Yang, and Xiangke Wang

Supplementary Information for

Orderly porous covalent organic frameworks-based materials: superior adsorbents for pollutants removal from aqueous solutions

Xiaolu Liu[1,2], Hongwei Pang[2], Xuewei Liu[2], Qian Li[2], Ning Zhang[2], Liang Mao[3], Muqing Qiu[1], Baowei Hu[1,*], Hui Yang[2,*], Xiangke Wang[2]*

1. School of Life Science, Shaoxing University, Huancheng West Road 508, Shaoxing, 312000, P.R. China

2. College of Environmental Science and Engineering, North China Electric Power University, Beijing, 102206, P.R. China

3. State Key Laboratory of Pollution Control and Resource Reuse, School of the Environment, Nanjing University, Nanjing, 210093, P.R. China

*: Corresponding author. Email: xkwang@ncepu.edu.cn (X. Wang), h.yang@ncepu.edu.cn (H. Yang); hbw@usx.edu.cn (B. Hu).

Contents:

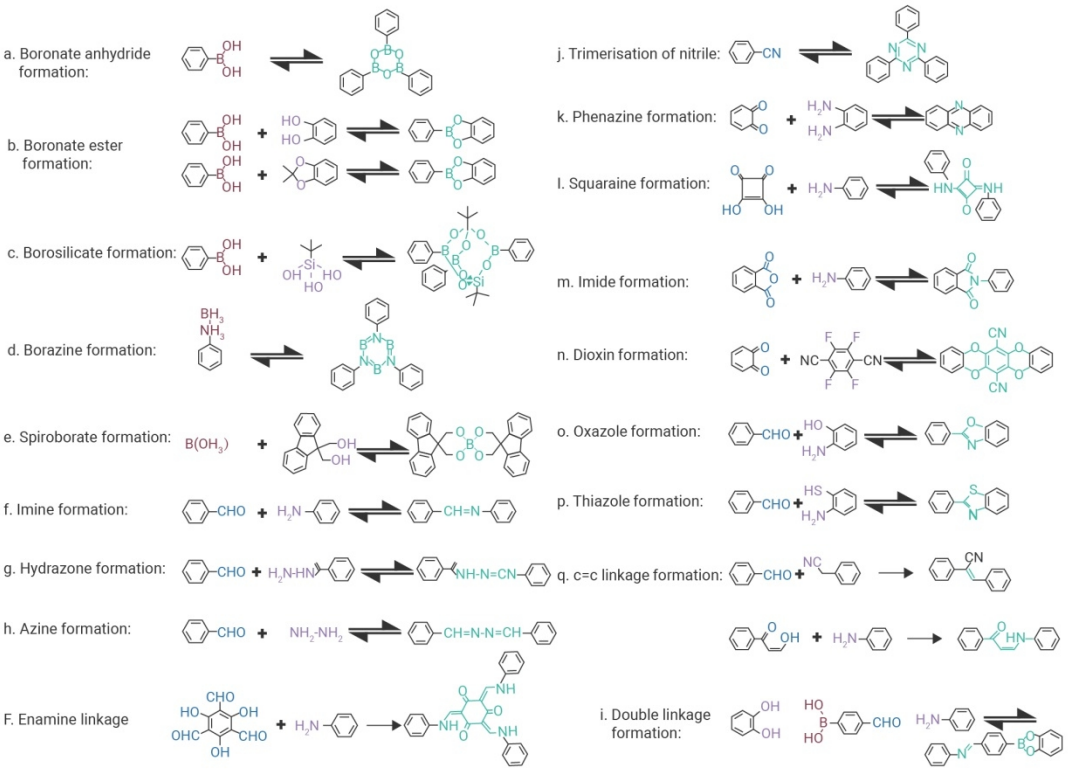

Fig. S1. Various linkages of COF formation[1].

Table S1 The typical kinetic and thermodynamic models commonly used to describe the adsorption process by COF-based materials.

	Equation	Parameters	Ref
Isotherm models			
Langmuir model	$C_e/q_e=1/(K_Lq_m)+C_e/q_m$ $R_L=1/(1+K_LC_0)$	C_e(mg·L^{-1}) equilibrium concentration; q_e(mg·g^{-1}) adsorption capacity at equilibrium time; K_L(L·mg^{-1}) the Langmuir constant; q_m(mg·g^{-1}) the maximum adsorption capacity; R_L the dimensionless parameter; C_0(mg·L^{-1}) highest concentration of the adsorbates;	2, 3
Freundlich model	$lnq_e = lnK_F + lnC_e/n$	K_F (mg·L^{-1}) the Freundlich constant; n-a constant describing the adsorption density;	2
Dubinin-Radushkevich	$lnq_e=lnq_m-K\varepsilon^2$ $E_D=1/(2K)^{½}$	K(mol^2/J^2) a constant; ε-the Polanyi potential; E_D (KJ·mol^{-1})	4
Temkin	$q_e=(R*T/b_T)lnK_T + (R*T/b_T)lnC_e$	K_T(L·g^{-1}) Temkin constant; R(J/mol·K) constant 8.314; b_T(KJ·mol^{-1}) Temkin constant related to the heat of adsorption	5
Sips model	$q_e=q_m(KC_e)^n/[1+(kC_e)^n]$	k((mg·L^{-1})$^{-n}$) the constant of the sips models; n-the index of heterogeneity	6
Kinetic models			
Pseudo first-order model	$ln[(q_e-q_t)/q_e]=-K_1q_et$	q_t(mg·g^{-1}) the adsorption capacity at the time t; K_1(min^{-1}) pseudo-first-order rate constant of the adsorption;	5
Pseudo second-order model	$t/q_t=t/q_m+1/(K_2q_e^2)$	K_2 (g·mg^{-1}·min^{-1}) pseudo-second-order rate constant of the adsorption	5

Intraparticle diffusion model	$q_t=K_i t^{1/2}+C$	K_i(mg·g^{-1}·min$^{-1/2}$) the intraparticle diffusion rate constant; C the intercept related to the boundary thickness	4
Elovich model	$q_t=\ln(\alpha\beta)/\beta+\ln(t)/\beta$	α-the initial adsorption rate; β-the desorption constant	4
Thermodynamic model	$K_0 = q_e/C_e$ $\Delta G = -RT \ln K_0$ $\ln K_0 = \Delta S/R-\Delta H/(RT)$	entropy change (ΔS, J·mol^{-1} K^{-1}); free energy change (ΔG, kJ·mol^{-1}); enthalpy change (ΔH, kJ·mol^{-1}); the thermodynamic equilibrium constant (K^0); the universal gas constant (R 8.314 J·mol^{-1} K^{-1})	7

Table S2 Abbreviations.

(CP/MAS) NMRs	The solid-state 13C cross-polarization magic-angle-spinning (CP/MAS) NMR spectroscopy
$[NH_4^+]$ $[COF\text{-}SO_3^-]$	SO_3^--anchored COF
$[P(O_2Ph)_3]^-$	Hexa-coordinated phosphorus moieties
2D	Two-dimensional
3D	Three-dimensional
3D ionic COFs	Tetrakis (4-formylphenyl) methane + diimidium bromide
ACOF	Azine-linked COF
ACs	Activated carbons
Ag NPs@COF	Ag nanoparticles@COF
Ag NPs@COF-LZU1	COF-supported Ag NPs material
BD	benzidine
BD-(CF3)2	3,3'-bis(trifluoromethyl)benzidine
BFBP2 +·$2Cl^-$	1,1-bis(4-formylphenyl)-4,4'-bipyridinium dichloride
BG	brilliant green
BIPY	bipyridine
BPA	Bisphenol A
CMPs	Conjugated microporous polymers
CNFs	Carbon nanofibers
CNTs	Carbon nanotubes
COF1	1,3,5-triaminobenzene (TAB) + 2,3-dihydroxyterephthalaldehyde (2,3-Dha)
COF-102	tetra-boronic acid + allyl-functionalized truncating
COF-103	tetra(4-(dihydroxy)borylphenyl) silane
COF2	1,3,5-triaminobenzene (TAB) + 2,5-dihydroxyterephthalaldehyde (2,5-Dha)
COF-366-Co	5,10,15,20-tetrakis(4-aminophenyl) porphinato] cobalt [Co(TAP)] + 1,4-benzenedi carboxaldehyde
COF-BTA-DHBZ	3,3′-dihydroxybenzidine (DHBZ) + [1,1′-biphenyl]-3,3′,5,5′-tetracarbaldehyde (BTA)
COF-COOH	carboxyl-containing COF
COF-ETTA-2,3-Dha	4,4′,4″,4‴-(ethene-1,1,2,2-tetrayl)tetraaniline (ETTA) + 2,3-dihydroxybenzene-1,4-dicarbaldehyde (2,3-Dha))
COF-LZU8	Thioether-functionalized hydrazone-linked COF
COF-LZU8	Thioether-functionalized hydrazone-linked COF
COFs	Covalent organic frameworks
COF-SH	Sulfhydryl functionalized COF
COF-S-SH	Sulfur-based chelating-group-laced COF
COF-S-SH	Thiol-functionalized COF
COF-TE	Amide-rich layered COF (1,3,5-trimesoyl chloride + p-Phenylenediamine)

COF-TP	Amide-rich layered COF (1,3,5-trimesoyl chloride + p-Phenylenediamine)
COF-TpPa-1	COF-2,4,6-Triformylphloroglucinol pPhenylenediamine
COF-TpPa-1-nc	1, 3, 5-triformylphloroglucinol+ p-phenylenediamine
COF-V (synthesized by Li et al.)	V inyl-incorporated COF (2,5-Divinylterephthalaldehyde (DVA) + 1,3,5-tris(4"-aminobiphenyl)benzene (TABPB))
COF-V (synthesized by Sun et al.)	Vinyl-functionalized COF (2,5-divinylterephthalaldehyde (Dva) + 1,3,5-tris(4-aminophenyl)-benzene (Tab))
COM	COF membrane
COOH@COF	Carboxyl functionalized COF
CR	Congo red
CTX	cefotaxime
CuP-DMNDA-COF	Imine-linked functionalized COFs
CuTAPP	5,10,15,20-tetra(p-aminophenyl) porphyrinatocopper(II)
CV	crystal violet
DBA	4,4’-diamino-[1,1’-biphenyl]-3,3’-dicarboxylic acid
DBd	4,4’-diamino-[1,1’-biphenyl]-2,2’-dicarboxylic acid
DCC	Dynamic covalent chemistry
DFS-4BS	direct fast scarlet 4BS
DFT	Density functional theory
DHBD	3,3′-dihydroxybenzidine
DMBD	2,2′-dimethyl-[1,1′-biphenyl]-4,4′-diamine-COF
DMNDA	2,6-dimethoxynaphthalene-1,5-dicarbaldehyde
DMTA	2,5-dimethoxyterephthalaldehyde
DMTP	dimethoxyterephthaldehyde
DT	4,4″-diamino-pterphenyl
EB-COF:Br	1,3,5-trifomylphloroglucinol (TFP) + ethidium bromide (EB)
EDC	endocrine-disrupting chemicals
EIS	electrochemical impedancespectroscopy
EPA	Environmental Protection Agency
EXAFS	Extended X-ray absorption fine structure spectroscopy
Fe0/TAPB-PDA COFs composites	1,3,5-tris(4-aminophenyl)benzene (TAPB) + terephthalaldehyde (PDA) + zero-valent iron (Fe0) nanoparticles
Fe_3O_4@TpPa-1	1,4-diaminobenzene (Pa-1) + 1, 3, 5-triformylphloroglucinol (Tp) + amino-functionalized magnetic Fe3O4 (Fe3O4-NH2)
FT-IR	Fourier transform infrared spectroscopy
g-C_3N_4	Graphitic carbon nitride
GenX	ammonium perfluoro-2-propoxypropionate
GO	Graphene oxides
IARC	International Agency for Research on Cancer
IAST	A method established for evaluation of metal ion uptakes by variety of adsorbents

Kd	Constant of distribution, L/g
Ksp	The solubility product constant, Ksp, is the equilibrium constant for a solid substance dissolving in an aqueous solution. It represents the level at which a solute dissolves in solution. The more soluble a substance is, the higher the Ksp value it has
LDHs	Layered double hydroxides
LMS	Layered metal sulfides
M18	monolith with 16% COF powder
M28	monolith with 28% COF powder
MB	Methylene blue
M-COF	Melamine-based COF
M-COF-SH	Thiol-functionalized COF composite
MO	Methyl orange
MOFs	Metal organic frameworks
MSPE	magnetic solid-phase extraction
MW	molecular weight
NACs	nitroaromatic compounds
NCCT	$NiFe_2O_4$/COF/CS/TPA nanocomposites film
ND	1,5-naphalenediamine
NZVI	Nanoscale zero-valent iron
OA	okadaic acid
OMC	Ordered mesoporous carbon
Pa-2	p-phenylenediamine (2,5-dimethyl-pphenylenediamine)
PAHs	Polycyclic aromatic hydrocarbon
PA-POFs	COFs with tetra-coordinated phosphate functional groups
PDA	p-phenylenediamine
PFAS	Per-/polyfluorinated alkyl substances
PFOA	perfluorooctanoic acid
pHzpc	The pH at zero-point charge
POFct-1	3D porous organic framework (crystal-type)
POFct-2	3D porous organic framework (amorphous)
POPs	Persistent organic pollutants
PPCPs	pharmaceutical and personal care products
PTSA	ptoluene sulfonic acid
P-WCA-POFs	COFs with hexa-coordinated phosphorus moieties
PXRD	powder X-ray diffraction pattern
QG-scaffolded COFs	Q-graphene (QG) + melanine (MA) + paraformaldehyde (PA) + phenol (Phen)
RhB	Rhodamine B
SA	succinic anhydride
SAXS	Small-angle X-ray scattering
SMT	Sulfamerazine
SNW-1	Schiff-based networks

TAPB	1,3,5-tris(4-aminophenyl) benzene
TAPB-BMTTPA-COF	1,3,5-tris(4-aminophenyl)benzene (TAPB) + 2,5-bis(methylthio)terephthalaldehyde (BMTTPA)
TC	Tetracycline
TCC	Triclocarban
TCOF/ T-COF	Triazine-based COF
TCS	Triclosan
TFBODH	Oxalyldihydrazide (ODH) + 1,3,5-triformylbenzene (TFB)
TFP	1,3,5-Triformylphloroglucinol
TFPM	tetra(4-formylphenyl)methane
TFPOT	1,3,5-triazine and 2,4,6-tris(4-formylphenoxy)-1,3,5-triazine
TFPPy-CHYD	1,3,6,8-tetrakis(4-formylphenyl)pyrene (TFPPy) + carbohydrazide (CHYD)
TFPT–COF	1,3,5-tris-(4-formyl-phenyl)triazine(TFPT)+ 2,5-diethoxy-terephthalohydrazide
TGA	Thermogravimetric analysis
Tp	2,4,6-triformylphloroglucinol
TPA	terephthalaldehyde
TPB	1,3,5-tri-(4-aminophenyl)benzene
TpBD	1,3,5-triformylphloroglucinol and benzidine
TPB-DMTP-COF-SH	triazole and thiol groups-functionalized COF (2,5-dimethoxyterephtaldehyde (DMTA) + 2,5-bis(prop-2-in-1-yloxy)terephtaldehyde (BPTA) + 1,3,5-Tris-(4-aminophenyl)benzene (TAPB))
TPhP	Triphenyl phosphate
TpND	a COF synthesized with Tp and ND
TpODH	Oxalyldihydrazide (ODH) + 1,3,5-triformylphloroglucinol (Tp)
TpPa-NH2@EDTA	EDTA-functionalized COF (triformylphloroglucinol (Tp) + 2-nitrobenzene-1,4-diamine (Pa-NO2) + ethylenediaminetetraacetic dianhydride (EDTA dianhydride))
TPT-CHO	2,4,6-tris(p-formylphenoxy)-1,3,5-triazine
TS-COF-1	Triazine-polyimide-COF
TS-COF-2	Task-specific Triazine-Schiff base-COF
TTB-COF	Thioether-functionalized COF (2,5-bis(2-(ethylthio)ethoxy) terephthalohydrazide (BETH) + 1,3,5-triformylbenzene (TFB))
Tz	1,3,5-tris(4-formyl-phenyl) triazine
TzDBd	1,3,5-tris(4-formyl-phenyl) triazine + 4,4'-diamino-[1,1'-biphenyl]-2,2'-dicarboxylic acid
U.S. EPA	The United States Environmental Protection Agency
VSM	vibrating sample magnetometer
WHO	World Health Organization
XAFS	X-ray absorption fine structure
XANES	X-ray absorption near-edge structure spectroscopy

XPS	X-ray photoelectron spectroscopy
λex	Wave length of external UV

Reference

[1] Wang, H., Wang, H., Wang, Z.W., Tang, L., Zeng, G.M., Xu, P., Chen, M., Xiong, T., Zhou, C.Y., Li, X.Y., et al. (2020). Covalent organic framework photocatalysts: structures and applications. Chem. Soc. Rev. 49, 4135-4165.

[2] Huo, J., Luo, B., and Chen, Y. (2019). Crystalline covalent organic frameworks from triazine nodes as porous adsorbents for dye pollutants. ACS Omega. 4, 22504-22513.

[3] Lu, X.F., Ji, W.H., Yuan, L., Yu, S., and Guo, D.S. (2019). Preparation of carboxy-functionalized covalent organic framework for efficient removal of Hg^{2+} and Pb^{2+} from water. Ind. Eng. Chem. Res. 58, 17660-17667.

[4] Firoozi, M., Rafiee, Z., and Dashtian, K. (2020). New MOF/COF hybrid as a robust adsorbent for simultaneous removal of Auramine O and Rhodamine B dyes. ACS Omega. 5, 9420-9428.

[5] Dinari, M., and Hatami, M. (2019). Novel N-riched crystalline covalent organic framework as a highly porous adsorbent for effective cadmium removal. J. Environ. Chem. Eng. 7, 102907.

[6] Zhuang, S.T., Chen, R., Liu, Y., and Wang, J.L. (2020). Magnetic COFs for the adsorptive removal of diclofenac and sulfamethazine from aqueous solution: Adsorption kinetics, isotherms study and DFT calculation. J. Hazard. Mater. 385, 121596.

[7] Li, Y., Yang, C.X., Qian, H.L., Zhao, X., and Yan, X.P. (2019). Carboxyl-functionalized covalent organic frameworks for the adsorption and aemoval of triphenylmethane dyes. ACS Appl Nano Mater. 2, 7290-7298.